11-1-2018

Interior Damage of Residential Building Due to Wind-Driven Rain Intrusion

Farzaneh Raji
Florida International University, fraji001@fiu.edu

FLORIDA INTERNATIONAL UNIVERSITY

Miami, Florida

INTERIOR DAMAGE OF RESIDENTIAL BUILDING DUE TO WIND-DRIVEN RAIN INTRUSION

A dissertation submitted in partial fulfillment of

the requirements for the degree of

DOCTOR OF PHILOSOPHY

in

CIVIL ENGINEERING

by

Farzaneh Raji

2018

To: Dean John L. Volakis
College of Engineering and Computing

This dissertation, written by Farzaneh Raji, and entitled Interior Damage of Residential Building Due to Wind-Driven Rain Intrusion, having been approved in respect to style and intellectual content, is referred to you for judgment.

We have read this dissertation and recommend that it be approved.

_____
Lu Zhang

_____
Peter Irwin

_____
Arindam Gan Chowdhury

_____
David Garber

_____
Ioannis Zisis, Major Professor

Date of Defense: November 01, 2018

The dissertation of Farzaneh Raji is approved.

_____
Dean John L. Volakis
College of Engineering and Computing

_____
Andrés G. Gil
Vice President for Research and Economic Development
and Dean of the University Graduate School

Florida International University, 2018

DEDICATION

I would like to dedicate this dissertation to my beloved husband, parents, and brother, for their wholehearted support and encouragement.

ACKNOWLEDGMENTS

The author is very thankful to her major advisor, Dr. Ioannis Zisis, for his support and guidance throughout the research. This research was possible, first, because of his thoughtful management and insightful comments. During these years, he was a great source of encouragement and inspiration.

My sincere appreciation goes to Dr. Chowdhury and Dr. Pinelli. Their knowledge and contributions were essential to this research. A special thanks goes to the members of my doctoral committee, Dr. Irwin, Dr. Zhang and Dr. Garber, for their valuable participation and accessibility.

Thanks are due to the Wall of Wind staff, Raphael Greenbaum, Walter Conklin, and Roy Liu Marques, for their help during the experimental tests. I would like to offer my sincere thanks to my friends and colleagues, Dr. Mohammadtaghi Moravej, Manuel Matus and Dr. Thomas Baheru, for their help and support.

The funding from the International Hurricane Research Center (IHRC) at FIU, Florida Division of Emergency Management, and the Federal Alliance for Safe Homes is greatly acknowledged. I offer special thanks to Florida International University for funding the writing phase by the Dissertation Year Fellowship (DYF).

ABSTRACT OF THE DISSERTATION

INTERIOR DAMAGE OF RESIDENTIAL BUILDING DUE TO WIND-DRIVEN RAIN INTRUSION

by

Farzaneh Raji

Florida International University, 2018

Miami, Florida

Professor Ioannis Zisis, Major Professor

This research aims to experimentally investigate the interior damage in residential buildings caused by rainwater intrusion during hurricane events. The first step, to experimentally evaluate the wind-driven rain effects on the building's interior, is to accurately simulate the rain field associated with the hurricane. The wind-driven rain simulation was performed at the 12-fan Wall of Wind Experimental Facility at Florida International University. The characteristic of the simulated rain field was compared to a target characteristic obtained from the recorded data from past hurricanes to validate the simulation.

In the next step, the large-scale models were subjected to the simulated rain field to observe the water propagation inside the models. The gable and hip roof models were prepared with three different exterior damage conditions, including the light damage state, minor damage state, and moderate damage state, to investigate the effect of

envelope openings on the water propagation path. Each model was tested at three wind angles of 0˚, 45˚ and 90˚ to assess the effects of wind direction. The interior of the models was divided into 6 different room compartments separated by partition walls, as well as 6 different attic compartments divided by short divider pieces. Finally, the results were used to evaluate the share of each interior component from the total amount of water that intrudes into the building.

The last phase of the research concentrated on the experimental evaluation of the sustained damage by partition walls subjected to water intrusion. The full-scale model was subjected to the simulated rain field at the Wall of Wind Experimental Facility test section. The interior of the model was built to simulate the actual interior of a residential building. The experimental results were used to evaluate the sustained damage by the partition.

This research made a great step forward in clarifying the mechanism of interior damage sustained in residential buildings due to rain intrusion during hurricanes. Most important, the results can be used in Hurricane Loss Models to predict the sustained damage on residential buildings at different hurricane hazard levels.

TABLE OF CONTENTS

CHAPTER PAGE

LIST OF TABLES

TABLE PAGE

LIST OF FIGURES

FIGURE PAGE

CHAPTER 1

INTRODUCTION AND LITERATURE REVIEW

CHAPTER 1. INTRODUCTION AND LITERATURE REVIEW

1.1. Problem Statement

While past experiences have proven the vulnerability of low-rise buildings to hurricane events, the number of economic losses caused by hurricanes has increased dramatically in the past few decades. According to the National Science Board, 2007, the average annual hurricane-induced economic losses in constant 2006 dollars were $1.3 billion in 1949-1989, $10.1 billion in 1990-1995, and exceeded $35 billion in the first decade of this century. This vulnerability to hurricane impact becomes more detrimental in states like Florida, with a high concentration of population along the coast.

To ensure the economic sustainability of Florida and other coastal states, and to improve the safety of their citizens, it is required to develop sustainable coastal communities and hazard-resilient coasts. This requires the accurate projection of risks and subsequent development of risk mitigation strategies to allow sustainable coastal living.

Although probabilistic simulating models (HAZUS, 2009 and FPHLM, 2015) are already in use for estimating hurricane risk, these models are imperfect due to high levels of simplifications. One of the major deficiencies of these models is related to estimating hurricane losses occurring at interior components of buildings. Despite the fact that interior damage could make up 50% to 100 % of the total damage costs, most of the past studies focused only on exterior damages. As a result, the analytical tools of loss estimation models are designed based on empirical and judgmental relations that calculate the amount of interior loss as a function of exterior damage.

Considering the importance of the accurate evaluation of interior damages on the one hand, and the inadequacy of existing methods on the other hand, this project aims to propose an improved method for the evaluation of interior damages that occur in residential buildings due to Wind-Driven Rain (WDR) during hurricane events. This improved method can later be applied in loss estimation models, and enhances their risk prediction accuracy.

Interior damage, which includes damage to the ceilings, drywall partitions, carpeting, cabinets, and utilities, is mainly due to rainwater ingress through defects or breaches of the building envelope. This has also been confirmed by many post-disaster surveys (Mileti, 1999, Van de Lindt et al., 2007, FEMA, 2005, FEMA P-942, 2013, FEMA 488, 2005 and Bhinderwala, 1995).

While experimental studies are required for assessing the performance of building interiors at water intrusion caused by wind-driven rain, there is no standard methodology for performing these tests. Therefore, there is a need to establish a framework for large-scale testing with respect to designing interior components, setting the envelope conditions, simulating the environmental conditions and determining monitoring protocols. One of the main objectives of this project is to develop such a framework for the large-scale testing of a low-rise building under WDR. For this purpose, experimental tests were performed at the Wall of Wind (WOW) Experimental Facility (EF) at Florida International University (FIU).

Understanding the WDR effects on a building requires a broad knowledge over several scientific fields, such as meteorological characteristics of the environmental

conditions (rain, wind, solar radiation, humidity, etc.), the physical mechanism of rain deposition on the building façade, and the hydrothermal behavior of building components. Considering the broad extent of science related to this subject, three main fields of concentration can be defined from previous studies that investigated WDR:

1. Understanding characteristics of the free-field WDR and its relation to the horizontal rainfall and wind speed. This includes the meteorological investigation of horizontal rainfall, the size distribution of raindrops and the raindrop's velocity. Some of the well-known studies on this subject are Best, 1950, Waldvogel, 1974, Mualem & Assouline, 1986 Dingle & Lee, 1972 and Lacy, 1977. These studies resulted in the experimental relations for the estimation of the rain size distribution. The rain size distribution is a parameter that determines the characteristics of a wind-driven rain field. Realistic simulation of the wind-driven rain requires accurate estimation of the rain size distribution.
2. Quantifying the amount of impinging water into the building envelope, which can be performed either by experimental testing or CFD modeling (Choi, 1999 and Blocken & Carmeliet, 2002). The results of this type of studies can lead to semi-empirical relations, which determine the amount of water deposition into a building envelope using the Rain Admittance Factor (Straube & Burnett, 2000) or the Wall Factor (ISO, 2009). These studies resulted in experimental relations to determine the amount of water that reaches the building exterior subjected to wind-driven rain. Since the amount of water intrusion into the building interior depends on the amount of water deposition on the building exterior, accurate

estimation of the water exposure at the building exterior can significantly affect the prediction of water intrusion into the building interior.

3. Predicting the amount of water intrusion through pre-existing defects and envelope breaches, and evaluating the performance of the building under WDR water infiltration (the effect on the building envelope). This area of study includes two main phases. The first phase is to evaluate how much of the deposited water on a building envelope would penetrate the building due to envelope breaches (ASTM E331, 2009 and ASTM E547, 2009b). The basis of all these methods is to measure the amount of intruded water when the building envelope is exposed to water spray with a predefined rain rate and the pressure difference between the interior and exterior. These methods are limited by two main weak points. First, they do not model the Rain Size Distribution (RSD), which represents actual rain characteristics. Second, they apply pressure differences in order to capture the effects of wind velocity, so they do not accurately simulate the droplet velocity. The second phase is to evaluate the effects of the intruded water on the hygrothermal behavior of the building envelope, which is usually performed by investigating the Heat, Air and Moisture (HAM) transfer characteristics. There are three main methods to perform HAM studies, including numerical modeling (Mendes & Philippi, 2005), field measurements (Desta, Langmans, & Roels, 2011) and laboratory testing. For laboratory tests, the water spray method, direct insertion method (Korsgaard & Rode, 1992), or both (Tsongas, Govan, & McGillis, 1998 and Hens & Fatin, 1995), can be implemented to simulate the intruded wind-driven rainwater.

While these three areas are like the links of a chain that should be consequentially followed for the accurate investigation of the WDR effects on the building envelope, most of the previous studies have mainly concentrated on one area and considered it separate from the whole system. While these simplified approaches to the problem can be justified by its complexity and a huge amount of effort required to consider all the related tasks, they can be problematic and lead to erroneous results. For example, many of the studies performed on the amount and effect of rain ingress into the building envelope (step 3) have skipped the preceding investigation of the amount of impinging rain on the building façade (step 2) by simply relying on the existing data in the literature. In this case, the erroneous estimation of the amount and intensity of water deposition can lead to an inaccurate prediction of the amount and intensity of water ingress and, as a result, the erroneous evaluation of hygrothermal performance. One of the novel aspects of this project is that it incorporates all the steps required for investigating the WDR effects, starting from actual WDR simulation to rain deposition on the building envelope, and rain infiltration through envelope defects and breaches in an integral approach.

Another unique aspect of this study is that it investigates the effect of water intrusion at envelope breaches caused during severe wind events. Although the most significant interior damage is caused by water intrusion at large envelope beaches, none of the previous studies have investigated the building performance for these extreme situations.

Almost all the previous studies have neglected the hurricane-induced damages, and only assessed the water intrusion at pre-existing defects caused by improper design,

defective workmanship, and inappropriate maintenance. In this study, the water intrusion through the hurricane-induced envelope breaches is investigated, as well as the water ingress through the pre-existing defects.

1.2. Research Objectives and Methodology

The primary objectives of the research project can be summarized as:

- Develop a methodology for investigating the WDR effects on a building's interior.
- Propose quantitative measures for describing the extent of damages at interior components of a building (increase in moisture content of interior components).
- Generate test-based data on interior damages due to WDR using large-scale models.
- Obtain a relation between the intruded water and expected interior damage.

1.3. Methodology

To accomplish these goals, the following tasks were performed:

1. First, the wind-driven rain needed to be simulated at the test section of the WOW EF. The generated rain field simulated the rain characteristics during a hurricane event. The rain size distribution was selected as a criterion that presents the characteristics of the rain field in a hurricane event. To accurately simulate the rain field, the rain size distribution of the generated rain was matched to the target rain size distribution associated with hurricanes. To do so, preliminary tests were performed to investigate the effect of nozzle type and water pressure on the

generated rain size distribution. Based on the obtained information, the proper nozzle type was selected and installed in front of the fan to simulate the rain field.

2. Then, the large-scale models were constructed to simulate generic low-rise residential buildings. These models were tested at the simulated rain field to investigate the water propagation path on the building interior during a hurricane event. The large-scale models were designed to allow water intrusion through envelope breaches and defects. The envelope breaches were mainly exterior damages caused by hurricanes, so they were depended on hurricane severity and, as a result, maximum gust speed. Since the envelope breaches presented the condition of building subjected to different wind speeds, the extent of envelope breaches for each level of wind intensity was estimated. The estimation was performed using the available data from hurricane loss modeling (Cope, 2004). The level of exterior damages was determined for each wind intensity, then envelope breaches were generated in the model by sequentially and partially removing panels representing the roof and windows.
3. Next, the results of the large-scale tests were modified to be implemented into the Florida Public Hurricane Loss Model (FPHLM). Additionally, some minor adjustments were applied to FPHLM to adopt the new interior loss evaluation module. Therefore, the FPHLM relations were derived to capture the water propagation matrices developed based on the large-scale experimental test results.
4. Based on the information obtained from step 3, the most critical cases were selected for further investigation during the full-scale experiments. Since performing the WDR test for full-scale models was a costly and time-consuming

task, the tests were performed only for the most critical model configurations and wind angles. The results of these full-scale tests were presented as graphs showing the amount of increase in the moisture content of different interior components as a function of the volume of water that reaches each interior wall surface. This increase in moisture content was used to determine the damage extent of interior components using qualitative measures.

1.4. Organization of Dissertation

This dissertation is organized into five chapters. The first chapter provides an introduction to the research and explains the goal and objective of the study. The literature review of the dissertation topic is included in the first chapter. It also provides a brief description of the applied methodology and tasks performed at different phases of the research.

The second chapter is dedicated to the simulation of a rain field at WOW EF test section. In this chapter, the rain size distributions generated by different nozzle types at different water pressures are experimentally investigated. Based on these experiments, the appropriate nozzle type is selected to simulate the rain field at the test section. Two droplet measurement devises are used to measure the rain size distribution of the simulated rain field. Calibration of the rain field is achieved based on the close match of the rain size distributing at the test section to the target rain size distribution.

The experimental water propagation study is presented in the third chapter. This chapter describes the preparation of the large-scale model to simulate the water propagation inside the building once the water intrudes through the envelope breaches

and defects. A discussion on how the decision is made for the location and the area of the envelope breaches and defects at different exterior damage states is also provided. The results of the water propagation tests are presented and discussed. Finally, how to implement these results into the FPHLM model is explained.

The fourth chapter presents the full-scale experimental evaluation of the moisture-induced damages of the building interior. The model preparation and moisture measurements are explained in this chapter. Discussion on how the test results are used to develop water volume-damage relationships, and how these relationships can be used for the prediction of moisture-induced damages, is also provided.

Chapter five is the last chapter and includes the summary and conclusion of the dissertation.

CHAPTER 2

RAIN FIELD SIMULATION

CHAPTER 2. RAIN FIELD SIMULATION

2.1. Introduction

This section is dedicated to the explanation of the experimental tests performed to calibrate the simulated rain field at the WOW EF facility. To simulate the actual rain characteristics during a hurricane event, it was tried to model the rain field with matching rain size distribution to a target rains size distribution obtained by Baheru, 2014 (Figure 1). The target rain size distribution was achieved by fitting a Gamma distribution to the normalized rain size distribution observed during three past hurricanes, including Hurricane Alex (2004), Hurricane Charley (2004) and Hurricane Gaston (2004), presented in the study by A. Tokay, Bashor, Habib, & Kasparis, 2008. The data collocation during these hurricanes was performed using the Joss-Waldvogel disdrometer (JWD). This disdrometer was commercialized in 1967, and has been used in many previous field measurements.

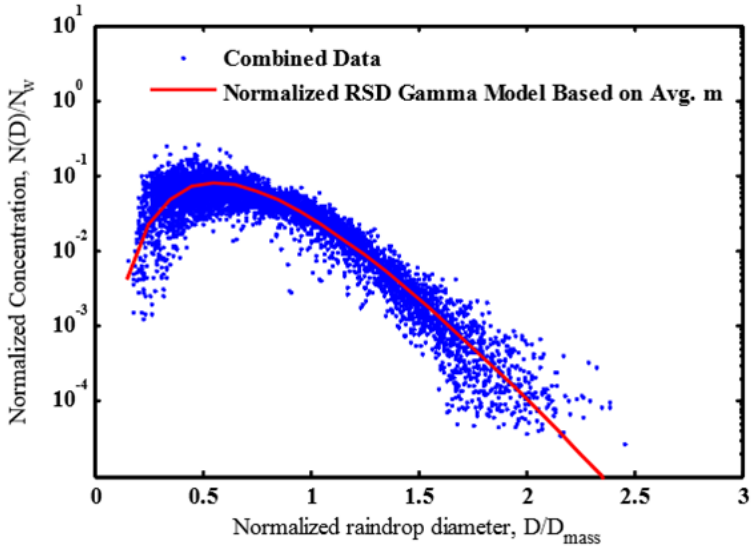

Figure 1. Normalized target Rain size distribution, Baheru 2014

To convert this normalized rain size distribution to the dimensional rain size distribution, which can be simulated at the laboratory, the rain parameters should have been selected, including liquid water content (W in g/m^3) and mass-weighted mean diameter (D_{mass}, in mm). These two parameters were selected based on the horizontal target Rain Rate (RR) of 25.4 mm/hr. and the RR - W and RR - D_{mass} relations presented in Baheru, 2014. Using those relations, W and D_{mass} were selected as 1.21 g/m^3 and 1.77 mm. Given the W and D_{mass}, the normalizing number concentration parameter N_w, was calculated as 10.05×10^3 ($1/m^3$ mm) by using EQ. 1 as follows:

$$N_w = \frac{4^4}{\pi \rho_w} \left(\frac{D}{D_{mass}^4} \right) \qquad \text{EQ. 1}$$

The full-scale target rain size distribution was calculated from the normalized rain size distribution, as shown in Figure 2.

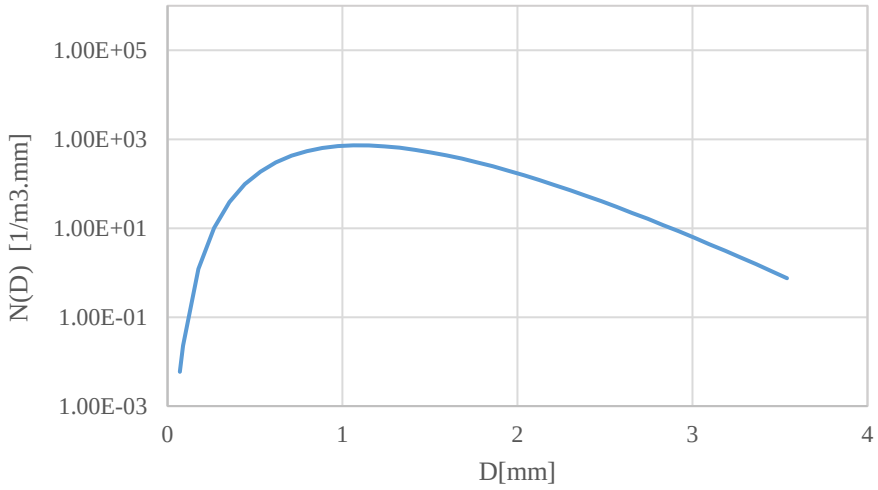

Figure 2. Full-scale target rain size distribution

Because damage estimation experiments were designed for a 1:4 scaled residential building model, the rain field was calibrated with the 1:4 scale, and the target rain size distribution was also transferred to the scale of 1:4 (Figure 3).

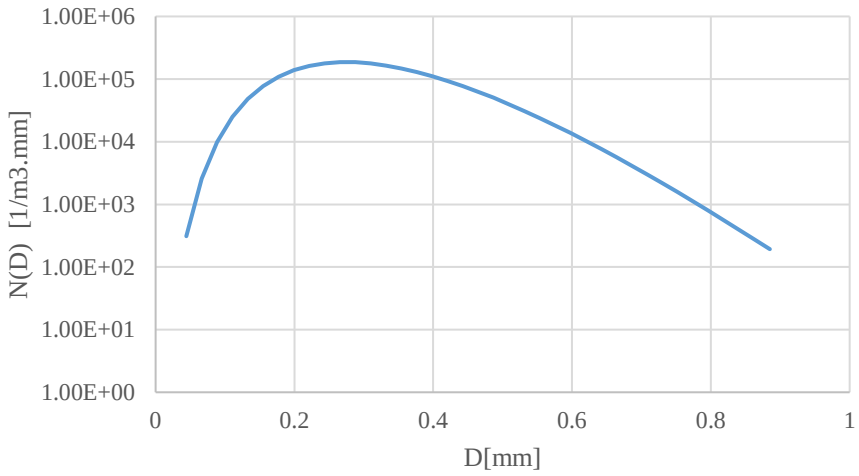

Figure 3. 1:4 scaled rain size distribution

Complete similarity between the full-scale and scaled-down model requires an identical air density ratio, Reynolds number (Re), and Froude number (Fr) between the model and prototype. The similarity of water-to-air density ratio is held by default. However, it is impractical to maintain the similarity of Reynolds and Froude numbers, simultaneously. Therefore, based on the possible effects on the test results, the similarity of the Froude number was preferred over the Reynolds number. Based on the Froude number's similarity, the following equation was used to relate the drop diameter (*D*) and raindrop size distribution, (*N*), between the model scale (*ms*) and full-scale (*fs*) model:

$$D_{ms} = \lambda_L \cdot D_{fs}\ ; \qquad N_{ms=} N_{fs}/\lambda_L^4 \qquad \text{EQ. 2}$$

In this equation, λ_L, is the length scale. Based on this equation, the 1:4 scaled target rain size distribution was obtained from the full-scale target rain size distribution by dividing

the vertical axis (raindrop size distribution N(D)) to $\lambda_L{}^4$ and multiplying the horizontal axis (drop diameter, D), to λ_L.

2.2. Droplet Measurement Devices

Parsivel^2 from OTT Hydromet and the precipitation imaging probe (PIP) were the two-droplet measurement devices used in this study. While the PIP is famous for its high precision for measuring the wind-driven rain, there are several studies confirming the inadequacy of Parsivel performance, especially when the wind is introduced into the measurements (A. Tokay, Petersen, W. A., Gatlin, P., & Wingo, M., 2013, Lopez, 2011 and Friedrich, 2013).

Lopez, 2011, showed that the inaccuracy of Parsivel for wind-driven rain measurement is mainly associated with the oblique trajectory angle of the raindrops caused by the wind. He concluded that when the wind angle is perpendicular to the laser plane of Parsivel, the droplet measurements are in good agreement with the results of the PIP. However, the results showed that Parsivel underestimates the number of small drop sizes (less than 0.68 mm), even when the wind angle is perpendicular to the laser field.

Tokay et al. compared the droplet measurement accuracy of Parsivel^2, Parsivel, and the Joss–Waldvogel (JW) disdrometer (A. Tokay, Wolff, & Petersen, 2014). It was shown that the accuracy of the Parsivel^2 is increased for small drop sizes in the range of 0.34–0.58mm, and it was concluded that Parsivel^2 is certainly an improved version of Parsivel for the raindrop size and rainfall measurements.

In this study, the droplet measurement is performed for wind-driven rain with the wind angle perpendicular to the laser field of the sensors. According to Lopez, 2011, the accuracy of Parsivel in this situation is intact for larger sizes (larger than 0.68mm). On the other hand, a higher accuracy is expected for smaller droplets (smaller than 0.5mm) for the Parsivel^2, therefore it was decided to use both Parsivel^2 and the PIP for the droplet measurements.

2.3. Measurement of Rain Size Distribution at Stagnant Air

In order to decide on the type and number of nozzles, several preliminary tests were performed on stagnant air. The main advantage of these tests was that they did not require turning on the WOW EF fans, which would have increased the experimental cost. These experiments allowed for testing different nozzle types and different water pressures. To perform these tests, a single nozzle was mounted above the sensors, and the sprayed droplets moved in the vertical direction through the stagnant air (see Figure 4). The rain size measurement was performed using both Parsivel^2 and PIP, and the resulting RSDs were compared to investigate the accuracy of Parsivel^2. Based on the measured RSDs, the most proper nozzle type was selected. The effect of water pressure on the RSD of the selected nozzle is investigated in the next step.

Figure 4. Droplet measurement using Parsivel and PIP for single-nozzle spray in the stagnant air

2.3.1. Nozzle types

Six different nozzle types were selected for the preliminary testing. The selection of these nozzles was based on the previous experiment performed by Baheru, 2014. In that study, Teejet extended range flat 8008-E was selected for the rain simulation. A water pressure of 52 psi was reported at the nozzle's tip during the experiment. According to the nozzle manual (TeeJet Technologies, 2015), the TEEJET 8008 – E nozzle generates medium-size droplets (See Table 1 for details on drop sizes) at 40-60 psi pressures. Since the resulting RSD using the TEEJET 8008 – E showed a higher number concentration than the target RSD for drop sizes larger than 0.6 mm, this study attempted to test the nozzles that generated finer droplets.

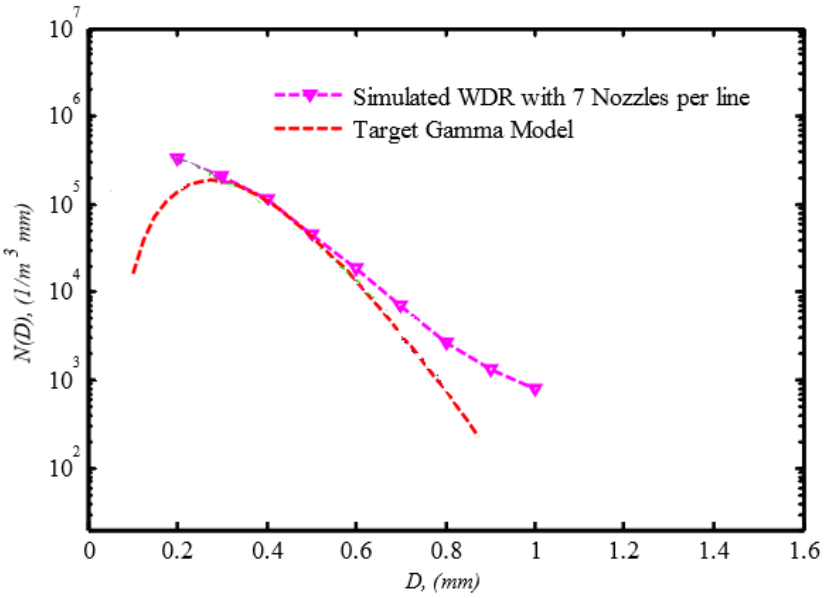

Figure 5. Target and achieved RSD, Baheru, 2014

Table 2 displays the tested nozzles, along with their nozzle sizes, at different water pressures. The water pressure for a single nozzle test was expected to vary between 40 to 50 psi. The same water pressure range was observed during the experiments.

Table 1. Droplet Size Classification based on ASABE S572.1

Size Classification	**VMD* Range (Microns)**
Extremely Fine	<60
Very Fine	61-105
Fine	106-235
Medium	236-340
Coarse	341-403
Very Coarse	404-502
Extremely Coarse	503-665
Ultra-Coarse	>665

* Volume Median Diameter

Table 2. Tested nozzles

	Water Pressure PSI						
type	15	20	25	30	40	50	60
XR8008	VC	VC	C	C	M	M	M
XR11001	F	F	F	F	F	F	VF
XR110015	F	F	F	F	F	F	F
XRC11002	M	F	F	F	F	F	F
XRC11004	M	F	F	F	F	F	F
XRC80015	M	M	M	M	M	F	F

*VC: Very Coarse, C: Coarse, M: Medium, F: fine, VF: Very fine

Figure 6 compares the droplet size distribution for different nozzles, measured using Parsivel (Figure 6a) and PIP (Figure 6b). As can be observed from Figure 6a, the Parsivel measurement showed that all the tested nozzles except for XR110015 lead to a higher number concentration than the XR8008E nozzle for drop sizes larger than 0.73 mm. PIP data resulted in an almost similar trend, except that 0.33 mm was the limit

where the number concentration of nozzles (except for the XR110015 nozzle) exceeded the number concentration of the XR8008E nozzle. While the similar trend confirms the fact that XR110015 can be a potential substitute for the XR8008E nozzle to modify the rain size distribution (decrease the number concentration for drop sizes larger than 0.6 mm to obtain a better match with target RSD), the difference between the results of Parsivel and the PIP needs to be further investigated.

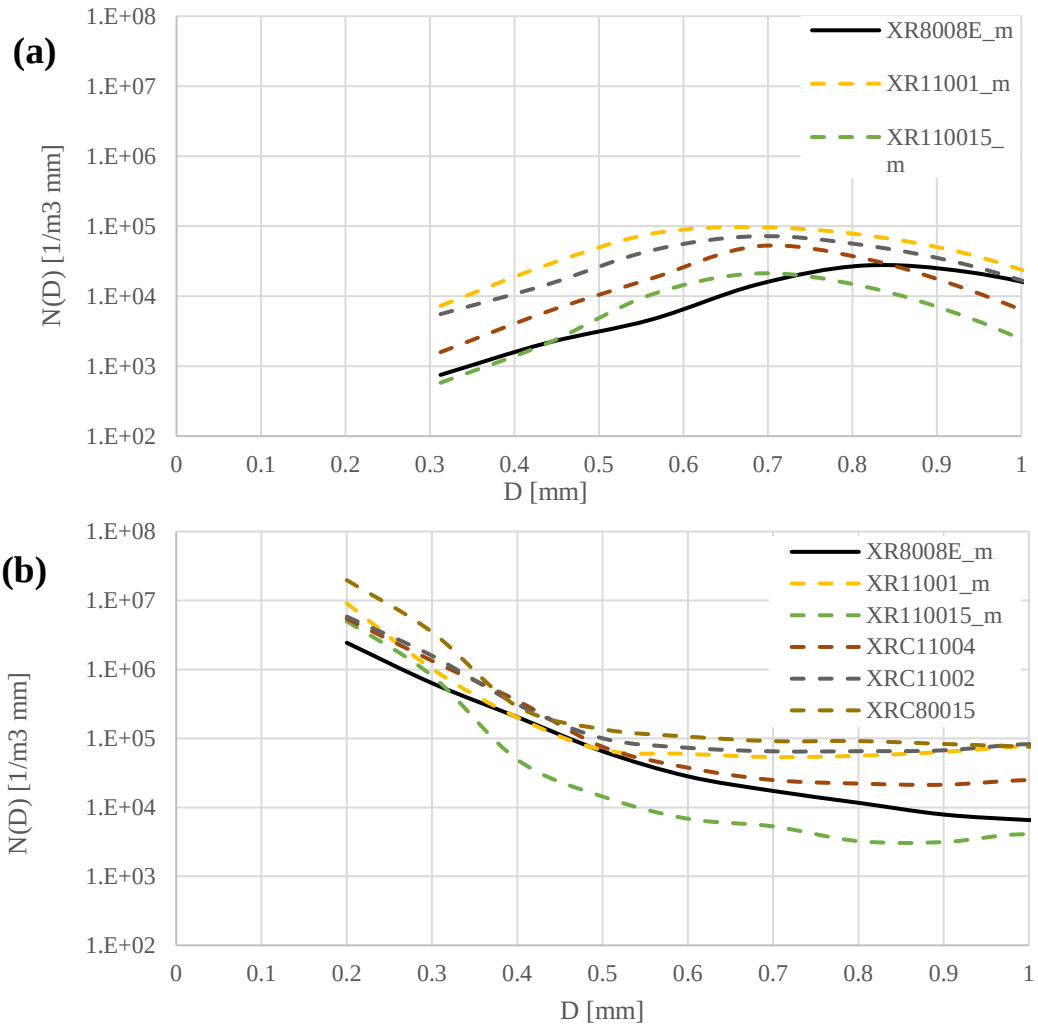

Figure 6. Droplet size distribution for different nozzles measured by (a) Parsivel and (b) PIP

Figure 7 compares the results of Parsivel and PIP for the XR8008E nozzle. As can be observed from this figure, Parsivel data lay below the PIP curve for drop sizes less than 0.7 mm. This observation can be attributed to the underestimation of the number concentration for fine droplets by Parsivel. The same observation can be made when comparing the RSD of other nozzle types using Parsivel and PIP. Therefore, it can be concluded that even in the stagnant air situation, where there is no obliqueness in the trajectory angle of the droplets, the measurement of Parsivel is not accurate enough for drop sizes less than 0.6 mm. Although this level of inaccuracy can be important for this study where the droplets are simulated with the scale of 1:4, in real situations, the performance of Parsivel can be accurate enough since the concentration of the raindrops lies between 1 to 3 mm.

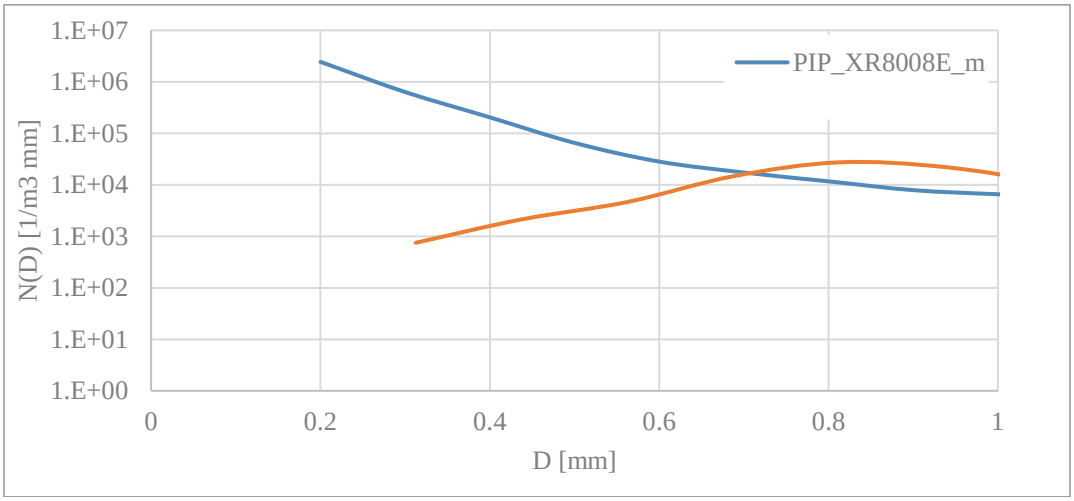

Figure 7. Comparing the RSD obtained from Parsivel and the PIP, for the XR8008E nozzle

2.3.2. Water pressure

The water pressure is a parameter that affects the generated size distribution of the nozzle, as well as its flow rate. Since the pressure head of the supplying pipeline is

constant, increasing the number of nozzles that fed on the pipeline can lead to a decrease in water pressure at the tips of the nozzles. In this section, the RSD generated by the XR8008E nozzle at different water pressures was investigated to assess the effect of water pressure on the generated drop sizes. The XR8008E nozzle was selected, as according to the manual the size range of this nozzle was highly dependent on water pressure. To alter the water pressure at the tips of the nozzle, the tests were performed with different numbers of nozzles installed on the pipeline. For each test, only one of the nozzles sprayed water above the droplet measurement device, while the water from the rest of the nozzles was sprayed out of the measurement field and could not participate in the measured RSD. Table 3 shows the water pressure as a function of the number of installed nozzles.

Table 3. Water pressure at tips of nozzles as a function of the number of nozzles

Number of nozzles	Pressure [psi]
2	42
4	28
6	16

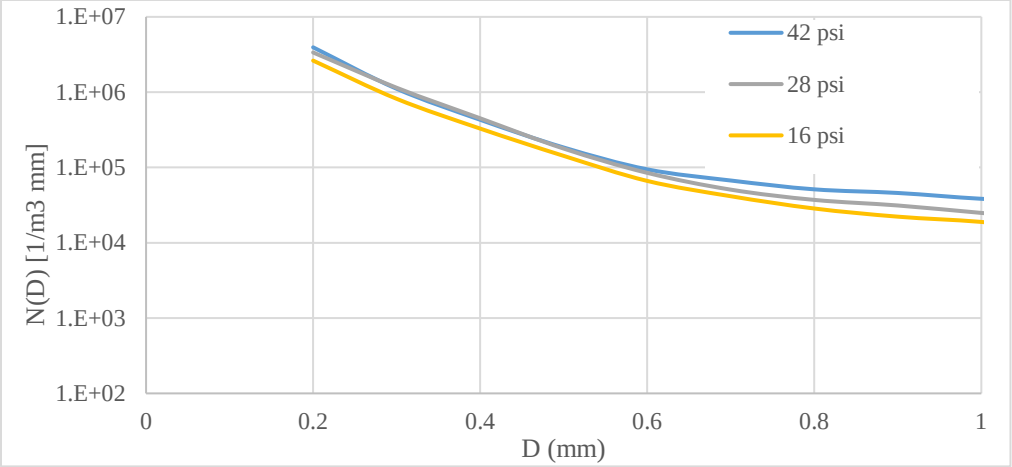

Figure 8. Effect of water pressure on RSD of droplets generated by the XR8008E nozzle

Figure 8 displays the RSD obtained for the RX8008E nozzle at different water pressures by the PIP. As can be observed from this figure, increasing the water pressure from 16 to 42 psi can lead to a slight increase in the concentration of the droplets. This increase becomes even more significant when the droplet size is increased.

2.4. Calibration of the WOW EF Rain Field

The simulation of the Wind-driven Rain (WDR) was performed at the 12-fan WOW EF at FIU. The WOW EF is a state-of-the-art wind engineering research laboratory consisting of a 2X6 array of 700-horsepower fans with a test section 4.3 m high and 6.1 m wide (Chowdhury et al., 2017).

The calibration of the WDR requires the simultaneous simulation of wind and rain. The wind field was calibrated to simulate the atmospheric boundary layer associated with suburban terrain. The mean wind speed profile, along with the turbulence intensity for the generated flow, is presented in Figure 9. These graphs are normalized according to the roof height of the large-scale model (0.76 m).

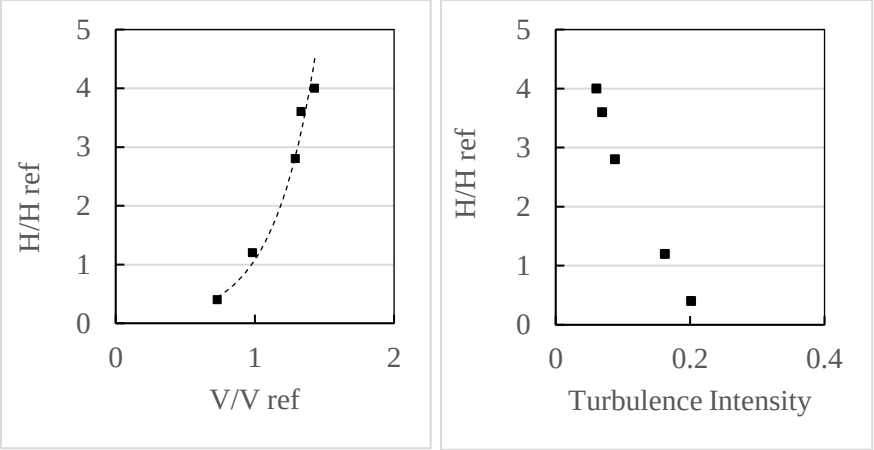

Figure 9. Mean velocity (left) and turbulence intensity profiles (right)

Once the RSDs generated by different nozzle types were compared, the decision was made to use only the XR8008E and XR110015 nozzles for simulation of the rain field at the WOW EF test section. To generate the raindrops, the nozzles were attached to the water hoses mounted on the spires in front of the fans (Figure 10). The sprayed water droplets could then be carried by the wind flow generated by the fans and simulate the WDR field. The calibration was performed based on a trial-and-error procedure. Three different nozzle arrangements were selected to be tested, including:

- Case 1: Nine XR8008E nozzles on each side spire and ten XR8008E nozzles on the center spire.
- Case 2: A combination of five XR8008E in between four XR110015 on each side spire and five XR8008E nozzles in between five XR110015 nozzles on the center spire.
- Case 3: Nine XR110015 nozzles on each side spire and ten XR110015 nozzles on the center spire.

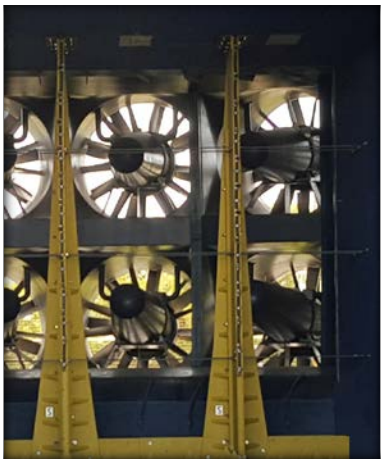

Figure 10. Vertical spires in front of the WOW EF, where the nozzles will be installed on the hoses

Each case was tested for a duration of 5 minutes, and the RSD of the generated rain was measured at the center of the test section using the PIP droplet merriment device. The comparison of the RSD results between case 1 and case 2 is presented in Figure 11. It can be observed that case 1, with only the XR8008E nozzle type, can result in a much better match to the target compared to case 2, where half of the XR8008E nozzles are replaced by XR110015 nozzles. Moreover, it could be predicted that replacing all of the XR8008E nozzles with XR110015 nozzles in case 3 would worsen the agreement to the target RSD. Therefore, it was decided to omit case 3 from the experiment. Considering the good match of the RSD in case 1, it was decided to select the case 1 nozzle arrangement for simulation of the rain field at the WOW EF.

As shown in Figure 11, the PIP measurement results are presented in the range of 0.2 to 1.0 mm. This is the range of reliable measurement for the PIP device based on the calibration performed using the spinning disk calibrator (Baheru, 2014). For drop sizes less than 0.2 mm, the readings were not steady and reliable. On the other hand, it was

improbable to generate droplets larger than 1.0 mm using the TEEJET 8008 – E nozzle with the median-volume diameter of 0.349 – 0.428 mm.

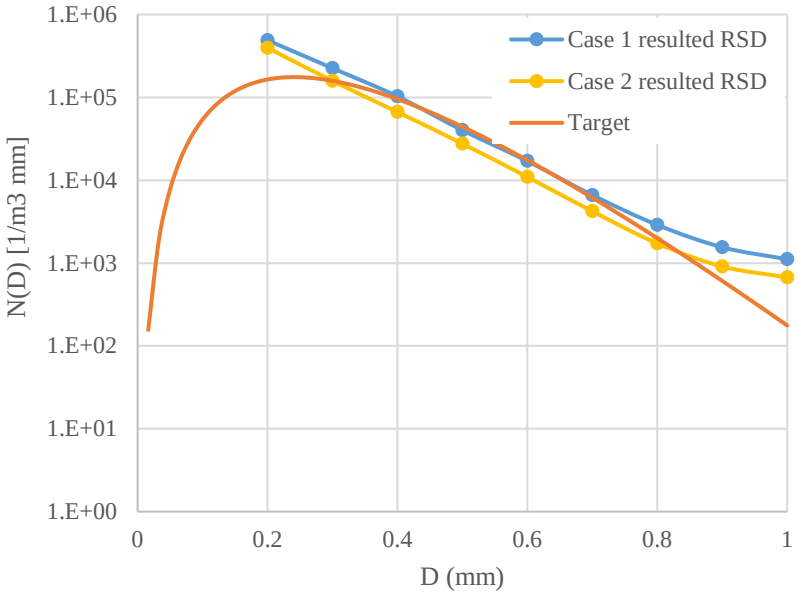

Figure 11. RSD results at the WOW EF test section

To compare the simulation results to the target RSD, Figure 12 shows the normalized simulated RSD, along with the normalized target RSD and the field measurement data.

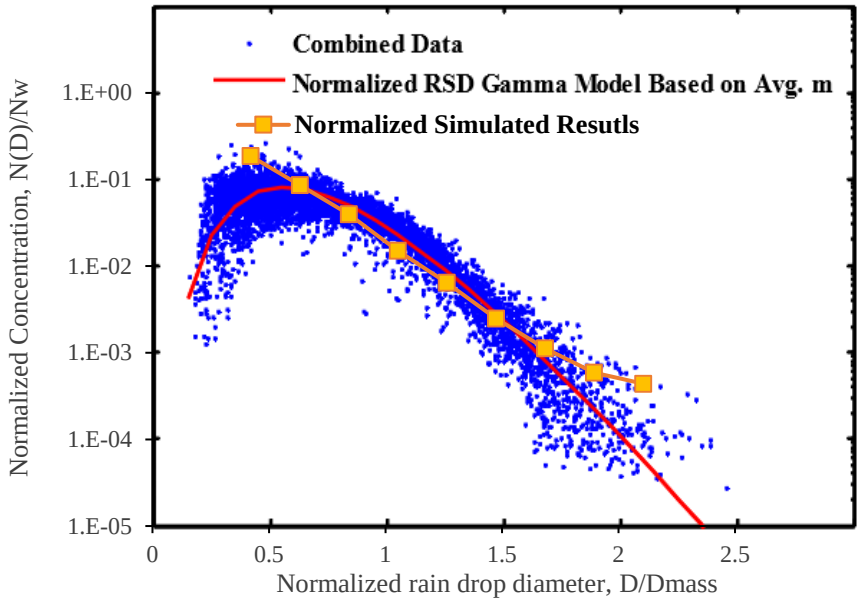

Figure 12. Normalized RSD simulated at WOW EF test section

Once the desired nozzle type and arrangement were selected, the uniformity of the generated rain field was assessed by measuring the RSD at different locations of the test section. In addition to the center of the test section, P1 (6.10, 0, 0.76), the RSD measurement was performed at five more locations, including P2 (6.10, 0.81, 0.76), P3 (6.10, -0.81, 0.76), P4 (6.10, 1.62, 0.76), P5 (6.10, -1.62, 0.76) and P6 (6.10, 0, 1.52). The coordinate axes for locating the measurement points and the turntable are shown in Figure 13.

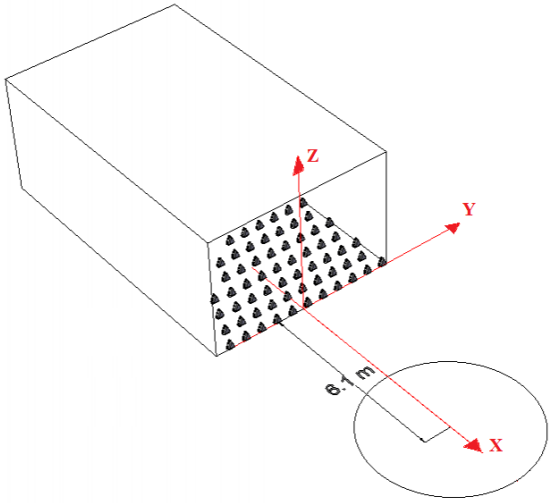

Figure 13. Coordinate axis and turntable

The RSDs at different locations are presented in Figure 14, along with the target RSD. It can be observed that all RSD graphs lie in an acceptable margin from the target RSD, and it can be concluded that the generated rain field can adequately simulate the rain characteristics associated with hurricane events.

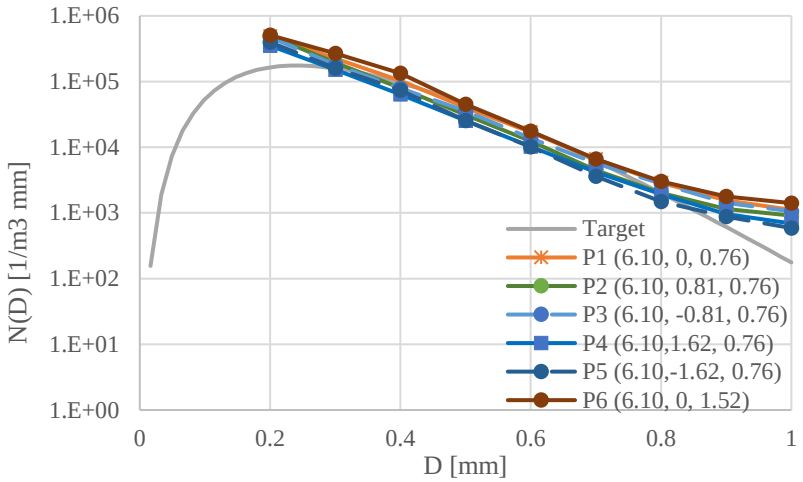

Figure 14. Comparison of RSD at the different location across the test section

In addition to RSD, the WDR rate measurement was also performed at locations P1 to P5. To measure the vertical rain rate, TB3 rain gauge devices were connected to rain-collecting buckets by plastic tubes, as shown in Figure 15. The collecting buckets

were 21.5 cm wide, 26 cm long and 12 cm deep. The water could get into these buckets through the vertical opening on the front face with the area of 217.5 cm^2. The TB3 rain gauge is instrumented with an internal bucket with the capacity of 0.254 mm. Every time the bucket reaches its capacity, it tilts and registers an electric pulse. The history of these pulses is recorded by an ML1-FL data logger and is used in the calculation of the rain rate.

Figure 15. TB3 rain gauge connected to vertical rain-collecting bucket

Figure 16 shows the recorded rain rate at measurement locations of 0.76 m height (P1 through P5). As was expected from the uniformity of RSD, the rain rate is also uniform across the test section. Finally, the mean vertical rain rate of 180 mm/hr is reported at the height of 0.76 m. As will be explained in the next chapter, this is the height of the building models used for the large-scale water propagation tests.

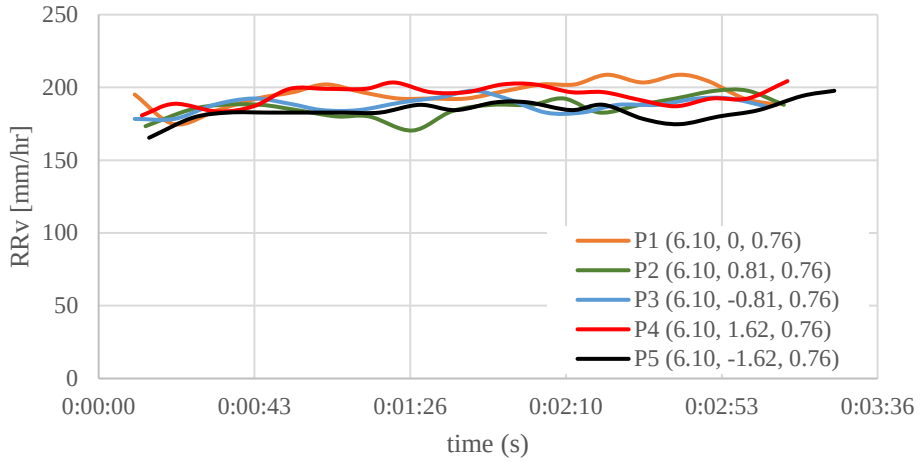

Figure 16. Vertical Rain Rate (RRv) at different locations across the test section

Once the RSD and rain rate were compared at different locations of the WOW EF facility test section, and the uniformity of the simulated rain field was validated, we could conclude that the rain filed was adequately simulated. In the next phase of the study, large-scale building models were subjected to the simulated WDR field that could represent the characteristics of rain during typical hurricane events.

CHAPTER 3

EXPERIMENTAL WATER PROPAGATION TESTS

CHAPTER 3. EXPERIMENTAL WATER PROPAGATION TESTS

3.1. Introduction

The preparation of the large-scale models and water propagation tests are presented in this section. Once the rain field was calibrated at the WOW EF test section, the next step was to prepare and test the large-scale models to investigate the propagation of the water inside the building. Since the water propagation path is directly affected by the envelope opening where the water intrudes into the building, the decision about the area and location of the envelope breaches had to be made. Using the Florida Public Hurricane Loss Model (FPHLM) as reference, it was decided to test models at three exterior damage conditions, i.e. light, minor and moderate. The roof type can also affect the water flow path, so two roof types—hip and gable—were considered. Also, to capture the effect of wind direction, each model configuration was tested at three wind angles of 0˚, 45˚ and 90˚.

3.2. Model preparation

The experimental tests were performed on 1:4 scaled models. Since the layout of the model should represent a typical low-rise residential building, it was decided to use the same layout as the one used for the Florida Public Hurricane Loss Model (FPHLM, 2015). The consistency of the layout allowed for the future implementation of the results into the loss model.

The building model was built out of wood and had horizontal dimensions of 9.14 by 6.10 m, with a roof edge height of 3.05 m (all dimensions are equivalent full-scale).

The model was tested with two roof types, gable and hip, both having a pitch angle of 5:12 and overhang length of 0.3m. The full-scale dimensions of the tested models are presented in Figure 17.

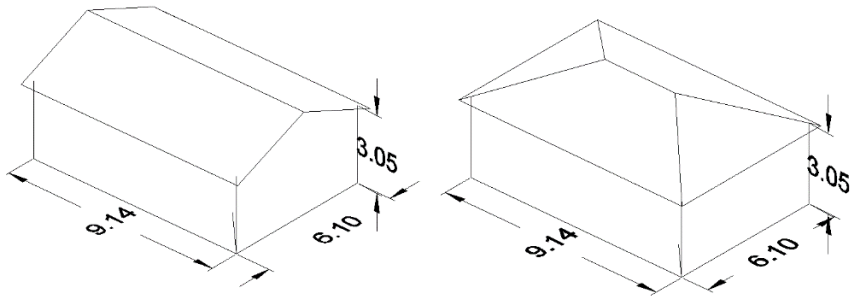

Figure 17. Building models (full-scale dimensions in meter)

The interior of the building was divided into six 3.05 × 3.05 m^2 compartments. Similarly, the attic space was divided into six 3.05 × 3.05 m^2 compartments. The windows are 1.22 m tall and are installed 0.81 m above the floor. Also, there is an opening on each internal partition to simulate the internal wind flow through the interior doors during the tests (Figure 18).

Figure 18. Partition openings

3.3. Exterior Damage State

To capture the effect of envelope openings on the water propagation path inside the building, the models were tested at three different exterior damage states, representing the light, minor and moderate damage of the building envelope. The area and location of the exterior openings associated with each of these damage states were estimated based on the damage matrices developed for the FPHLM model (FPHLM, 2015). The extracted information from the damage matrices is presented in Table 4 and

Table 5 for gable and hip roof models, respectively. The percentage of the total building damage associated with each damage state is presented in the second column. The third and fourth columns show the percentage of the removed roof sheathing and roof cover, respectively. The number of the broken windows is displayed in the fifth column.

Table 4. Damage condition of the gable roof model for each damage state

Damage State	Total building Damage	Removed Roof Sheathing	Removed Roof Cover	Broken Windows
Light (DS0)	up to 6%	0%	5%	0
Minor (DS1)	10%	15%	20%	2
Moderate (DS2)	20%	35%	40%	4

Table 5. Damage condition of hip roof model for each damage state

Damage State	Total building Damage	Removed Roof Sheathing	Removed Roof Cover	Broken Windows
Light	up to 6%	0%	5%	0
Minor	10%	10%	15%	2
Moderate	20%	30%	35%	4

The pre-existing defects of the building envelope can also lead to water intrusion into the building interior during a hurricane event. These defects are usually caused by poor construction or previous minor damages endured from past events. To include the effects of these openings on the water propagation path, two types of envelope defects were included in the models. The seal cracks (500mm x 4mm full-scale) below the windows and the missing sealant of ducts (60mm x 4mm full-scale) located at 1.78 m height above the floor were included. The defect opening type was only considered for the light damage model to represent the exterior state of the building envelope before the occurrence of severing wind-induced damages.

Once the decision was made on the location and area of the defects and breaches, the models were prepared to simulate the water propagation path for each of the desired

exterior damage conditions. The locations and dimensions of the gable and hip roof breaches are displayed in Figure 19. The next section describes how these breaches were made in the wood building model. *Figure 20* shows the layout of the wall defects for DS0, as well as the wall breaches for the DS1 and DS2 model configurations.

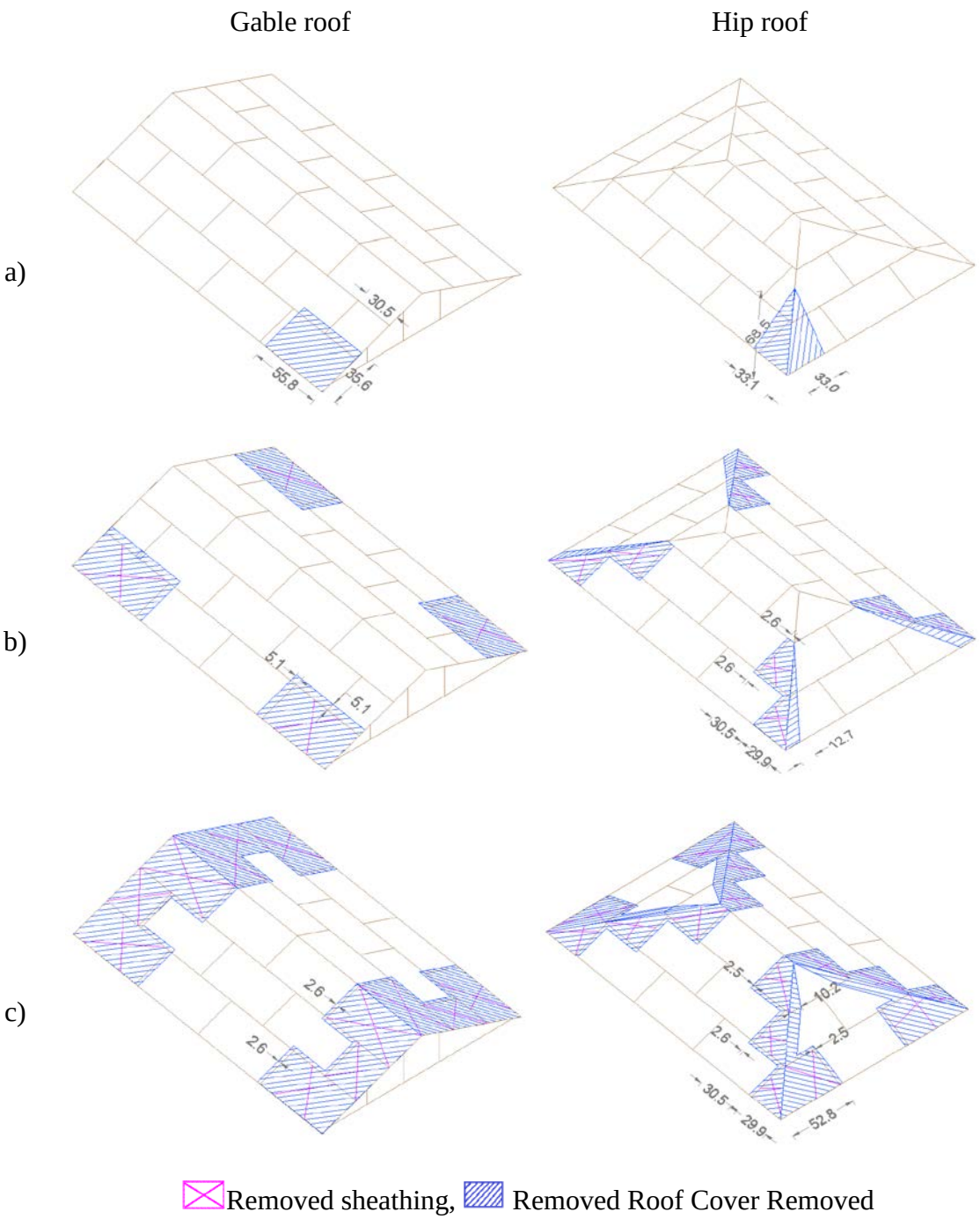

Figure 19. Gable and hip roof breaches at (a) light damage, (b) minor damage and (c) moderate damage states (scaled model dimensions in cm)

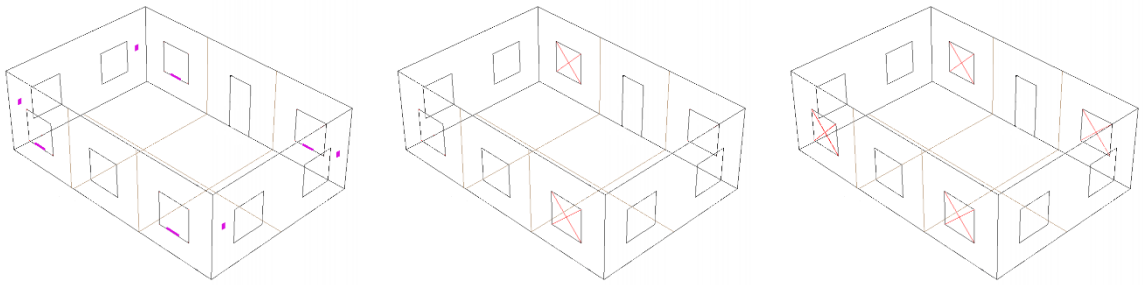

(a) (b) (c)

Figure 20. Wall breaches at (a) light damage, (b) minor damage and (c) moderate damage states (full *scale dimensions)*

3.4. Model Preparation

As shown in Figure 21, the 1:4 scaled models were built out of wood. The building roof was constructed by attaching the 0.3 × 0.61 m^2 plywood pieces on the roof's wooden frame. These plywood pieces were the 1:4 scaled-down models of 4 by 8 plywood sheathing that is commonly used in residential building construction. This modeling approach simulated the roof sheathing removal by removing the plywood sheathing pieces, and roof cover removal by unsealing the gap between the plywood sheathing pieces (Figure 22).

(a) (b)

Figure 21. 1:4 scaled models out of wood, (a) hip and (b) gable

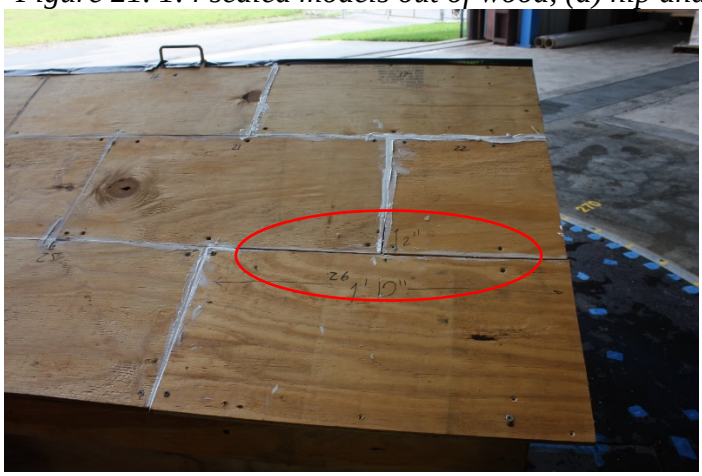

Figure 22. The unsealed gap between the sheathing

To accurately simulate the internal wind flow and to distinguish between the roof and wall water ingress, the attic space was separated from the room compartments by the plywood ceiling. Each of the six attic compartments was connected to a distinct bucket using a plastic tube. Therefore, the water that reached the attic compartments was separately accumulated in six buckets. These buckets were weighed at the end of each test to obtain the amount of water reaching each attic compartment (Figure 23). The same method was used to separately measure the amount of water reaching the floor on each of the room compartments.

Figure 23. Water collection buckets

As shown in Figure 24, the internal walls were coved by superabsorbent pads, and the volume of water that reached each wall surface was measured based on the weight of absorbed water by the pad during the test. Additionally, the infrared camera was used to better observe the water traces across the surface of the walls.

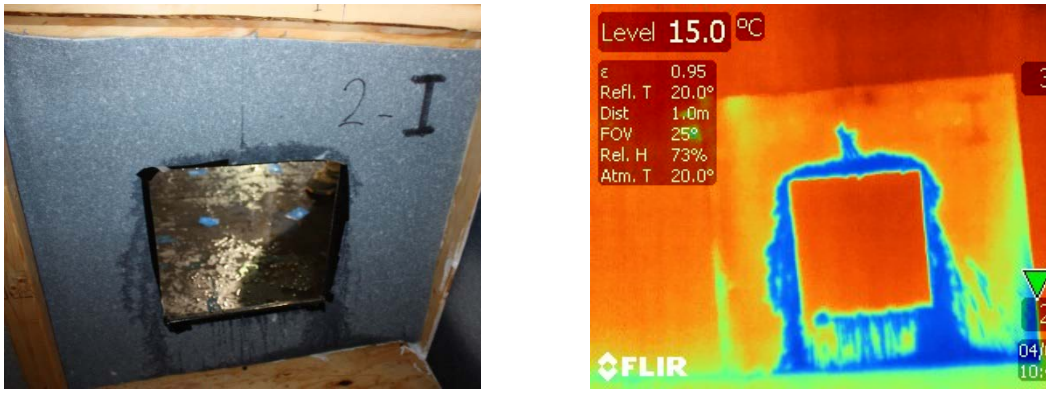

(a) (b)

Figure 24. Superabsorbent pads covering the interior wall and the infrared photo

Each roof type model (i.e. gable and hip) was prepared for each of the three damage states (i.e. light damage, minor damage, and moderate damage) and was tested at three different wind angles (i.e. 0°, 45° and 90°)—see Figure 25. During each test, the model was subjected to 5 minutes of WDR. After each test, the buckets and pads were

weighed to measure the amount of water reaching each interior component, and infrared photos were taken off the pads. Each test was performed at the wind speed of 13.41 m/s and rain rate of 86 mm/hr at the roof eave height of the model.

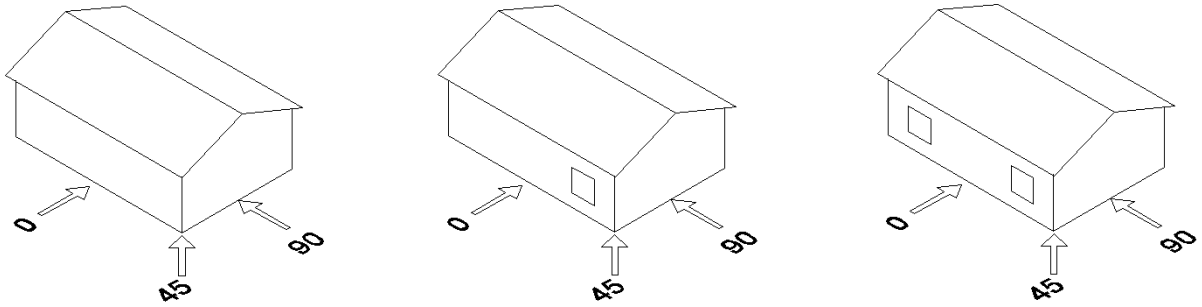

DS0 DS1 DS2

Figure 25. Wind direction notation for each damage state

3.5. Test Results and Discussions

The results of the large-scale experimental investigation of the water propagation inside the building are presented in this section. As explained earlier in this chapter, the tests were performed for eighteen model configurations, including two roof types, three damage states and three wind angles of attack. The next three subsections explain the results for the light, minor and moderate damage states, respectively. For each subsection, the results for water accumulation on the room and attic compartments are discussed, separately.

3.5.1. Light Damage State

For the light damage state configuration, since the area of the envelope defects is very small, it was expected that the direct impinging rain into the building interior would

have a minimal effect on the water propagation path inside the building. Additionally, since the internal wind flow is negligible, the gravity is the main propeller for the water propagation inside the building. In this case, it was expected that the major mode of water propagation is the water runoff on the interior walls below the opening toward the floor.

3.5.1.1 Room compartments

The water propagation inside the room compartments of the light damage state models is presented in Figure 26. This figure shows the amount of water that reaches each interior surface (i.e. wall and flooring), for gable and hip roof models subjected to 0˚, 45˚ and 90˚ wind angels of attack. For all cases, the mode of water propagation is the water runoff on the defected wall surface from the opening toward the floor. As expected, the water trace can only be observed on the windward defected walls and flooring below them.

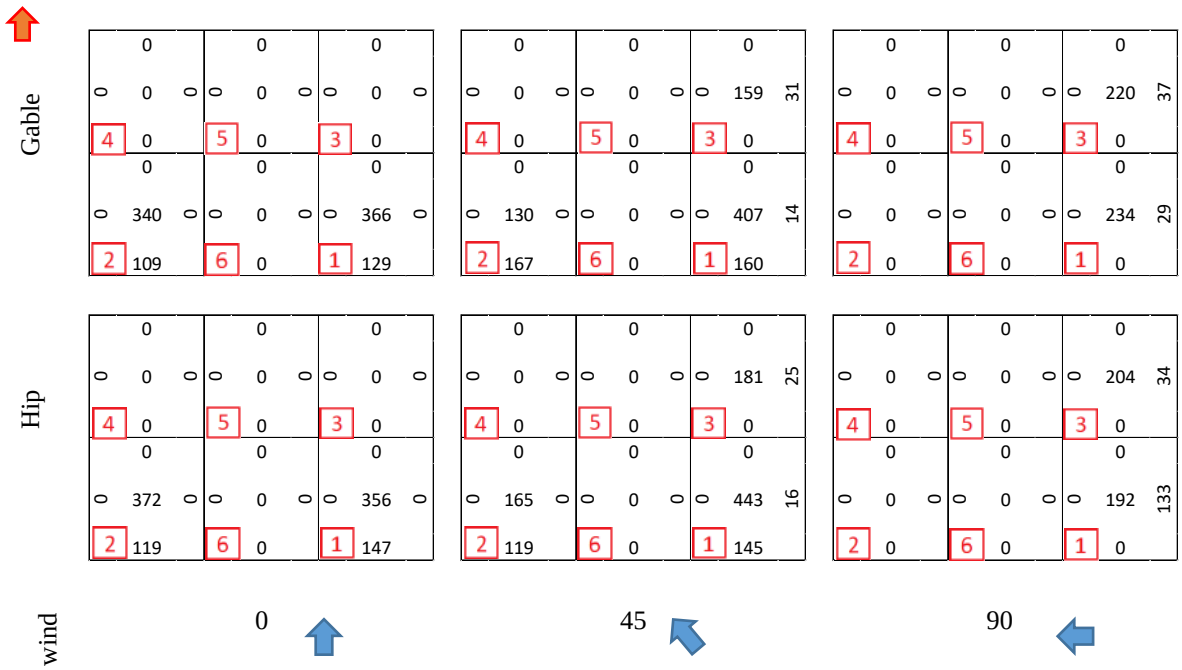

Figure 26. Room compartments' numbering and water propagation into interior walls and floorings in grams, for the light damage state model

3.5.1.2 Attic compartments

Figure 27 shows the water propagation into the attic compartments of the light damage state models. The results are separately presented for gable and hip roof models, as well as 0°, 45°, and 90° wind directions. In this case, also, the area of the roof openings is very small, and as a result, the internal wind flow is too weak to govern the internal water propagation. Therefore, the gravity is the major force that controls the movement of the infiltrated water through the roof openings. This results in the attic compartment directly below the roof defect (roof compartment 1) being the only affected attic compartment.

For the gable roof model, the highest amount of water accumulation occurs at the 0° wind angle. This wind direction results in more surface runoff water at the roof

opening compared to the 45˚ and 90˚ wind directions, where flow separation at the roof edge deviates the runoff water flow from the opening.

The 0° wind direction results in the highest amount of water intrusion into the hip roof's attic. The wind flow, in this case, pushes the runoff water from the center line of the windward roof surface toward the hip lines. Since the roof defect is located on the hip line, a part of this runoff water can infiltrate through the opening and get into the attic. Similarly, at the 90° wind direction, the runoff water is directed toward the hip lines by the wind flow. However, in this case, the area of the windward roof surface is smaller compared to the windward roof surface at the 0˚ wind angle, which results in a lower volume of surface runoff water at the roof opening. As a result, the amount of water that gets into the attic at the 90˚ wind direction is smaller compared to 0˚. However, at the 45˚ wind direction, a different flow path is observed for the runoff water. In this case, the wind flow directly hits the defected hip line and pushes the runoff water away from the hip line toward the centers of the windward roof surfaces, and results in the minimum amount of water infiltration.

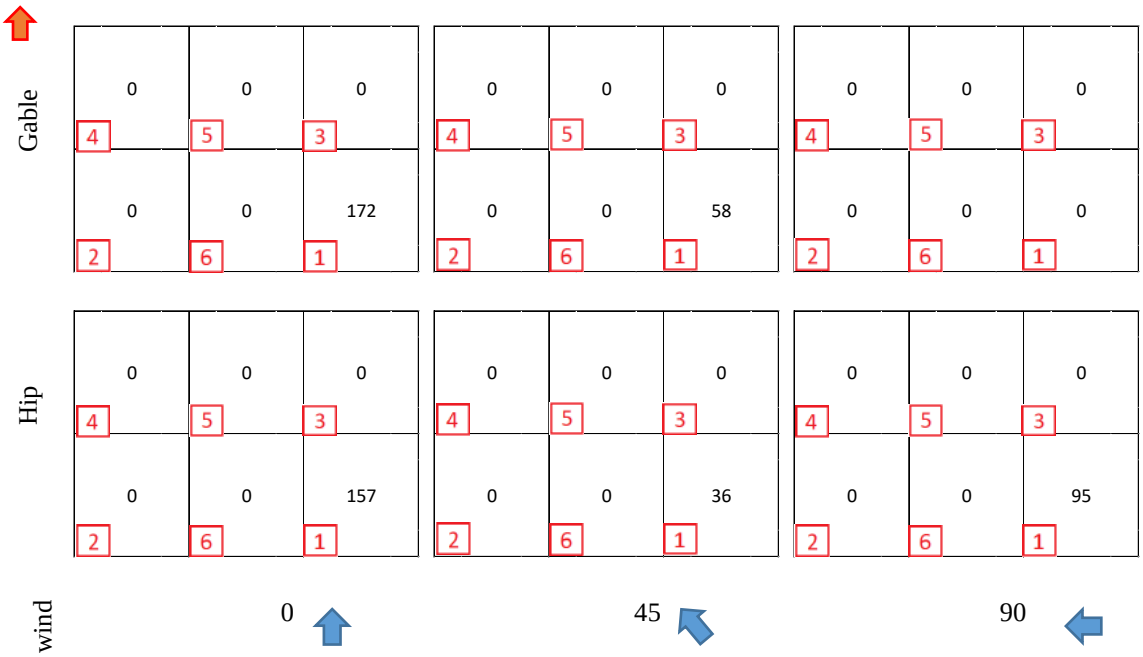

Figure 27. Attic compartments' numbering and water propagation in grams, for the light damage state model

3.5.2. Minor Damage State

The exterior openings of the model at the minor damage state were large enough to allow direct impinging rain into the building interior, as well as the internal wind flow. It was expected that any of the interior walls of the room compartments with an opening experience the water trace on their surfaces. Similarly, water accumulation could occur on any attic compartment.

3.5.2.1 Room compartments

The water propagation inside the room compartments of the minor damage state model is presented in Figure 28. The results are displayed separately for two roof types (i.e. gable and hip) and three wind angles (0°, 45°, and 90°).

At the 0˚ wind angle of attack, for both gable and hip roof models, the least amount of water (less than 1%) is absorbed by the west wall of room compartment 1. At

this wind angle, the wind hits the south wall perpendicularly, and then it is redirected toward the east and west edges of the building. As the wind flows from the vertical center line of the windward wall toward the building edges, it enters through the window opening with an inclined angle directing toward the northeast corner of the room compartment 1 (Figure 29). This inclined direction of the internal wind flow is the reason for the minimum amount of water absorption by the west wall of room compartment 1. The infrared photos shown in Figure 30 also depict this explanation. As can be observed from these photos, only a slight amount of water can be noted on the west wall, while the trace of water on the east and north wall expands to the same height as the window's top edge. For the south wall, in addition to the wet area below the window, a narrow margin of moisture trace can be noted around the window.

The 45˚ wind direction results in a minimum amount of water absorption by the east wall of room compartment 1 (1% of the total intruded water into the room compartment) for both gable and hip roof types. The maximum amount of water absorption occurs at the west wall, with 26% and 30% of the total intruded water for gable and hip roof models, respectively. In this case, the external wind flow enters the room compartment 1 through the window opening with an inclined angle toward the west wall (Figure 31). As shown in Figure 32, the infrared photos support this rationale. The west wall, which is the direct target of the wind flow, gets wet up to almost the same height as the top edge of the open window, while the moisture trace can only be observed on the left side of the north wall (the side closer to the west wall). Similarly, the bottom left corner of the south wall (the corner adjacent to the west wall) is the location where a

notable moisture trace is observed. Finally, and as expected, the east wall is barely affected by the water.

For the 90˚ wind direction, non-traceable water absorption is recorded at all interior surfaces for both gable and hip roof models. In this case, there is no opening on the exterior windward wall to allow water intrusion into the room compartments.

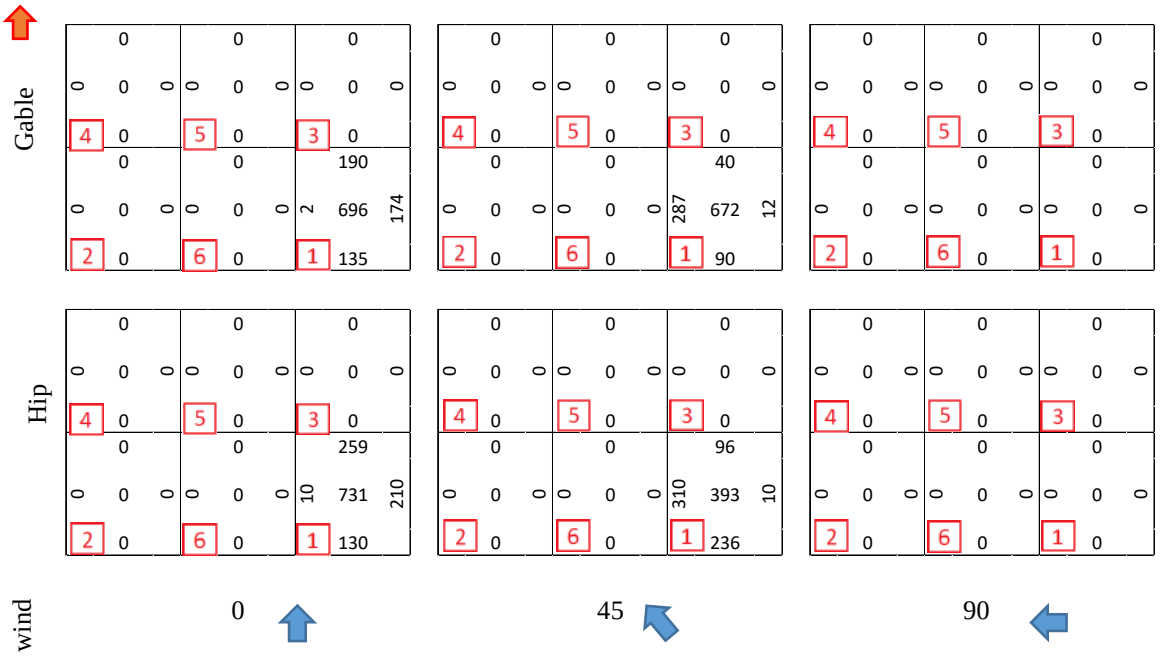

Figure 28. Room compartments' numbering and water propagation into interior walls and floorings in grams, for the minor damage state model

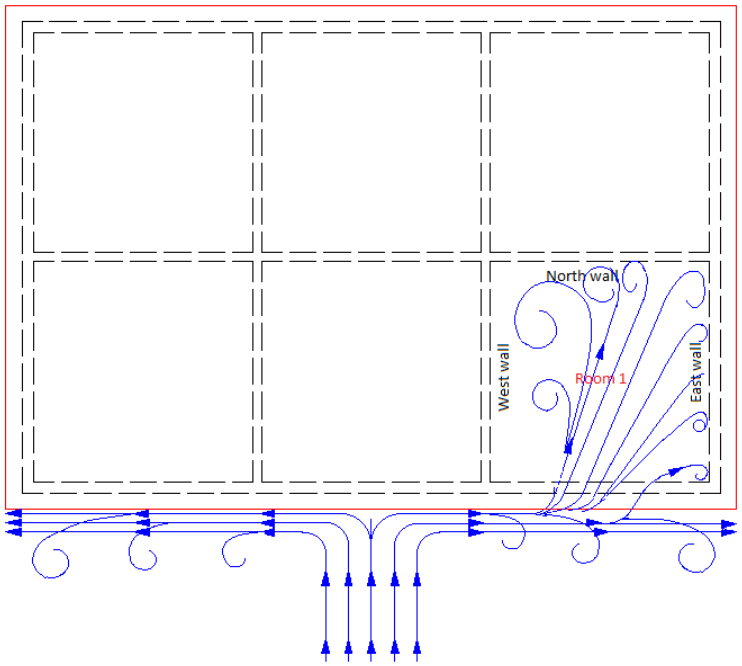

Figure 29. Schematic view of wind flow at a 0° wind direction

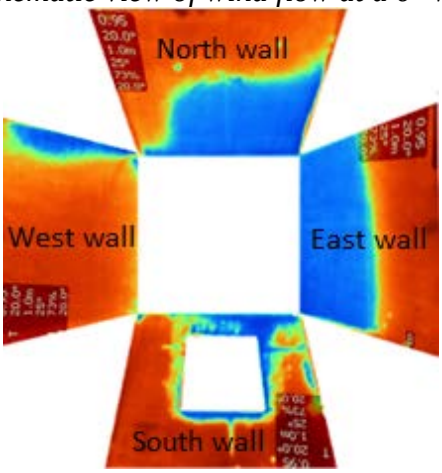

Figure 30. Infrared photos of the walls of room compartment 1, subjected to a 0° wind direction

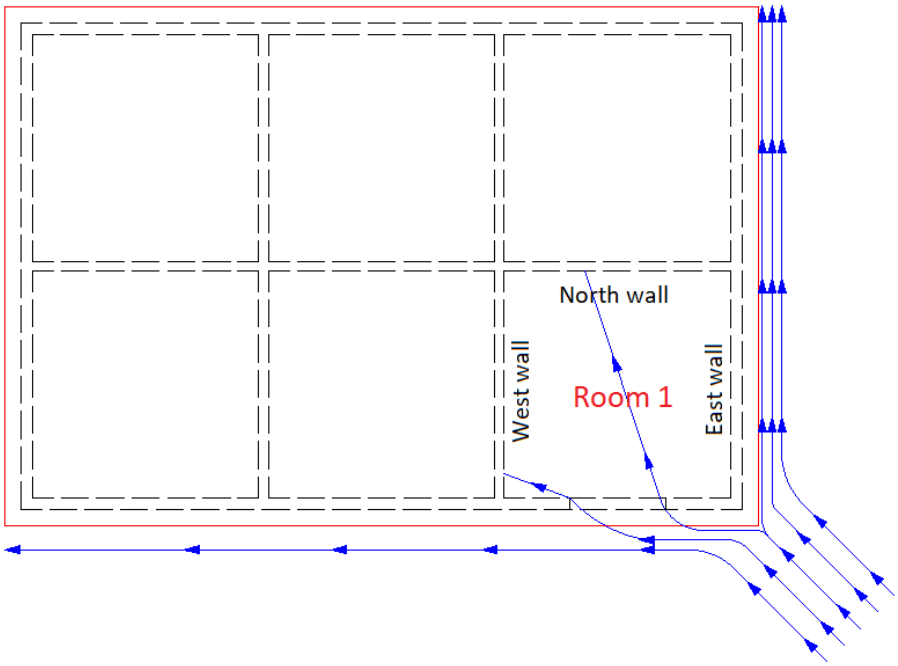

Figure 31. Schematic view of wind flow at a 45° wind direction

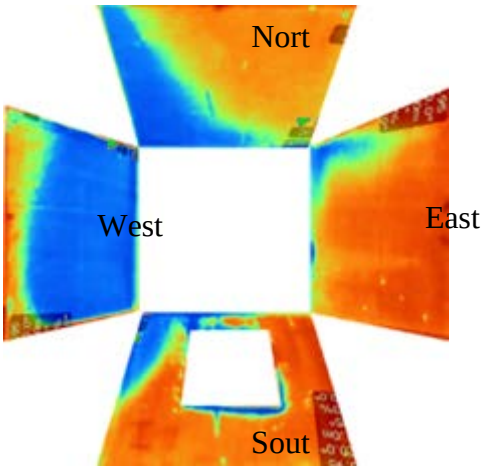

Figure 32. Infrared photos of the walls of room compartment 1, subjected to 45° wind

3.5.2.2 Attic compartments

Figure 33 shows the water propagation into different attic compartments of the gable and hip roof models subjected to wind angles of 0°, 45°, and 90°. The 0˚ wind direction results in the highest amount of water deposition on the attic compartment 1 and

2 for both gable and hip roof models. These are the immediate attic compartments exposed to the wind flow, therefore significant amount of water intrusion—73% and 95% of the total ingress water into the gable and hip roof, respectively—was expected. Also, for both gable and hip roof models, the symmetric configuration of the model for the 0˚ wind angle should result in similar amount of water accumulation on the attic compartments 1 and 2. As expected in the case of the gable roof model, there is only 1% difference between the accumulated water on room compartments 1 and 2. However, for the hip roof model, the difference between the recorded water for compartments 1 and 2 is 11%. This difference might be caused by the minor details in the physical model. As explained earlier, the models were built out of wood and, because of the nature of the water flow, even minor cracks or uneven sheathing surface could change the water flow path and result in different amount of water accumulation on the attic compartments 1 and 2. This justification was affirmed by the observation of the water flow path on the roof surface. This observation showed how minor physical details can change the water flow path (Figure 34).

The attic compartments 1 and 2 of the gable roof model are the ones with the highest amount of water accumulation at 45˚ wind direction. In this case, 35% and 36% of the total ingress water through the gable roof openings are accumulated at attic compartments 1 and 2, respectively. When the hip roof model is tested at the 45˚ wind direction, the attic compartment 2 receives the highest amount of water (38% of the total ingress water).

As shown in Figure 33, the least amount of water intrusion through the gable roof openings occurs at the 90˚ wind angle of attack. At this wind direction, the flow separation at the gable end results in the minimum amount of direct impinging rain into the roof openings located upstream of the wind flow. On the other hand, the wind flow reattachment to the roof surface downstream of the flow pushes the surface runoff water toward the west side roof openings. Similar results were obtained by Baheru, 2014, for the rainwater deposition on the building envelope.

For the hip roof model subjected to the 90˚ wind direction, the attic compartments 1 and 3, with 40% and 44% of the total amount of water intrusion through the roof, are those with the highest amount of water accumulation. In this case, the roof openings above compartments 1 and 3 are parallel to the wind flow, rather than being directly exposed to it. However, the wind flow pushes the surface runoff water on the windward roof surface (east roof side) toward the hip lines and results in water infiltration into the attic compartments 1 and 3.

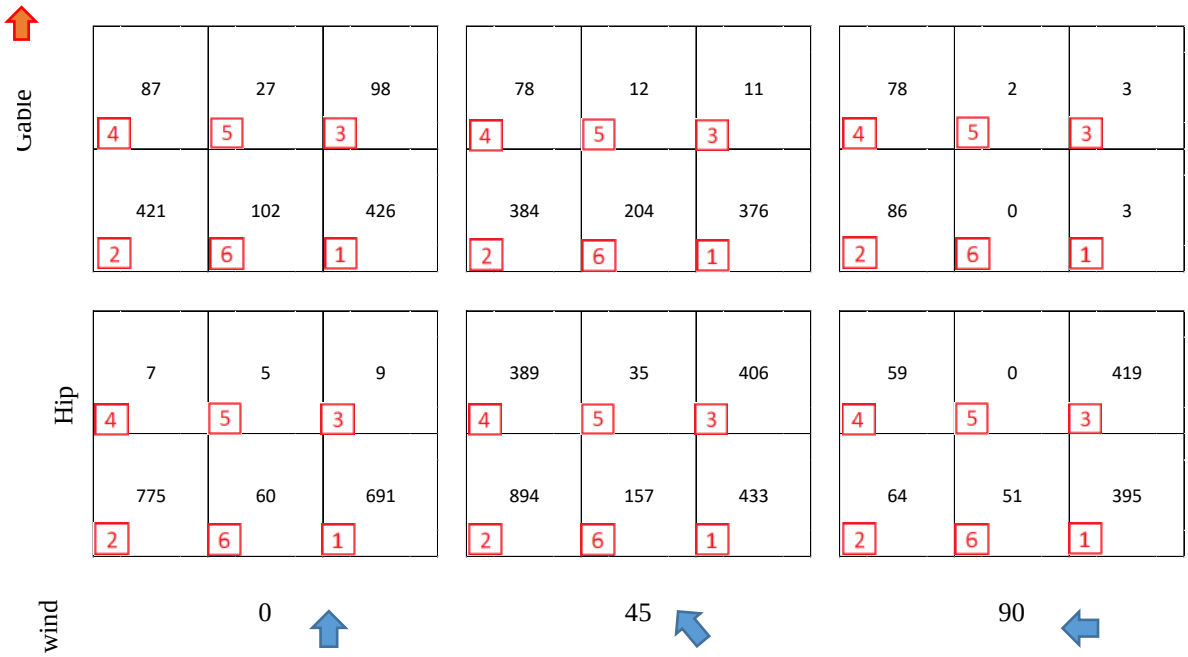

Figure 33. Attic compartments' numbering and water propagation in grams, for the minor damage state model

Figure 34. Water path on the model affected by the construction details

3.5.3. *Moderate Damage State*

This section explains the water propagation into the room and attic compartments of the moderate damage state model. Similar to the case of the minor damage state, the envelope openings in the moderate damage state model are also large. Therefore, the

direct impinging and internal wind flow significantly affects the moisture propagation on the interior surfaces, as will be further discussed in this section.

3.5.3.1 Room compartments

The water distribution into the room compartments of the moderate damage state model is presented in Figure 35. The results are shown for two roof type models (i.e. gable and hip) and three wind directions (i.e. 0˚, 45˚ and 90˚).

The same water propagation pattern as the one for the minor damage state can be noted for the room compartment 1 for the moderate damage state at the 0° wind angle. Similarly, the west wall of room compartment 1 attracts the least amount of water. For the gable roof model, only 5.7% of the total ingress water into the room compartment 1 reaches the west wall, and for the hip roof model, this wall has only a 0.5% share of the total ingress water. The mirrored water propagation pattern can be observed for the room compartment 2, which was expected based on the symmetric configuration of the model with respect to the wind direction. Therefore, the east wall of room compartment 2 is the one with the least share of water absorption. As shown in Figure 36, the 0° wind flow is perpendicular to the south wall, and once it hits the building the flow is redirected toward the east and west side of the building. The internal wind flow has an inclined angle toward the east wall of room compartment 1 and west wall of room compartment 2, rather than directly targeting the interior north walls. The infrared photos also agree with these observations. As shown in Figure 37-a, the west wall of the room compartment 2 gets wet up to the same height as the opening top edge. The moisture trace extends to the west side of the north wall, then gradually fades near the east side of this wall and leaves

only a thin line on the east wall, where it finally disappears. The mirror of the same pattern can be observed in the room compartment 2, as shown in Figure 37-b.

For the 45˚ wind direction, the water distribution in the room compartment 1 is very similar to what was observed for the minor damage state. The notable observation in both cases is that the west wall attracts more water compared to the rest of the interior wall. For the gable roof model, the water absorbed by the west wall is 27% of the total intruded water into room compartment 1, and for the hip roof model, this amount equals 34%. As discussed in the minor damage state, the inclined direction of the internal wind flow toward the west wall is the reason for this observation (Figure 38). The very same thing happens for the room compartment 2, and the west wall absorbs the highest amount of water. However, in this case, the amount of intruded water is generally lower compared to the room compartment 1. This can be justified by the less strong internal wind flow inside the room compartment 2 compared to room compartment 1. The less powerful wind flow can result in a lesser amount of water deposition on the interior surfaces.

The thermography results agreed well with this reasoning. Figure 39 shows the notable trace of moisture on the west walls of room compartments 1 and 2. It can also be noted that the extent of the moist area is smaller on the west wall of room compartment 2 compared to room compartment 1. The trace on the west wall fades as it gets closer to the north wall, especially in the room compartment 2. However, it leaves an inclined pattern on the north wall and finally disappears on the east wall.

The 90˚ wind direction does not allow any traceable water intrusion into the building interior since there is no envelope opening on the windward exterior walls in this case. This is the reason for the zero values recorded on the interior walls and floorings for the moderate damage state model subjected to the 90˚ wind angle of attack.

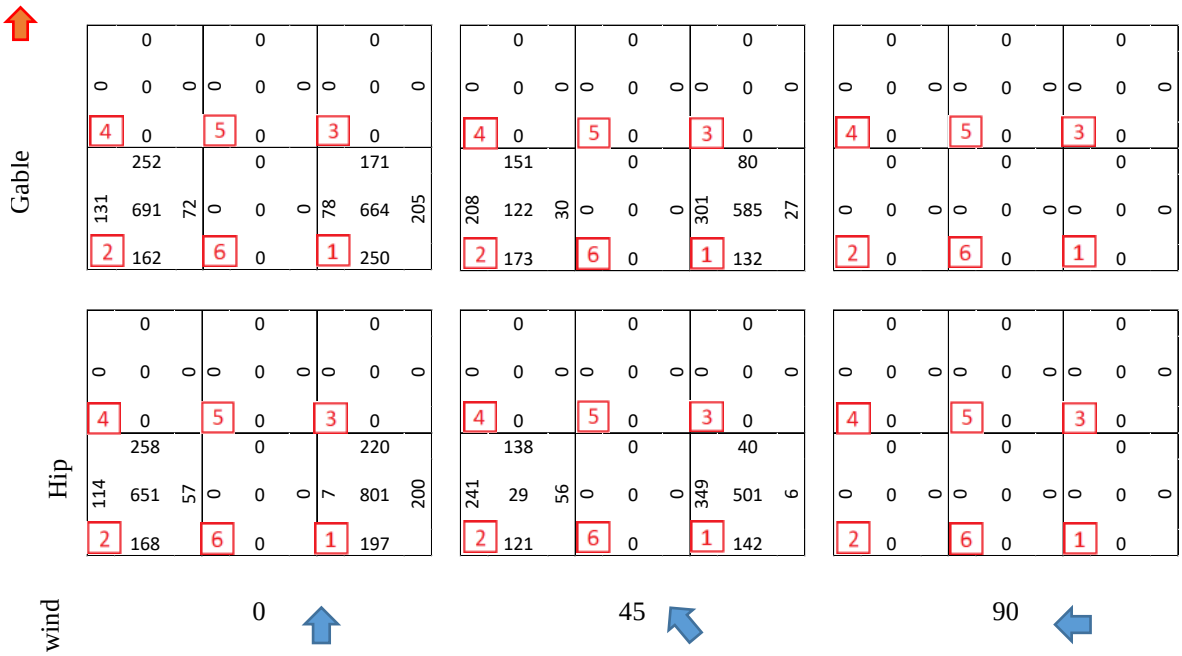

Figure 35. Room compartments' numbering and water propagation into interior walls and floorings in grams, for the moderate damage state model

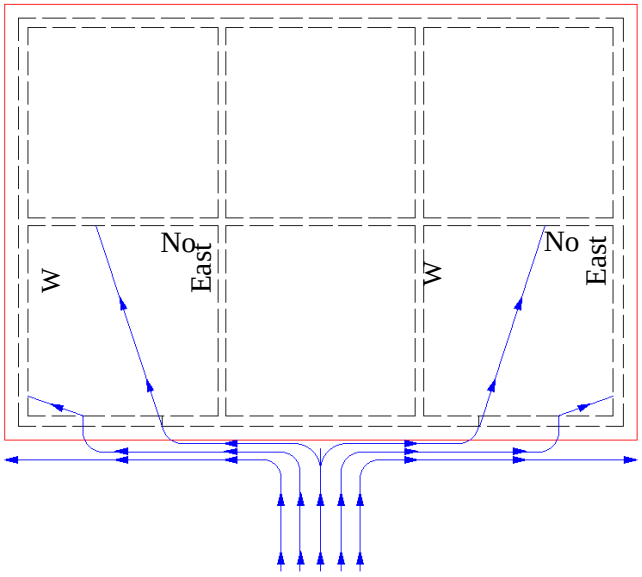

Figure 36. Schematic view of wind flow at the 0° wind direction

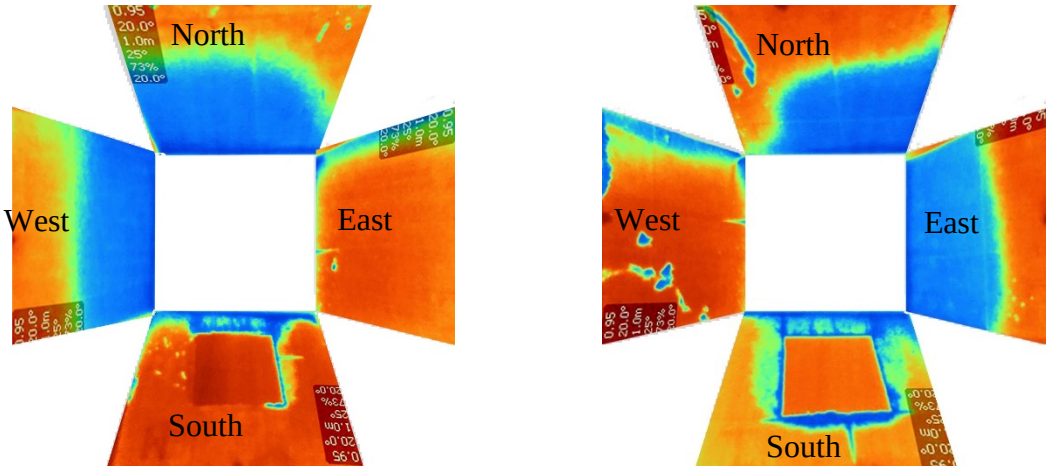

(a) Room compartment 2 (b) Room compartment 1

Figure 37. Infrared photos of the walls of room compartments 1 and 2, subjected to the 0° wind direction

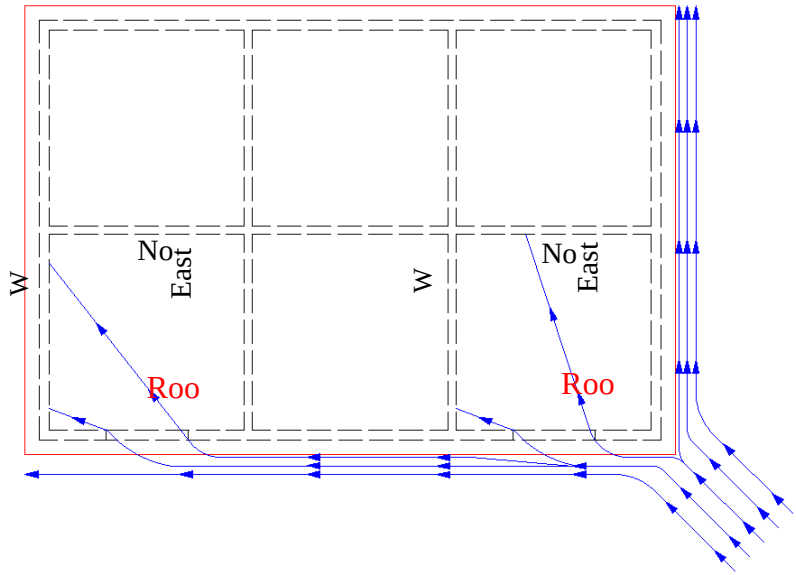

Figure 38. Schematic view of wind flow at 45° the wind direction

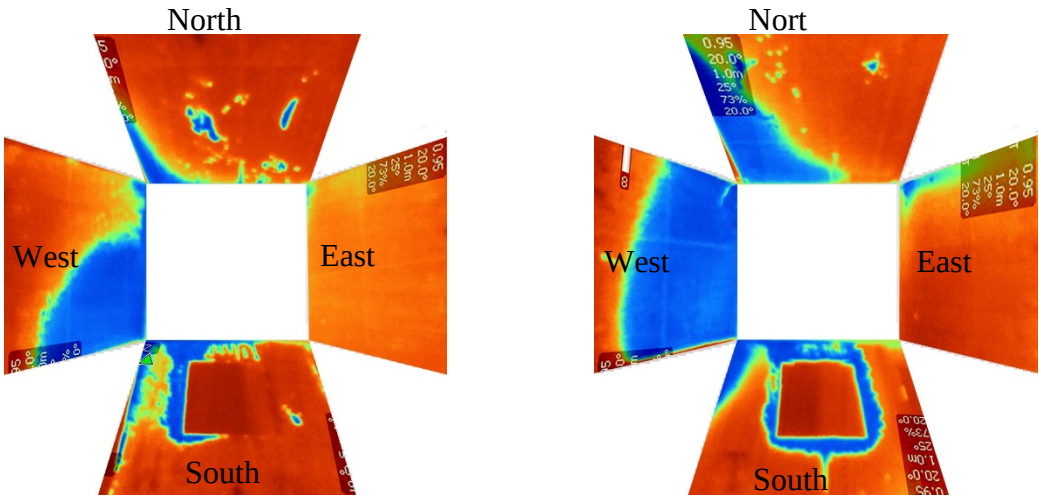

(a) Room compartment 2 (b) Room compartment 1

Figure 39. Infrared photos of the walls of room compartments 1 and 2, subjected to the 45° wind direction

3.5.3.2 Attic compartments

Figure 40 displays the findings of the experimental tests on the distribution of water into the attics of the gable and hip roof models subjected to the 0˚, 45˚ and 90˚ wind angles of attack. It can be noted that the attic compartments 1 and 2 are the ones that attract the highest amount of water at the 0° wind direction. For the gable roof model, 76% of the total intruded water through the roof openings is accumulated on only these two compartments. For the hip roof, these two compartments attract 83% of the total ingress water through the roof. Another notable observation is that for the gable roof model subjected to the 0˚ wind direction, the middle attic compartments (compartments 5 and 6) attract no water at all. This might be due to the undisturbed interior wind flow inside the damaged gable roof. In this case, the model configuration allows for the direct flow of the wind through the attic without deviating from its normal to ridge direction.

At the 45˚ wind angle, the attic compartment 2 attracts the highest amount of water, which is 39% and 23% of the total ingress water into the gable and hip roof models, respectively. This attic compartment is subjected to a considerable amount of direct impinging rain, as well as the surface runoff water in both gable and hip roof models at the 45˚ wind direction, which justifies the considerable amount of water accumulation.

The attic compartments of gable roof model experience a minimal water intrusion at the 90° wind angle. At this wind direction, the flow separation at the gable end prevents the raindrops from getting through the roof openings into the attic compartments. However, the same wind direction results in a considerable amount of water accumulation on the attic compartments 1 and 3 of the hip roof model. These attic compartments can attract both the direct impinging rain and the surface runoff water on the windward roof side. Also, it should be noted that almost the same amount of water is accumulated in these two compartments (only a 6% difference), which could be expected based on the symmetric configuration of the model with respect to the wind angle.

Figure 40. Attic compartments' numbering and water propagation in grams (% of total water intruded through roof openings), for the moderate damage state model

3.6. Implementation into FPHLM

This section explains how the raw results of the experimental large-scale tests are processed so that they can be implemented into the FPHLM model. One of the objectives of this research was to obtain experimental data that can be used to improve the interior loss estimation module of the FPHLM program. The current FPHLM model can estimate how much water can intrude into the building interior, but it cannot calculate how this water is distributed among different interior components. By implementing the experimental water propagation results into the FPHLM program, it can be modified to calculate the amount of water that reaches each interior component and estimate the sustained loss based on this information.

To implement the experimental results to the FPHLM program, the obtained data needed to be modified. To understand the necessity of these modifications requires a

brief introduction to the FPHLM procedure for the calculation of the amount of water intrusion into the building interior. The current method applied in the FPHLM for the evaluation of the amount of water intrusion is summarized in the following paragraphs. More comprehensive information on the procedure can be found in the literature (Johnson, 2015, Johnson et al., 2018, G. L. Pita, 2012 and G. Pita et al., 2012).

The assumptions made by the FPHLM regarding the calculation of the amount of water intrusion into the building interior can be summarized as follows:

- The wind speed during a hurricane event is variant. The hurricane starts with a, low wind speed then at some point it reaches the maximum wind speed of V_{max}.
- For a given building model, a specific maximum wind speed is associated with any of the predefined damage states (section 3.3) depending on the construction type of the building. In other words, a minimum value of V_{max} is required to generate a specific level of the exterior damage state (e.g. DS0, DS1 or DS2) depending on the building construction type. This is based on the idea that the stronger the building construction, the higher the wind speed required for generating the same level of exterior damage.
- Before the occurrence of V_{max}, there was not any wind-induced damage on the building envelope caused by the pertinent hurricane. Therefore, the water intrusion occurs only at the pre-existing openings, including the building defects and the roof damages that have occurred during the previous low wind speed events. The model configuration at Damage State 0 in the experimental tests corresponds to the envelope opening in this situation.

- The occurrence of V_{max} results in the generation of wind-induced damages on the building envelope, unless the V_{max} is lower than the wind speed associated with the DS0 (which means the value of V_{max} has been too low to generate the exterior damage). In the case that V_{max} is large enough to result in wind-induced exterior damages on the building envelope, the water intrusion after V_{max} occurs, at both pre-existing defects and wind, induces exterior breaches. However, the simultaneous water intrusion through the envelope defects and breaches was not considered in the experimental tests, so there is a need to apply the modification to the test results to include the water ingress through the defects and wind-induced breaches at the same time. Section 3.6.1 describes how these modifications are applied to the experimental test results.
- In the FPHLM model, it is assumed that during a hurricane event the hurricane eye rotates around the building and, as a result, the wind angle of attack can change from 0˚ to 315˚ in 45 ˚ increments (8 octants). At each wind direction, the water can intrude into the building through the existing envelope breaches, so it is necessary to determine the water propagation inside the building for each of the eight wind angle of attacks (octants). Section 3.6.2 explains how the water propagation data are developed for eight octants, and how this data will be implemented into the FPHLM model.

3.6.1. Generalization of the experimental test results

As mentioned earlier, the experimental tests did not account for the water intrusion at defects. In other words, the model configuration for DS1 and DS2 did not include the envelope defects (the existing opening in the DS0). Instead, they only

incorporated the wind-induced breaches associated with DS1 or DS2. On the other hand, in reality (also in the FPHLM model), once the wind induced-damages occur on the building envelope, the water can intrude not only through these breaches but also through the pre-existing defects. To include this effect in the experimental test results, it was decided to add the volume of water intruded during the DS0 experimental tests to the amount of water accumulated during DS1 to obtain the total volume of water intrusion at DS1 through both defects and breaches. Similarly, for DS2, the volume of intruded water during DS0 was added to the amount of water intrusion during DS2.

However, there were some matters that should have been considered for the procedure of adding DS0 results to DS1 or DS2 results. For example, if there was a defect in DS0 at a window that was assumed to be broken in the DS1 or DS2 model, the volume of water intrusion through that defect in the DS0 test should have not been added to the volume of water intrusion through the broken window at that location in the DS1 or DS2 tests. The reason is that once the whole window breaks, the amount of surface runoff water in the DS0 case that intruded through the defects now can impinge inside the building and is included in the water intrusion obtained by DS1 or DS2. Therefore, adding the volume of water at DS0 to the DS1 or DS2, in this case, results in double-counting the amount of intruded water. Also, for the roof water intrusion, the area of the roof opening at DS1 and DS2 covered the area of roof opening at the DS0 model, so there was no need to add the water intrusion at DS0 to the water intrusion at DS1 or DS2. Table 6 summarizes the water intrusion results after this modification. In the first column, P1 to P24 refer to the interior partitions, while F1 to F6 and C1 to C6 refer to Flooring

and Ceiling components, respectively. The naming convention of the interior components is shown in *Figure* 41.

Table 6. The modified volume of water reaching different interior components at different model configurations

Interior component	Volume of water reaching each interior component (ml)																	
	Hip-DS0-0°wind	Hip-DS0-45°wind	Hip-DS0-90°wind	Gable-DS0-0°wind	Gable-DS0-45°wind	Gable-DS0-90°wind	Hip-DS1-0°wind_modified	Hip-DS1-45°wind_modified	Hip-DS1-90°wind_modified	Hip-DS2-0°wind_modified	Hip-DS2-45°wind_modified	Hip-DS2-90°wind_modified	Gable-DS1-0°wind_modified	Gable-DS1-45°wind_modified	Gable-DS1-90°wind_modified	Gable-DS2-0°wind_modified	Gable-DS2-45°wind_modified	Gable-DS2-90°wind_modified
P1	147	145	0	129	160	0	130	236	0	197	142	0	135	90	0	250	132	0
P2	0	0	0	0	0	0	10	310	0	7	349	0	2	287	0	78	301	0
P3	0	0	0	0	0	0	259	96	0	220	40	0	190	40	0	171	80	0
P4	0	16	133	0	14	29	210	26	133	200	22	133	174	26	29	205	41	29
P5	119	119	0	109	167	0	119	119	0	168	121	0	109	167	0	162	173	0
P6	0	0	0	0	0	0	0	0	0	114	241	0	0	0	0	101	208	0
P7	0	0	0	0	0	0	0	0	0	258	138	0	0	0	0	252	151	0
P8	0	0	0	0	0	0	0	0	0	57	56	0	0	0	0	102	30	0
P9	0	25	34	0	31	37	0	25	34	0	25	34	0	31	37	0	31	37
P10	0	0	0	0	0	0	0	0	0	0	0	0	0	0	0	0	0	0
P11	0	0	0	0	0	0	0	0	0	0	0	0	0	0	0	0	0	0
P12	0	0	0	0	0	0	0	0	0	0	0	0	0	0	0	0	0	0
P13	0	0	0	0	0	0	0	0	0	0	0	0	0	0	0	0	0	0
P14	0	0	0	0	0	0	0	0	0	0	0	0	0	0	0	0	0	0
P15	0	0	0	0	0	0	0	0	0	0	0	0	0	0	0	0	0	0
P16	0	0	0	0	0	0	0	0	0	0	0	0	0	0	0	0	0	0
P17	0	0	0	0	0	0	0	0	0	0	0	0	0	0	0	0	0	0
P18	0	0	0	0	0	0	0	0	0	0	0	0	0	0	0	0	0	0
P19	0	0	0	0	0	0	0	0	0	0	0	0	0	0	0	0	0	0
P20	0	0	0	0	0	0	0	0	0	0	0	0	0	0	0	0	0	0
P21	0	0	0	0	0	0	0	0	0	0	0	0	0	0	0	0	0	0
P22	0	0	0	0	0	0	0	0	0	0	0	0	0	0	0	0	0	0
P23	0	0	0	0	0	0	0	0	0	0	0	0	0	0	0	0	0	0
P24	0	0	0	0	0	0	0	0	0	0	0	0	0	0	0	0	0	0
F1	356	443	192	366	407	234	731	615	192	801	723	192	696	876	234	664	789	234
F2	372	165	0	340	130	0	372	165	0	651	29	0	340	130	0	691	122	0
F3	0	181	204	0	159	220	0	181	204	0	181	204	0	159	220	0	159	220
F4	0	0	0	0	0	0	0	0	0	0	0	0	0	0	0	0	0	0
F5	0	0	0	0	0	0	0	0	0	0	0	0	0	0	0	0	0	0
F6	0	0	0	0	0	0	0	0	0	0	0	0	0	0	0	0	0	0
C1	157	36	95	172	58	0	691	433	395	1306	828	1026	426	376	3	1516	810	24
C2	0	0	0	0	0	0	775	894	64	1212	911	68	421	384	86	1536	1456	0
C3	0	0	0	0	0	0	9	406	419	44	839	1089	98	11	3	506	327	28
C4	0	0	0	0	0	0	7	389	59	49	379	54	87	78	78	471	806	10
C5	0	0	0	0	0	0	5	35	0	138	418	27	27	12	2	0	324	0
C6	0	0	0	0	0	0	60	157	51	271	631	0	102	204	0	0	10	0

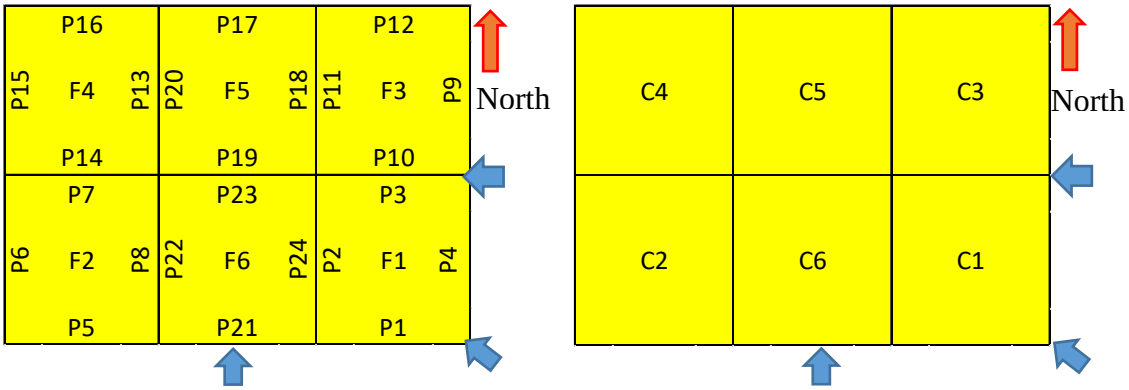

(a) (b)

Figure *41. The naming convention for (a) interior partition and flooring components, and (b) ceiling components*

It should be noted that for the FPHLM implementation, it is important to use the normalized share of each interior component so that the results can be used for any duration of rain and amount of total water intrusion. In other words, the results should be presented as the share of each interior components form the total volume of intruded water, so that the volume of the water reaching each component can be calculated for any given value of water intrusion. Because the water intrusion from the roof openings was separately measured from the water intrusion from the wall openings in the experimental tests, it was decided to use total volume of water intrusion through the wall opening for normalizing the results of room components and total volume of water intrusion through the ceiling for the normalization of the ceiling components. Therefore, the experimental results were normalized to present the share of each interior room compartment (P1 to P24 and F1 to F6) from the total volume of water that intrudes through the wall openings. Similarly, for the ceiling components (C1 to C6), the volume of water at each ceiling component was normalized to the total volume of water that intrudes through the roof opening. The figure below presents the normalized results for each interior component at

each model configuration. The location of the interior compartments is shown in *Figure* 41.

Table 7. The normalized share of different interior components at different configurations

	Normalized share of different interior components																	
Interior component	Hip-DS0-0°wind	Hip-DS0-45°wind	Hip-DS0-90°wind	Gable-DS0-0°wind	Gable-DS0-45°wind	Gable-DS0-90°wind	Hip-DS1-0°wind_modified	Hip-DS1-45°wind_modified	Hip-DS1-90°wind_modified	Hip-DS2-0°wind_modified	Hip-DS2-45°wind_modified	Hip-DS2-90°wind_modified	Gable-DS1-0°wind_modified	Gable-DS1-45°wind_modified	Gable-DS1-90°wind_modified	Gable-DS2-0°wind_modified	Gable-DS2-45°wind_modified	Gable-DS2-90°wind_modified
P1	15%	13%	0%	14%	15%	0%	7%	13%	0%	7%	7%	0%	8%	5%	0%	9%	6%	0%
P2	0%	0%	0%	0%	0%	0%	1%	17%	0%	0%	17%	0%	0%	16%	0%	3%	14%	0%
P3	0%	0%	0%	0%	0%	0%	14%	5%	0%	8%	2%	0%	12%	2%	0%	6%	4%	0%
P4	0%	1%	24%	0%	1%	6%	11%	1%	24%	7%	1%	24%	11%	1%	6%	8%	2%	6%
P5	12%	11%	0%	12%	16%	0%	6%	7%	0%	6%	6%	0%	7%	9%	0%	6%	8%	0%
P6	0%	0%	0%	0%	0%	0%	0%	0%	0%	4%	12%	0%	0%	0%	0%	4%	9%	0%
P7	0%	0%	0%	0%	0%	0%	0%	0%	0%	10%	7%	0%	0%	0%	0%	9%	7%	0%
P8	0%	0%	0%	0%	0%	0%	0%	0%	0%	2%	3%	0%	0%	0%	0%	4%	1%	0%
P9	0%	2%	6%	0%	3%	7%	0%	1%	6%	0%	1%	6%	0%	2%	7%	0%	1%	7%
P10	0%	0%	0%	0%	0%	0%	0%	0%	0%	0%	0%	0%	0%	0%	0%	0%	0%	0%
P11	0%	0%	0%	0%	0%	0%	0%	0%	0%	0%	0%	0%	0%	0%	0%	0%	0%	0%
P12	0%	0%	0%	0%	0%	0%	0%	0%	0%	0%	0%	0%	0%	0%	0%	0%	0%	0%
P13	0%	0%	0%	0%	0%	0%	0%	0%	0%	0%	0%	0%	0%	0%	0%	0%	0%	0%
P14	0%	0%	0%	0%	0%	0%	0%	0%	0%	0%	0%	0%	0%	0%	0%	0%	0%	0%
P15	0%	0%	0%	0%	0%	0%	0%	0%	0%	0%	0%	0%	0%	0%	0%	0%	0%	0%
P16	0%	0%	0%	0%	0%	0%	0%	0%	0%	0%	0%	0%	0%	0%	0%	0%	0%	0%
P17	0%	0%	0%	0%	0%	0%	0%	0%	0%	0%	0%	0%	0%	0%	0%	0%	0%	0%
P18	0%	0%	0%	0%	0%	0%	0%	0%	0%	0%	0%	0%	0%	0%	0%	0%	0%	0%
P19	0%	0%	0%	0%	0%	0%	0%	0%	0%	0%	0%	0%	0%	0%	0%	0%	0%	0%
P20	0%	0%	0%	0%	0%	0%	0%	0%	0%	0%	0%	0%	0%	0%	0%	0%	0%	0%
P21	0%	0%	0%	0%	0%	0%	0%	0%	0%	0%	0%	0%	0%	0%	0%	0%	0%	0%
P22	0%	0%	0%	0%	0%	0%	0%	0%	0%	0%	0%	0%	0%	0%	0%	0%	0%	0%
P23	0%	0%	0%	0%	0%	0%	0%	0%	0%	0%	0%	0%	0%	0%	0%	0%	0%	0%
P24	0%	0%	0%	0%	0%	0%	0%	0%	0%	0%	0%	0%	0%	0%	0%	0%	0%	0%
F1	36%	40%	34%	39%	38%	45%	40%	35%	34%	30%	35%	34%	42%	48%	45%	25%	36%	45%
F2	37%	15%	0%	36%	12%	0%	20%	9%	0%	24%	1%	0%	21%	7%	0%	26%	6%	0%
F3	0%	17%	36%	0%	15%	42%	0%	10%	36%	0%	9%	36%	0%	9%	42%	0%	7%	42%
F4	0%	0%	0%	0%	0%	0%	0%	0%	0%	0%	0%	0%	0%	0%	0%	0%	0%	0%
F5	0%	0%	0%	0%	0%	0%	0%	0%	0%	0%	0%	0%	0%	0%	0%	0%	0%	0%
F6	0%	0%	0%	0%	0%	0%	0%	0%	0%	0%	0%	0%	0%	0%	0%	0%	0%	0%
C1	100%	100%	100%	100%	100%	0%	45%	19%	40%	43%	21%	45%	37%	35%	2%	38%	22%	39%
C2	0%	0%	0%	0%	0%	0%	50%	39%	6%	40%	23%	3%	36%	36%	50%	38%	39%	0%
C3	0%	0%	0%	0%	0%	0%	1%	18%	42%	1%	21%	48%	8%	1%	2%	13%	9%	45%
C4	0%	0%	0%	0%	0%	0%	0%	17%	6%	2%	9%	2%	7%	7%	45%	12%	22%	16%
C5	0%	0%	0%	0%	0%	0%	0%	2%	0%	5%	10%	1%	2%	1%	1%	0%	9%	0%
C6	0%	0%	0%	0%	0%	0%	4%	7%	5%	9%	16%	0%	9%	19%	0%	0%	0%	0%

3.6.2. Calculation of water intrusion for all eight octants

As mentioned earlier, the water propagation calculation in the FPHLM model has been performed for the eight 45˚ octants. The experimental tests were performed at only three wind angles of attack, including 0˚, 45˚ and 90˚. The first step for FPHLM implementation was to expand the results for all the desired wind directions. Because of the symmetrical model, it was possible to generate the results for 135˚ to 315˚ based on the results obtained from the 0˚, 45˚ and 90˚ tests. Finally, the experimental test results were presented by six Water Propagation Matrices (WPM) for two building roof types and three exteriors Damage States (Table 8 to Table 13). Each matrix is composed of thirty-six rows for thirty-six interior components, and eight columns for eight different wind directions. The values presented in these tables are the normalized share of different interior components. For the room components, including P1 to P24 and F1 to F6, the values are normalized to the total volume of water that enters through the wall openings. For Ceiling components (C1 to C6), the values are normalized to the total volume of water that intrudes through the roof openings.

Table 8. Water Propagation Matrix for Hip roof at DS0

Interior component	Hip-DS0-0°wind	Hip-DS0-45°wind	Hip-DS0-90°wind	Hip-DS0-135°wind	Hip-DS0-180°wind	Hip-DS0-225°wind	Hip-DS0-270°wind	Hip-DS0-315°wind
P1	15%	13%	0%	0%	0%	0%	0%	11%
P2	0%	0%	0%	0%	0%	0%	0%	0%
P3	0%	0%	0%	0%	0%	0%	0%	0%
P4	0%	1%	24%	2%	0%	0%	0%	0%
P5	12%	11%	0%	0%	0%	0%	0%	13%
P6	0%	0%	0%	0%	0%	2%	24%	1%
P7	0%	0%	0%	0%	0%	0%	0%	0%
P8	0%	0%	0%	0%	0%	0%	0%	0%
P9	0%	2%	6%	1%	0%	0%	0%	0%
P10	0%	0%	0%	0%	0%	0%	0%	0%
P11	0%	0%	0%	0%	0%	0%	0%	0%
P12	0%	0%	0%	13%	15%	11%	0%	0%
P13	0%	0%	0%	0%	0%	0%	0%	0%
P14	0%	0%	0%	0%	0%	0%	0%	0%
P15	0%	0%	0%	0%	0%	1%	6%	2%
P16	0%	0%	0%	11%	12%	13%	0%	0%
P17	0%	0%	0%	0%	0%	0%	0%	0%
P18	0%	0%	0%	0%	0%	0%	0%	0%
P19	0%	0%	0%	0%	0%	0%	0%	0%
P20	0%	0%	0%	0%	0%	0%	0%	0%
P21	0%	0%	0%	0%	0%	0%	0%	0%
P22	0%	0%	0%	0%	0%	0%	0%	0%
P23	0%	0%	0%	0%	0%	0%	0%	0%
P24	0%	0%	0%	0%	0%	0%	0%	0%
F1	36%	40%	34%	17%	0%	0%	0%	15%
F2	37%	15%	0%	0%	0%	17%	34%	40%
F3	0%	17%	36%	40%	36%	15%	0%	0%
F4	0%	0%	0%	15%	37%	40%	36%	17%
F5	0%	0%	0%	0%	0%	0%	0%	0%
F6	0%	0%	0%	0%	0%	0%	0%	0%
C1	100%	100%	100%	0%	0%	0%	0%	0%
C2	0%	0%	0%	0%	0%	0%	100%	100%
C3	0%	0%	0%	100%	100%	0%	0%	0%
C4	0%	0%	0%	0%	0%	100%	0%	0%
C5	0%	0%	0%	0%	0%	0%	0%	0%
C6	0%	0%	0%	0%	0%	0%	0%	0%

Table 9. Water Propagation Matrix for Hip roof at DS1

Interior component	Gable-DS0-0°wind	Gable-DS0-45°wind	Gable-DS0-90°wind	Gable-DS0-135°wind	Gable-DS0-180°wind	Gable-DS0-225°wind	Gable-DS0-270°wind	Gable-DS0-315°wind
P1	14%	15%	0%	0%	0%	0%	0%	16%
P2	0%	0%	0%	0%	0%	0%	0%	0%
P3	0%	0%	0%	0%	0%	0%	0%	0%
P4	0%	1%	6%	3%	0%	0%	0%	0%
P5	12%	16%	0%	0%	0%	0%	0%	15%
P6	0%	0%	0%	0%	0%	3%	6%	1%
P7	0%	0%	0%	0%	0%	0%	0%	0%
P8	0%	0%	0%	0%	0%	0%	0%	0%
P9	0%	3%	7%	1%	0%	0%	0%	0%
P10	0%	0%	0%	0%	0%	0%	0%	0%
P11	0%	0%	0%	0%	0%	0%	0%	0%
P12	0%	0%	0%	15%	14%	16%	0%	0%
P13	0%	0%	0%	0%	0%	0%	0%	0%
P14	0%	0%	0%	0%	0%	0%	0%	0%
P15	0%	0%	0%	0%	0%	1%	7%	3%
P16	0%	0%	0%	16%	12%	15%	0%	0%
P17	0%	0%	0%	0%	0%	0%	0%	0%
P18	0%	0%	0%	0%	0%	0%	0%	0%
P19	0%	0%	0%	0%	0%	0%	0%	0%
P20	0%	0%	0%	0%	0%	0%	0%	0%
P21	0%	0%	0%	0%	0%	0%	0%	0%
P22	0%	0%	0%	0%	0%	0%	0%	0%
P23	0%	0%	0%	0%	0%	0%	0%	0%
P24	0%	0%	0%	0%	0%	0%	0%	0%
F1	39%	38%	45%	15%	0%	0%	0%	12%
F2	36%	12%	0%	0%	0%	15%	45%	38%
F3	0%	15%	42%	38%	39%	12%	0%	0%
F4	0%	0%	0%	12%	36%	38%	42%	15%
F5	0%	0%	0%	0%	0%	0%	0%	0%
F6	0%	0%	0%	0%	0%	0%	0%	0%
C1	100%	100%	0%	0%	0%	0%	0%	0%
C2	0%	0%	0%	0%	0%	0%	0%	100%
C3	0%	0%	0%	100%	100%	0%	0%	0%
C4	0%	0%	0%	0%	0%	100%	0%	0%
C5	0%	0%	0%	0%	0%	0%	0%	0%
C6	0%	0%	0%	0%	0%	0%	0%	0%

Table 10. Water Propagation Matrix for Hip roof at DS2

Interior component	Hip-DS1-0°wind	Hip-DS1-45°wind	Hip-DS1-90°wind	Hip-DS1-135°wind	Hip-DS1-180°wind	Hip-DS1-225°wind	Hip-DS1-270°wind	Hip-DS1-315°wind
P1	7%	13%	0%	0%	0%	0%	0%	9%
P2	1%	17%	0%	0%	0%	0%	0%	4%
P3	14%	5%	0%	0%	0%	0%	0%	10%
P4	11%	1%	24%	2%	0%	0%	0%	17%
P5	6%	7%	0%	0%	0%	0%	0%	10%
P6	0%	0%	0%	0%	0%	1%	6%	1%
P7	0%	0%	0%	0%	0%	0%	0%	0%
P8	0%	0%	0%	0%	0%	0%	0%	0%
P9	0%	1%	6%	1%	0%	0%	0%	0%
P10	0%	0%	0%	0%	0%	0%	0%	0%
P11	0%	0%	0%	0%	0%	0%	0%	0%
P12	0%	0%	0%	10%	6%	7%	0%	0%
P13	0%	0%	0%	4%	1%	20%	0%	0%
P14	0%	0%	0%	10%	14%	2%	0%	0%
P15	0%	0%	0%	17%	11%	1%	24%	2%
P16	0%	0%	0%	9%	7%	8%	0%	0%
P17	0%	0%	0%	0%	0%	0%	0%	0%
P18	0%	0%	0%	0%	0%	0%	0%	0%
P19	0%	0%	0%	0%	0%	0%	0%	0%
P20	0%	0%	0%	0%	0%	0%	0%	0%
P21	0%	0%	0%	0%	0%	0%	0%	0%
P22	0%	0%	0%	0%	0%	0%	0%	0%
P23	0%	0%	0%	0%	0%	0%	0%	0%
P24	0%	0%	0%	0%	0%	0%	0%	0%
F1	40%	35%	34%	13%	0%	0%	0%	2%
F2	20%	9%	0%	0%	0%	10%	36%	32%
F3	0%	10%	36%	32%	20%	9%	0%	0%
F4	0%	0%	0%	2%	40%	41%	34%	13%
F5	0%	0%	0%	0%	0%	0%	0%	0%
F6	0%	0%	0%	0%	0%	0%	0%	0%
C1	45%	19%	40%	18%	0%	17%	6%	39%
C2	50%	39%	6%	17%	1%	18%	42%	19%
C3	1%	18%	42%	19%	50%	39%	6%	17%
C4	0%	17%	6%	39%	45%	19%	40%	18%
C5	0%	2%	0%	7%	4%	7%	5%	2%
C6	4%	7%	5%	2%	0%	2%	0%	7%

Table 11. Water Propagation Matrix for Gable roof at DS0

Interior component	Hip-DS2-0°wind	Hip-DS2-45°wind	Hip-DS2-90°wind	Hip-DS2-135°wind	Hip-DS2-180°wind	Hip-DS2-225°wind	Hip-DS2-270°wind	Hip-DS2-315°wind
P1	7%	7%	0%	0%	0%	0%	0%	6%
P2	0%	17%	0%	0%	0%	0%	0%	3%
P3	8%	2%	0%	0%	0%	0%	0%	7%
P4	7%	1%	24%	1%	0%	0%	0%	12%
P5	6%	6%	0%	0%	0%	0%	0%	7%
P6	4%	12%	0%	0%	0%	1%	24%	1%
P7	10%	7%	0%	0%	0%	0%	0%	2%
P8	2%	3%	0%	0%	0%	0%	0%	17%
P9	0%	1%	6%	1%	7%	12%	0%	0%
P10	0%	0%	0%	2%	8%	7%	0%	0%
P11	0%	0%	0%	17%	0%	3%	0%	0%
P12	0%	0%	0%	7%	7%	6%	0%	0%
P13	0%	0%	0%	3%	2%	17%	0%	0%
P14	0%	0%	0%	7%	10%	2%	0%	0%
P15	0%	0%	0%	12%	4%	1%	6%	1%
P16	0%	0%	0%	6%	6%	7%	0%	0%
P17	0%	0%	0%	0%	0%	0%	0%	0%
P18	0%	0%	0%	0%	0%	0%	0%	0%
P19	0%	0%	0%	0%	0%	0%	0%	0%
P20	0%	0%	0%	0%	0%	0%	0%	0%
P21	0%	0%	0%	0%	0%	0%	0%	0%
P22	0%	0%	0%	0%	0%	0%	0%	0%
P23	0%	0%	0%	0%	0%	0%	0%	0%
P24	0%	0%	0%	0%	0%	0%	0%	0%
F1	30%	35%	34%	9%	0%	0%	0%	1%
F2	24%	1%	0%	0%	0%	9%	34%	35%
F3	0%	9%	36%	35%	30%	1%	0%	0%
F4	0%	0%	0%	1%	24%	35%	36%	9%
F5	0%	0%	0%	0%	0%	0%	0%	0%
F6	0%	0%	0%	0%	0%	0%	0%	0%
C1	43%	21%	45%	21%	1%	9%	3%	23%
C2	40%	23%	3%	9%	2%	21%	45%	21%
C3	1%	21%	48%	21%	43%	23%	2%	9%
C4	2%	9%	2%	23%	40%`	21%	48%	21%
C5	5%	10%	1%	16%	9%	16%	1%	10%
C6	9%	16%	0%	10%	5%	10%	0%	16%

Table 12. Water Propagation Matrix for Gable roof at DS1

Interior component	Gable-DS1-0°wind	Gable-DS1-45°wind	Gable-DS1-90°wind	Gable-DS1-135°wind	Gable-DS1-180°wind	Gable-DS1-225°wind	Gable-DS1-270°wind	Gable-DS1-315°wind
P1	8%	5%	0%	0%	0%	0%	0%	12%
P2	0%	16%	0%	0%	0%	0%	0%	2%
P3	12%	2%	0%	0%	0%	0%	0%	10%
P4	11%	1%	6%	2%	0%	0%	0%	14%
P5	7%	9%	0%	0%	0%	0%	0%	11%
P6	0%	0%	0%	0%	0%	2%	7%	1%
P7	0%	0%	0%	0%	0%	0%	0%	0%
P8	0%	0%	0%	0%	0%	0%	0%	0%
P9	0%	2%	7%	1%	0%	0%	0%	0%
P10	0%	0%	0%	0%	0%	0%	0%	0%
P11	0%	0%	0%	0%	0%	0%	0%	0%
P12	0%	0%	0%	11%	7%	9%	0%	0%
P13	0%	0%	0%	2%	0%	16%	0%	0%
P14	0%	0%	0%	10%	12%	4%	0%	0%
P15	0%	0%	0%	14%	11%	2%	6%	2%
P16	0%	0%	0%	12%	8%	7%	0%	0%
P17	0%	0%	0%	0%	0%	0%	0%	0%
P18	0%	0%	0%	0%	0%	0%	0%	0%
P19	0%	0%	0%	0%	0%	0%	0%	0%
P20	0%	0%	0%	0%	0%	0%	0%	0%
P21	0%	0%	0%	0%	0%	0%	0%	0%
P22	0%	0%	0%	0%	0%	0%	0%	0%
P23	0%	0%	0%	0%	0%	0%	0%	0%
P24	0%	0%	0%	0%	0%	0%	0%	0%
F1	42%	48%	45%	11%	0%	0%	0%	8%
F2	21%	7%	0%	0%	0%	9%	42%	28%
F3	0%	9%	42%	28%	21%	7%	0%	0%
F4	0%	0%	0%	8%	42%	43%	45%	11%
F5	0%	0%	0%	0%	0%	0%	0%	0%
F6	0%	0%	0%	0%	0%	0%	0%	0%
C1	37%	35%	2%	1%	7%	7%	45%	36%
C2	36%	36%	50%	7%	8%	1%	2%	35%
C3	8%	1%	2%	35%	36%	36%	50%	7%
C4	7%	7%	45%	36%	37%	35%	2%	1%
C5	2%	1%	1%	19%	9%	19%	0%	1%
C6	9%	19%	0%	1%	2%	1%	1%	19%

Table 13. Water Propagation Matrix for Gable roof at DS2

Interior component	Gable-DS2-0°wind	Gable-DS2-45°wind	Gable-DS2-90°wind	Gable-DS2-135°wind	Gable-DS2-180°wind	Gable-DS2-225°wind	Gable-DS2-270°wind	Gable-DS2-315°wind
P1	9%	6%	0%	0%	0%	0%	0%	8%
P2	3%	14%	0%	0%	0%	0%	0%	1%
P3	6%	4%	0%	0%	0%	0%	0%	7%
P4	8%	2%	6%	1%	0%	0%	0%	9%
P5	6%	8%	0%	0%	0%	0%	0%	6%
P6	4%	9%	0%	0%	0%	1%	6%	2%
P7	9%	7%	0%	0%	0%	0%	0%	4%
P8	4%	1%	0%	0%	0%	0%	0%	14%
P9	0%	1%	7%	2%	8%	9%	0%	0%
P10	0%	0%	0%	4%	6%	7%	0%	0%
P11	0%	0%	0%	14%	3%	1%	0%	0%
P12	0%	0%	0%	6%	9%	8%	0%	0%
P13	0%	0%	0%	1%	4%	14%	0%	0%
P14	0%	0%	0%	7%	9%	4%	0%	0%
P15	0%	0%	0%	9%	4%	2%	7%	1%
P16	0%	0%	0%	8%	6%	6%	0%	0%
P17	0%	0%	0%	0%	0%	0%	0%	0%
P18	0%	0%	0%	0%	0%	0%	0%	0%
P19	0%	0%	0%	0%	0%	0%	0%	0%
P20	0%	0%	0%	0%	0%	0%	0%	0%
P21	0%	0%	0%	0%	0%	0%	0%	0%
P22	0%	0%	0%	0%	0%	0%	0%	0%
P23	0%	0%	0%	0%	0%	0%	0%	0%
P24	0%	0%	0%	0%	0%	0%	0%	0%
F1	25%	36%	45%	7%	0%	0%	0%	6%
F2	26%	6%	0%	0%	0%	7%	45%	36%
F3	0%	7%	42%	36%	25%	6%	0%	0%
F4	0%	0%	0%	6%	26%	36%	42%	7%
F5	0%	0%	0%	0%	0%	0%	0%	0%
F6	0%	0%	0%	0%	0%	0%	0%	0%
C1	38%	22%	39%	9%	13%	22%	0%	39%
C2	38%	39%	0%	22%	12%	9%	39%	22%
C3	13%	9%	45%	22%	38%	39%	16%	22%
C4	12%	22%	16%	39%	38%	22%	45%	9%
C5	0%	9%	0%	0%	0%	0%	0%	9%
C6	0%	0%	0%	9%	0%	9%	0%	0%

To implement these matrices into the FPHLM requires a more detailed explanation of how the FPHLM model works. The following paragraphs describe the

methodology applied in the FPHLM model to evaluate the amount of water intrusion into the building interior.

In the applied methodology, it is assumed that for a given hurricane simulation, the building is subjected to a specific amount of vertical rain. The model calculates the amount of rain based on the synthetic hurricane data, which relate the total horizontal rain and the peak wind gust speed. More information on the procedure can be found in Johnson et al., 2018. A portion of this vertical rain that reaches the building before the occurrence of V_{max} is named WDR_1, while the rest of it, which reaches the building after the V_{max} happens, is referred to as WDR_2.

The total amount of WDR_1 can be distributed among four time intervals covering the hurricane duration form the start to the time when V_{max} happens (Johnson, 2015). The amount of vertical rain during each time interval is a portion of WDR_1, and the summation of vertical rain for all four time intervals equals WDR_1. Therefore, the amount of vertical rain for the m^{th} time interval (WDR_m) can be calculated by:

$$WDR_m = \alpha_m . WDR_1 \qquad \text{EQ. 3}$$

where α_m is the fraction of WDR_1 that happens at the m^{th} time interval. On the other hand, it is assumed that the wind flow rotates over four wind directions from the start of the hurricane to the time when V_{max} happens. Each of these wind directions corresponds to a specific time interval (θ_m). Because of the agreement between the time interval and wind direction, WDR_m is referred to by $WDR_{\theta m}$.

Similarly, the amount of WDR_2 is distributed among five time intervals, starting from the time when V_{max} happens to the end of the hurricane. The amount of vertical rain for the n^{th} time interval (WDR_n) can be calculated by:

$$WDR_n = \beta_n . WDR_2 \qquad \text{EQ. 4}$$

In this equation, β_n is the fraction of WDR_2 that happens at n^{th} time interval. Likewise, the wind direction for the n^{th} time interval is named θ_n, and WDR_n is referred to as $WDR_{\theta n}$.

Once the amount of vertical rain is determined, the next step is to estimate how much of the rain can get inside the building. The vertical rain can get into the building interior through either surface runoff or direct impinging. The direct impinging water is the amount of rain that directly impinges on the building envelope openings. The surface runoff water is the amount of water that runs over the building envelope and gets into the building interior by penetrating through the exterior openings. To calculate the amount of water intrusion through the surface runoff and direct impinging, EQ. 5 and EQ. 6 are derived from the relationships suggested by Baheru, 2014. For a given wind direction, knowing the amount of vertical rain (WDR_θ), the amount of surface runoff water intrusion (V_{SR_θ}) through an envelope opening with the exposed surface area of A_{SR_θ} to that wind direction, can be calculated by:

$$V_{SR\_\theta} = SRC_\theta . WDR_\theta . A_{SR\_\theta} \qquad \text{EQ. 5}$$

To calculate the amount of water intrusion through the direct impinging at an opening with the exposed area of A_{o_θ} to the wind direction (θ), EQ. 6 can be derived from (Baheru, 2014) as follows:

$$V_{DI\_\theta} = RAF_{\theta}.WDR_{\theta}.A_{o\_\theta} \qquad EQ.\ 6$$

In the above equations, SRC_{θ} and RAF_{θ} are the Surface Runoff Coefficient and Rain Admittance Factor for the wind angle direction of θ, respectively, suggested by Baheru (Baheru, 2014). Also, more information on the calculation of A_{SR_θ} and A_{o_θ} can be found in this reference.

To calculate the total amount of water intrusion, the water intrusion at different wind angles should be calculated and added as the hurricane rotates around the building. Considering the fact that the amount of vertical rain affecting the building and the area of envelope opening depends on the occurrence of V_{max}, two different sets of formulas have been developed for the calculation of water intrusion before and after the occurrence of V_{max}. On the other hand, since the total amount of water intrusion at each wind direction is composed of direct impinging rain and surface runoff water intrusion, each set of formula consists of two relations: one for calculating the amount of surface runoff water and another one for direct impinging water.

To calculate the amount of water intrusion before the occurrence of V_{max}, through surface runoff and direct impinging, EQ. 7 and EQ. 8 can be used, respectively.

$$V_{SR\_\theta m} = SRC_{\theta m}.\alpha_m.WDR_1.A_{SR\_d\_\theta m} \qquad EQ.\ 7$$

$$V_{DI\_\theta m} = RAF_{\theta m}.\alpha_m.WDR_1.A_{o\_d\_\theta m} \qquad EQ.\ 8$$

These relations were derived from EQ. 5 and EQ. 6 by substituting θ for θ_m, which represents the wind angle before the occurrence of V_{max}, so WDR_{θ} has been replaced by $WDR_{\theta m}$, which equals $\alpha_m.WDR_1$ based on EQ. 3. Additionally, A_{SR_θ} and A_{o_θ} were replaced by $A_{SR\_d\_\theta m}$ and $A_{o\_d\_\theta m}$, which represent the exposed area of

defects to surface runoff and direct impinging water intrusion, respectively. Because before the occurrence of V_{max}, water can intrude only through the pre-existing defects, the area of defects was used in the above equations.

Similarly, the amount of water intrusion for the wind directions that occur after V_{max} can be calculated by EQ. 9 and EQ. 10 for the surface runoff and direct impinging, respectively.

$$V_{SR\_\theta n} = SRC_{\theta n}.\beta_n.WDR_2.A_{SR\_b\_\theta n} \qquad EQ.\ 9$$

$$V_{DI\_\theta n} = RAF_{\theta n}.\beta_n.WDR_2.A_{o\_b\_\theta n} \qquad EQ.\ 10$$

The above equations were derived by replacing θ with θ_n in EQ. 5 and EQ. 6. Similarly, WDR_θ has been replaced by $WDR_{\theta n}$, which equals $\alpha_n.WDR_2$ based on EQ. 4. In this case, because the occurrence of V_{max} results in wind-induced openings on the building exterior, A_{SR_θ} and A_{o_θ} were replaced by $A_{SR\_b\_\theta n}$ and $A_{o\_b\_\theta n}$, which represent the exposed area of wind-induced breaches to surface runoff and direct impinging water intrusion, respectively.

The next step would be to calculate the amount of water that reaches each interior component once the water intrudes through either direct impinging or surface runoff. This can be accomplished by using the WPM matrices. As explained previously, the WPM matrices were developed for different exterior damage states depending on the severity of the wind-induced damages. Therefore, to distribute the water among the interior components using the WPMs, the damage state of the building at the time of water intrusion should be decided on. It was explained that the water intrusion is

calculated at two phases, including before the occurrence of V_{max} and after V_{max} happens. At each of these two phases, the damage state of the building should be determined.

Since the DS0 model was initially designed to simulate the light damage and it only includes the pre-existing defects and damages caused by low wind speeds, the WPMs obtained for the DS0 can be used for calculating the water propagation among the interior components before the V_{max} phase, regardless of the value of maximum wind speed. However, after the occurrence of V_{max}, the exterior damage of the building depends on the value of the maximum wind speed, as well as the building construction type. Table 14 shows the wind speed associated with the different damage states for different construction types. Having the data presented in this table, the procedure displayed in Figure 42 can be used to decide on the damage state of the building after the occurrence of V_{max}, based on the value of V_{max} and the building construction type. From now on, the applied WPM before and after the occurrence of V_{max} are referred to as WPM_DS0 and WPM_DS, respectively. It should be noted that WPM_DS can be the WPM for either DS0, DS1 or DS2, depending on the maximum wind speed and construction type.

Table 14. Wind speed associated with different damage state for different construction types

Damage State	DAMAGE	Construction Type		
		W00 (weak)	M00 (Moderate)	S00 (strung)
Light (DS0)	up to 6%	up to 85	up to 100	up to 125
Minor (DS1)	10%	100	115	145
Moderate (DS2)	20%	120	130	165

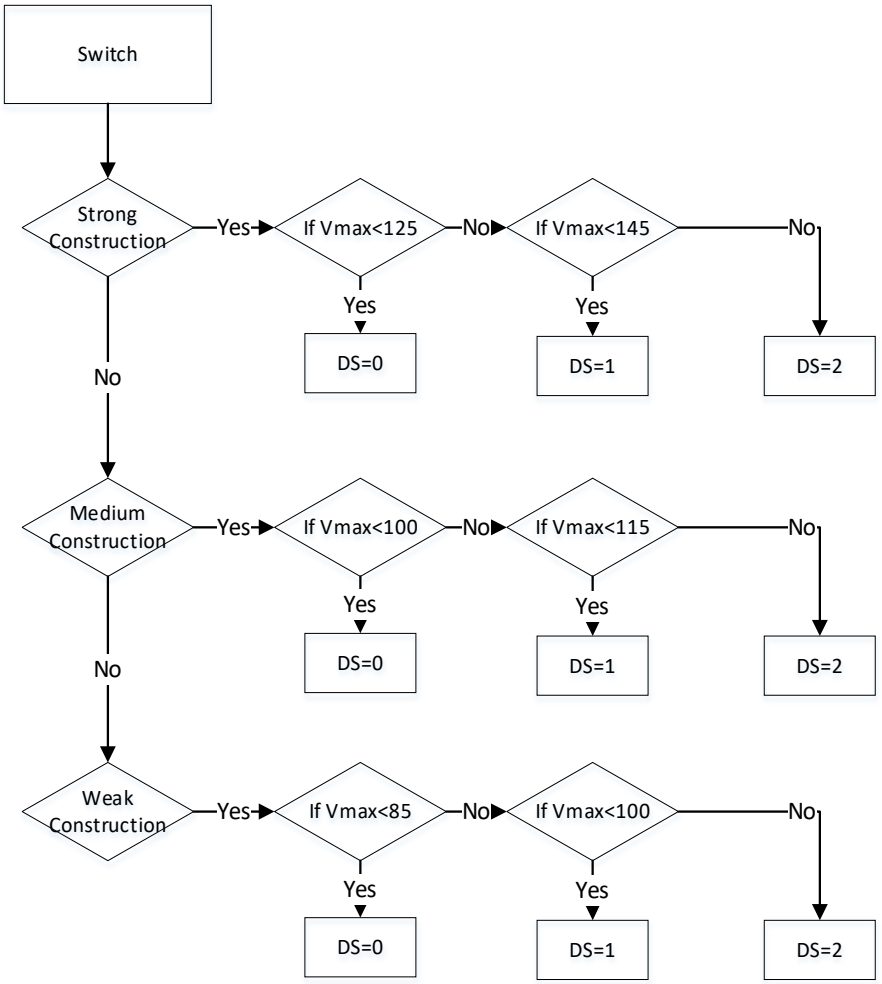

Figure 42. Procedure for determining the damage state of the building when V_{max} is exceeded

As mentioned earlier in this chapter, the WPM matrices were normalized so that for each wind direction the amount of water reaching the room compartments, including P1 to P24 and F1 to F6, can be calculated by multiplying the associated cell of the matrix for the desired component (row) and wind direction (column) to the volume of water that enters through the wall openings. Thus, EQ. 7 and EQ. 8 can be modified to EQ. 11 and EQ. 12, respectively, to calculate the amount of water that reaches each interior room component before the occurrence of V_{max}.

$$C_{i,SR\_\theta m} = SRC_{\theta m}.\alpha_m.WDR_1.A_{SR\_dWall\_\theta m}.WPM\_DS0(i,\theta_m)\ ,\ 1 \le i \le 30 \quad \textit{EQ. 11}$$

$$C_{i,DI\_\theta m} = RAF_{\theta m}.\alpha_m.WDR_1.A_{o\_dWall\_\theta m}.WPM\_DS0(i,\theta_m)\ ,\ 1 \le i \le 30 \quad \textit{EQ. 12}$$

The amount of water that reaches component C_i at the wind angle of θ_m from surface runoff and direct impinging through wall openings is displayed by $C_{i,SR\_\theta m}$ and $C_{i,DI\_\theta m}$, respectively. Since the above equations have been developed for the room components, the value of i can change from 1 to 30 (1 to 24 for partitions and 25 to 30 for flooring components). In the above equations $A_{SR\_dWall\_\theta m}$ and $A_{o\_dWall\_\theta m}$ that represent the exposed area of wall defects to surface runoff and direct impinging, respectively, replaced $A_{SR\_b\_\theta n}$ and $A_{o\_d\_\theta m}$ in EQ. 7 and EQ. 8, because for the room components, only the water that comes from the wall openings is of interest. As discussed previously, WPM_DS0 is the WPM obtained for the DS0 model.

Also, EQ. 9 and EQ. 10 can be modified to EQ. 13 and EQ. 14, respectively, to calculate the amount of water that reaches each interior room component after the occurrence of V_{max}.

$$C_{i,SR\_\theta n} = SRC_{\theta n}.\beta_n.WDR_2.A_{SR\_bWall\_\theta n}.WPM\_DS(i,\theta_n)\ ,\ 1 \le i \le 30 \quad \textit{EQ. 13}$$

$$C_{i,DI\_\theta n} = RAF_{\theta n}.\beta_n.WDR_2.A_{o\_bWall\_\theta n}.WPM\_DS(i,\theta_n)\ ,\ 1 \le i \le 30 \quad \textit{EQ. 14}$$

$C_{i,SR\_\theta n}$ and $C_{i,DI\_\theta n}$ represent the amount of water that reaches room component C_i at the wind angle of θ_n from surface runoff and direct impinging, respectively. The index i can change in the range of 1 to 30 for the room components. In these equations, $A_{SR\_bWall\_\theta m}$ and $A_{o\_bWall\_\theta m}$ represent the exposed area of wall breaches to surface

runoff and direct impinging, respectively, and substitute $A_{SR\_b\_\theta n}$ and $A_{o\_d\_\theta m}$ in EQ. 9 and EQ. 10. This substitution was done since only the water that comes from the wall openings is of interest for the room compartments. WPM_DS is the WPM after the occurrence of V_{max}, which can be obtained from the procedure of Figure 42.

Similarly, the amount of water that reaches the ceiling components, including C1 to C6, can be calculated by multiplying the pertinent cell of the WPM matrix for the desired ceiling component (row) and wind direction (column) to the amount of water that enters through the roof openings. Using the same approach for the ceiling components, equations EQ. 15 and EQ. 16 were developed for the distribution of the intruded water through surface runoff and direct impinging before the occurrence of V_{max}.

$$C_{i,SR\_\theta m} = SRC_{\theta m}.\alpha_m.WDR_1.A_{SR\_dRoof\_\theta m}.WPM\_DS0(i,\theta_m),\ 31 \le i \le 36 \quad EQ.\ 15$$

$$C_{i,DI\_\theta m} = RAF_{\theta m}.\alpha_m.WDR_1.A_{o\_dRoof\_\theta m}.WPM\_DS0(i,\theta_m),\ 31 \le i \le 36 \quad EQ.\ 16$$

In these equations, $C_{i,SR\_\theta m}$ and $C_{i,DI\_\theta m}$ are the shares of ceiling component C_i from surface runoff and direct impinging, respectively. The index i is changing from 31 to 36 to represent the ceiling components. Since only the water intrusion through the roof opening can affect these components, the roof defects area exposed to surface runoff ($A_{SR\_dRoof\_\theta m}$) and direct impinging ($A_{o\_dRoof\_\theta m}$) were used in equations EQ. 15 and EQ. 16, respectively. In the above equations, WPM_DS0 is the WPM before the occurrence of V_{max}, which was obtained from the large-scale experimental tests of the building model at DS0.

Similarly, EQ. 17 and EQ. 18 were developed for the water distribution among the ceiling components after V_{max} occurs.

$$C_{i,SR\_\theta n} = SRC_{\theta n}.\beta_n.WDR_2.A_{SR\_bRoof\_\theta n}.WPM\_DS(i,\theta_n)\ ,\ 31 \le i \le 36 \qquad \textit{EQ. 17}$$

$$C_{i,DI\_\theta n} = RAF_{\theta n}.\beta_n.WDR_2.A_{o\_bRoof\_\theta n}.WPM\_DS(i,\theta_n)\ ,\ 31 \le i \le 36 \qquad \textit{EQ. 18}$$

In these equations, $C_{i,SR\_\theta n}$ and $C_{i,DI\_\theta n}$ are the shares of ceiling component C_i from surface runoff and direct impinging, when i is in the rage of 31 to 36. Also, $A_{SR\_bRoof\_\theta n}$ and $A_{o\_bRoof\_\theta n}$ represent the exposed area of roof breaches to surface runoff and direct impinging, respectively. WPM_DS is the WPM after the occurrence of V_{max}, obtained from the procedure of Figure 42.

Finally, equations EQ. 15 to EQ. 18 can be directly implemented in the FPHLM program for the calculation of water distribution among the interior components.

To summarize, the water propagation matrices were developed, and modifications were proposed to the FPHLM program to use the experimental results. These modifications allow the FPHLM to calculate the percentage of water that reaches each group of interior components (e.g. flooring, the partition, and ceiling). Using this information, the program can calculate the sustained physical damage based on the volume of water that reaches each group of interior components.

CHAPTER 4

FULL-SCALE EXPERIMENTS ON MOISTURE-INDUCED DAMAGES

CHAPTER 4. INVESTIGATION OF MOISTURE-INDUCED DAMAGES

4.1. Introduction

The second phase of the experimental study focused on the evaluation of the interior damage caused by water intrusion into the building. The results of these experimental tests provided a means to understand the damage of interior components when subjected to a progressive volume of water intrusion.

4.2. Test setup

The tests were performed at the WOW EF. Figure 43 shows the wind speed profile at the center of the test section. The rain rate at the mean roof height of the full-scale building is presented in Figure 44.

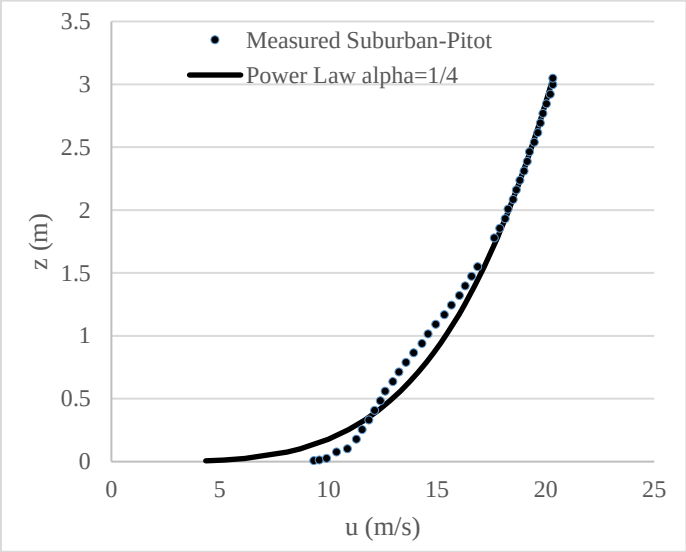

Figure 43. Wind speed profile

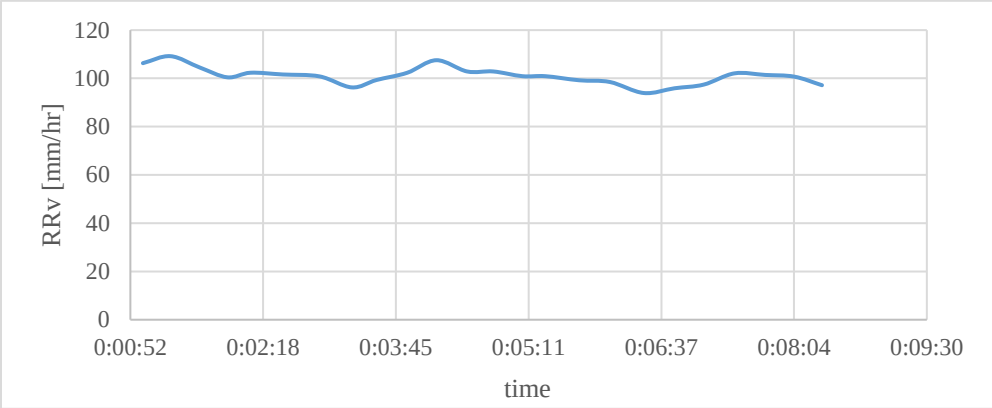

Figure 44. Vertical Rain Rate (RR_v) at mean roof height

4.3. Model Preparation

Since the sustained damage by the interior components is directly affected by the material properties of the components, it was decided to use the same materials as commonly used in residential building construction. On the other hand, since the scaling effects on the material properties can bias the damage estimation in scaled-down models, it was decided to test a full-scale model. Figure 45 shows the full-scale gable roof building model used for the experimental tests. The wood-frame building model allowed for the installation of drywalls directly on the studs (Figure 46).

Figure 45. Full-scale model

Figure 46. Wall with wood studs

The building interior was prepared by installing 1/2” drywall and applying one layer of primer and paint on the surface (Figure 47). The ceiling was covered with horizontally installed plywood to resemble the internal volume of typical residential buildings.

Figure 47. Interior of the building model

The sustained damage by the interior side of the walls depends on the increase in moisture content of the drywall, so the experimental tests were designed to measure the increase in moisture content of the drywall due to consecutive water intrusion tests. Several locations on each of the interior wall surfaces were marked for moisture measurement, as displayed in Figure 48. At the end of each test, the Delmhorst DB-2100 moisture meter was used to measure the moisture content of the drywall at the marked locations.

East Wall

West wall

North Wall

South Wall

Figure 48. Marked locations for moisture measurements

To obtain the volume of water reaching the interior side of the walls and leading to moisture increase in the drywall, the sloped gutters were installed below the drywall. Each gutter was connected to a bucket and conveyed the runoff water from the wall where it was installed to that bucket. At the end of each test, the buckets were weighed to obtain the amount of water reaching each wall and resulting from the moisture increase in the drywall. The results of these tests indicated a relationship between the volume of water reaching the interior wall surface and moisture increase on the drywall installed in the wall.

4.4. Test plan

The tests were designed to evaluate the extent of damage at interior sides of the wall due to water intrusion through the window opening. The model was prepared to be tested at the minor damage state (i.e. DS1 corresponds to only one open window at the east wall) and the moderate damage state (i.e. DS2 corresponds to two open windows, one at the east wall and another at the south wall). The DS1 case was tested at two wind angles of 0º and 45º, while DS2 was tested only at the 0º wind direction (Figure 49).

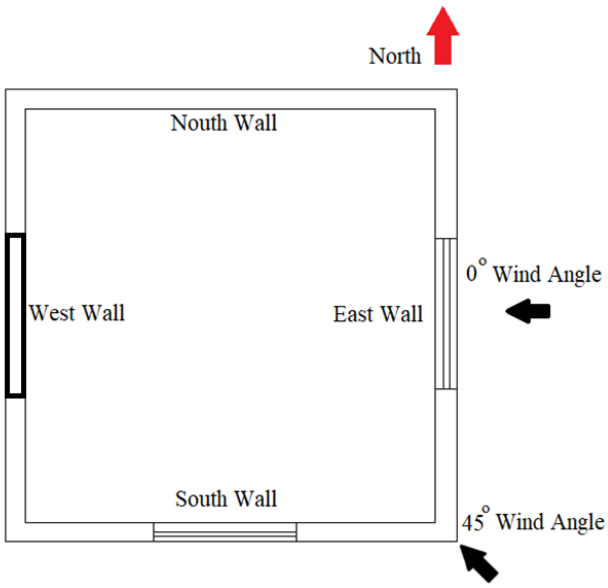

Figure 49. Wind direction notation

4.5. Test results and discussion

This section presents the results of moisture measurement at the full-scale experimental model. During the tests, the model was subjected to consecutive periods of water intrusion. After each period of water exposure, the moisture content at the drywall was measured using a handheld moisture meter, and the results were recorded. Additionally, the runoff water on the surface of each interior wall during the period of

water exposure was conveyed and accumulated in a separate bucket. The total volume of water that reaches a wall could be calculated by adding the volume of water that runs off its surface and the volume of water that is absorbed by its drywall. Finally, at the end of each run of the tests, the moisture measurement at each wall could be related to the volume of water reaching the surface of that wall.

4.5.1. Moisture content of the drywall for DS1 model at 0˚ wind direction

For the DS1 model, at the 0˚ wind direction, the tests were performed during two consecutive days. During the first day, the tests were performed at four time intervals, including two consecutive 5-minute tests followed by two consecutive 10-minute exposures to rain. Among these seven test periods, only the first set of tests started with the dry interior condition. For the rest of the tests, there was not enough time to allow the building interior to dry. At the end of each duration of water exposure, the total volume of water reaching the interior wall surface was calculated as the sum of the accumulated water on the bucket since the start of the first set of the tests and the volume of water that was absorbed by the drywall at the end of that exposure period. To calculate the amount of absorbed water by the drywall, the difference between the moisture content after the test and the moisture content before the start of the first set of tests (dry condition) was calculated at different measurement locations and multiplied by the tributary weight associated with any location. Then, the total absorbed water was calculated as the sum of the absorbed water at all the measurement locations.

The second-day tests were performed for three consecutive time intervals, including 10-min, 15-min, and 30-min of rain exposure. Unlike the first-day tests, the,

second-day tests started with the wet drywall condition, since there was not enough time to allow for complete drying of the building interior. On the other hand, the moisture content of the drywall at the beginning of the second day was less than the moisture content at the end of the first day, meaning that some of the absorbed water since the last test of the first day had left the drywall. Therefore, modifications were applied to calculate the required amount of water resulting in the moisture content at the beginning of the second day.

In order to calculate the total volume of water that has reached each interior wall surface before the start of the second-day tests, a linear relation was developed between the volume of water reaching the wall surface and the amount of absorbed water by the drywall. Using this relation, the volume of water that has reached the wall surface at the beginning of the second day could be calculated given the amount of absorbed water just before the second-day testing occurred.

Figure 50 shows the experimental results for the different interior walls obtained from the first day of testing on the DS0 model subjected to the 0˚ wind direction, along with the obtained linear relations between the volume of water reaching the wall surface and the absorbed water by the drywall. Using these relations, the volume of water at the beginning of the second day was calculated based on the volume of the absorbed water at the start of the second day.

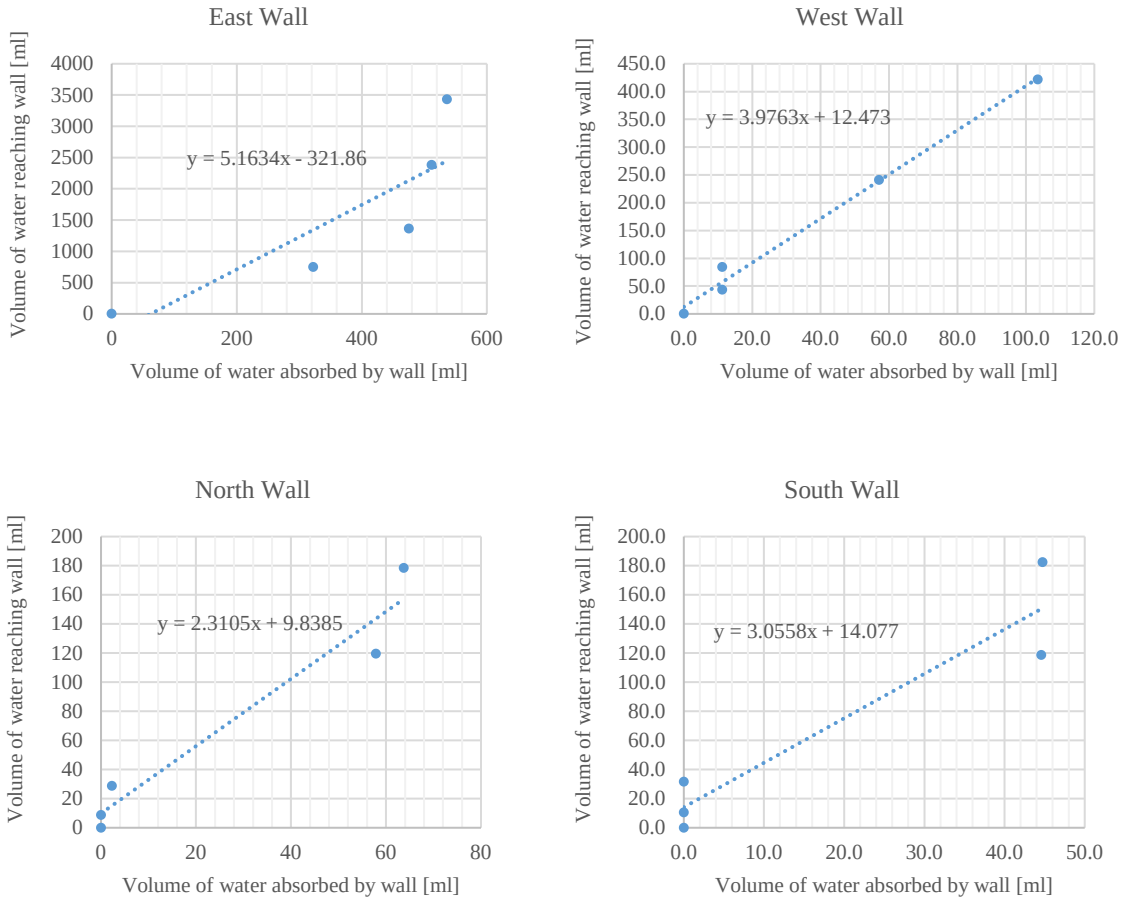

Figure 50. The experimental relation between the volume of water reaching the wall and absorbed water by the drywall for the first day of testing DS0 at the 0° wind direction

For the tests performed on the second day, the total volume of water reaching the wall surface was calculated as the sum of the accumulated water on the bucket since the start of the second day, and the amount of absorbed water by the drywall at the end of the test plus the volume of water calculated at the beginning of the second day obtained from the linear regression. Figure 51 shows the final results of all test durations performed on the DS0 model at the 0˚ wind angle.

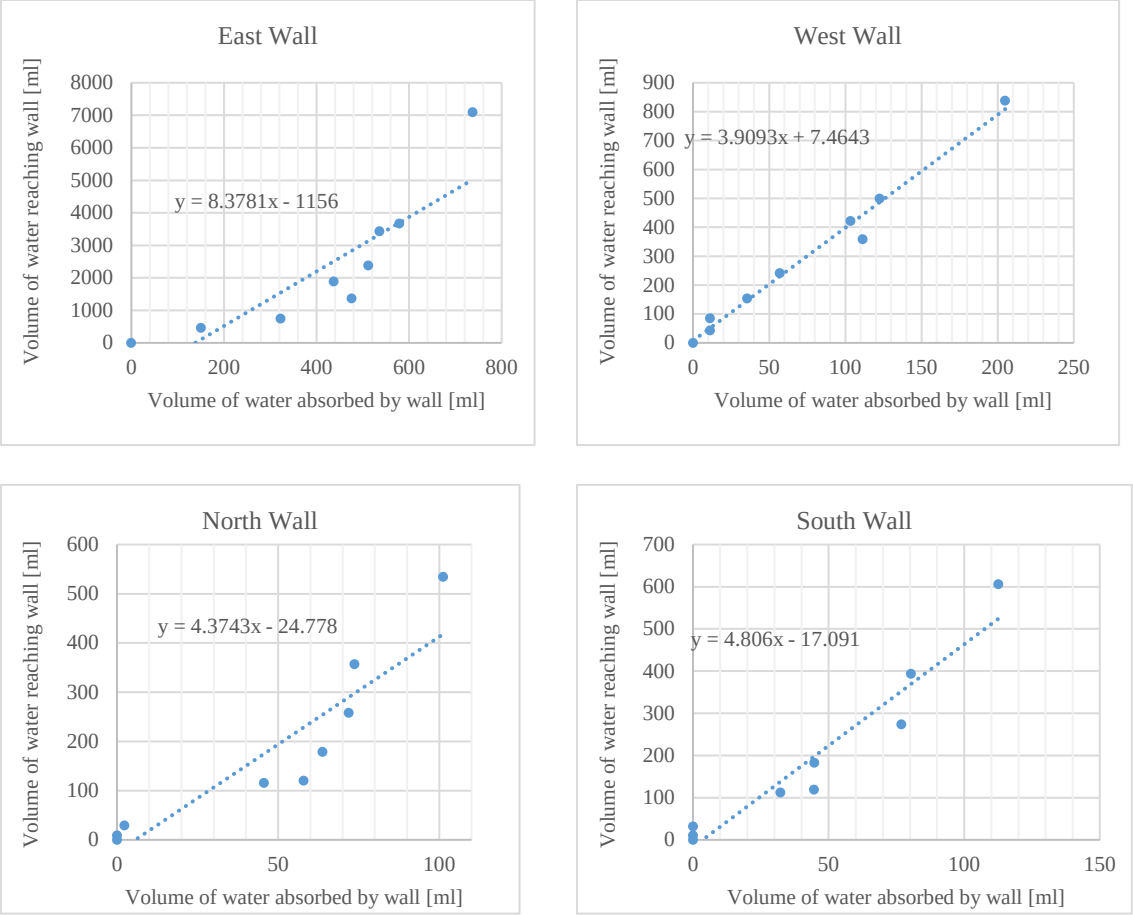

Figure 51. The experimental relation between the volume of water reaching the wall and absorbed water by the drywall for DS0 at the 0° wind direction

4.5.1.1 East wall DS1 at 0˚ wind direction

Figure 52 shows the moisture content of the East Wall affected by different volumes of water reaching its surface. As shown in Figure 49, the East Wall is the wall with the windward open window. It can be observed that the moisture content of the drywall increases by increasing the volume of water reaching the wall. Figure 52-a shows the dry condition before the start of the tests. It can be noted that the moisture at the drywall below the window immediately increases after the first period of rain exposure

(Figure 52-b). Thus, it can be claimed that even a relatively small (i.e. 0.75 liters) amount of water would be enough to damage this area. Then, continuing the tests results in the expansion of the wet area below the window toward the bottom of the wall (Figure 52-c). After that, the moisture trace moves from the center toward the sides of the wall (Figure 52-d, e and f). Another notable observation is that once the volume of water reaches a certain value (in this case 2.38 liters), the moisture content of the top portion of the wall begins to increase. This increase of moisture results from the increase in relative humidity of the indoor environment and not because of direct absorption of the rain by the drywall.

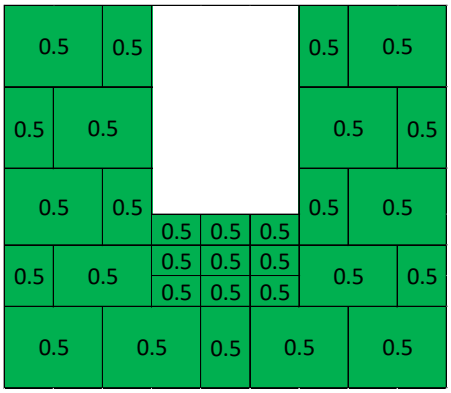

(a) volume of water = 0.00 liter

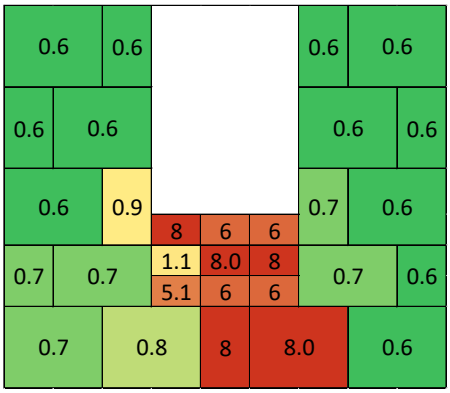

(d) volume of water = 2.38 liter

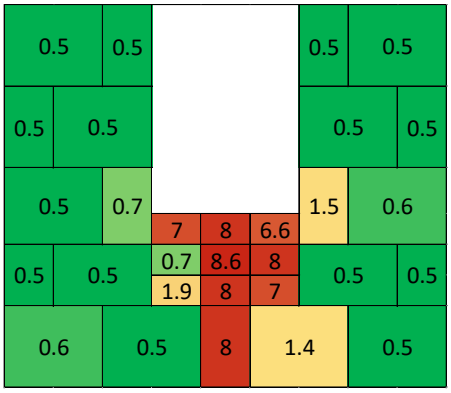

(b) volume of water = 0.75 liter

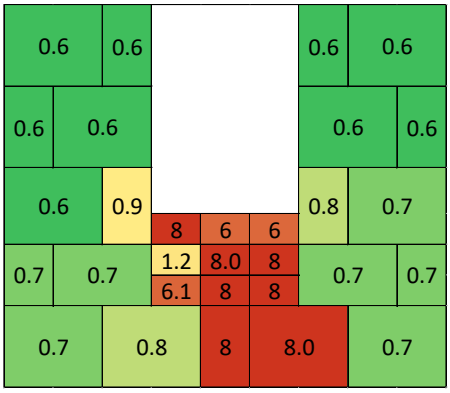

(e) volume of water = 3.43 liter

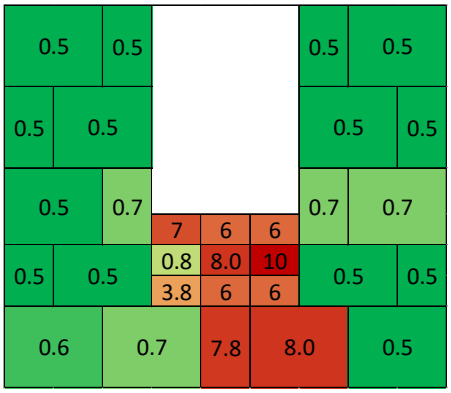

(c) volume of water = 1.36 liter

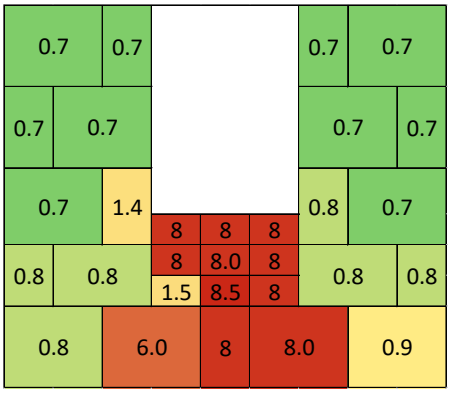

(f) volume of water = 7.09 liter

Figure 52. Volume of water reaching the wall surface and the moisture content (%) of drywall

4.5.1.2 West wall DS1 at the 0˚ wind direction

Figure 53 shows the moisture content of the West Wall affected by different volumes of water reaching its surface. Figure 53-a shows the moisture content of the drywall before the start of the tests and represents the dry condition, and Figure 53-f shows the moisture level at the end of the tests. As can be observed from these figures, the moisture content of the drywall increases by increasing the volume of water reaching the wall surface. The West Wall (as was shown in Figure 49) is directly opposite of the open window at the 0˚ wind direction. Therefore, the moisture content is symmetrically increasing on each side of this wall. It is noteworthy that moisture increase starts at the bottom of the wall then progresses upward toward the top. Also, it can be noted that even after the end of the test, the amount of water that has reached the wall is relatively low (i.e. less than 1 liter). This observation can be justified by the fact that in the case of DS1, there is only one opening on the building envelope (windward open window), and once the internal pressure reaches its maximum value, there is minimum air flow exchange between the exterior and interior building volume. This results in a weaker internal wind flow for DS1 compared to DS2 at the same wind direction of 0˚.

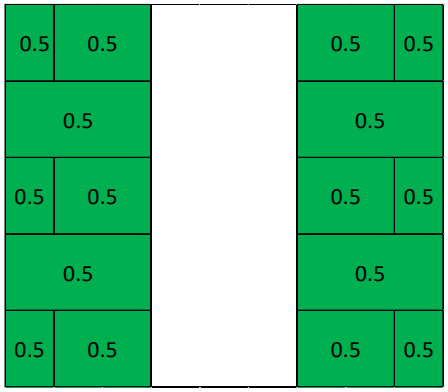

(a) volume of water = 0.00 liter

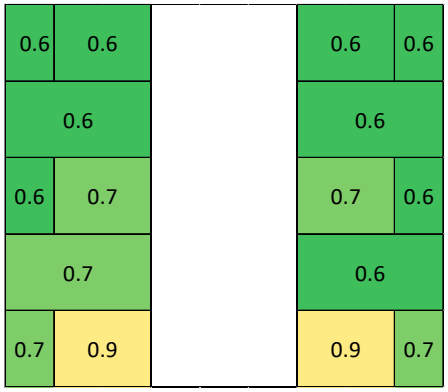

(d) volume of water = 0.24 liter

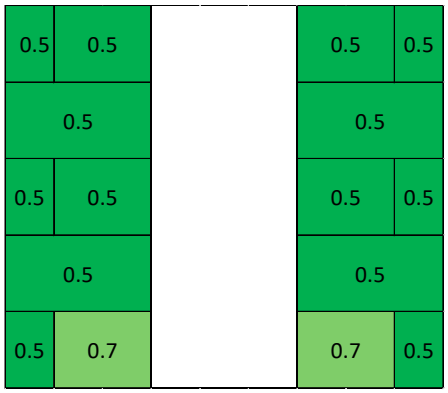

(b) volume of water = 0.04 liter

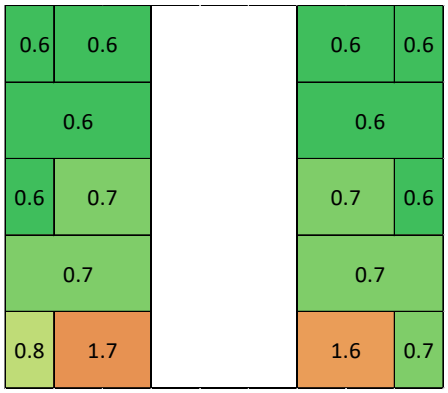

(e) volume of water = 0.42 liter

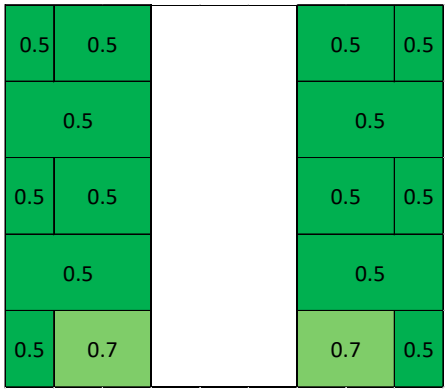

(c) volume of water = 0.08 liter

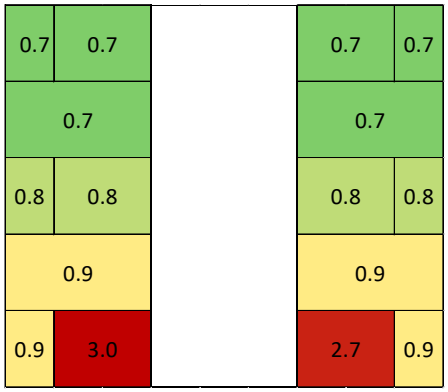

(f) volume of water = 0.84 liter

Figure 53. Volume of water reaching the wall surface and the moisture content (%) of drywall

4.5.1.3 North wall DS1 at the 0˚ wind direction

Figure 54 presents the moisture content of the North Wall at different levels of water exposures. Generally, it can be observed that this wall is minimally affected by the water intrusion. Even at the end of the tests, only 0.53 liters of water has reached the wall surface, and the highest moisture content is less than 1%. During the first three periods of water exposure (Figure 54-a, b, and c) there is not any notable increase in the moisture content. As soon as the volume of water reaches the 0.12-liter value, the moisture increase is initiated (Figure 54-d, e and f). After that point, although the whole surface is experiencing a moisture increase, only the lower half of the wall is affected by the direct impinging rain droplets, and the moisture increase on the upper half of the wall is caused by the high relative humidity inside the building.

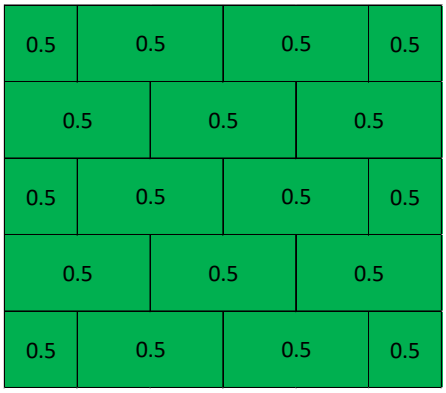

(a) volume of water = 0.00 liter

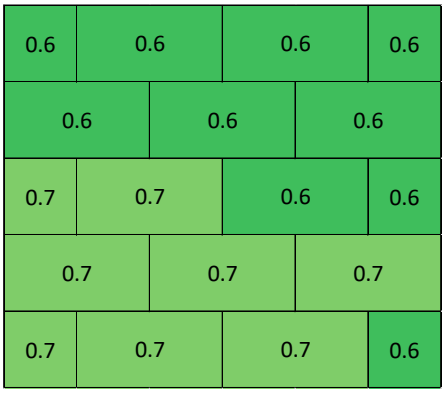

(d) volume of water = 0.12 liter

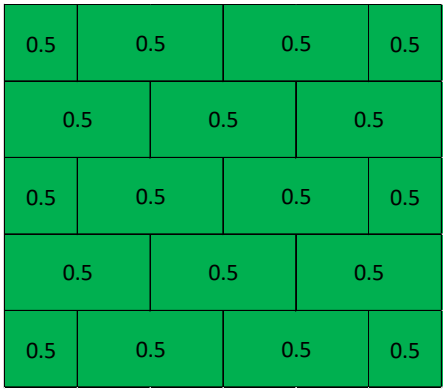

(b) volume of water = 0.01 liter

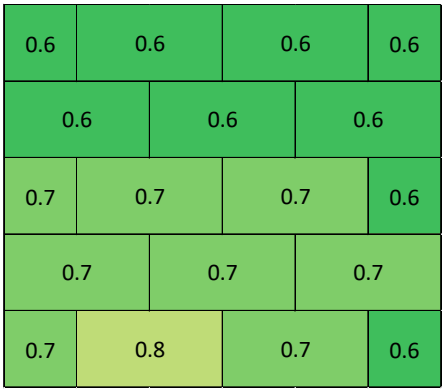

(e) volume of water = 0.18 liter

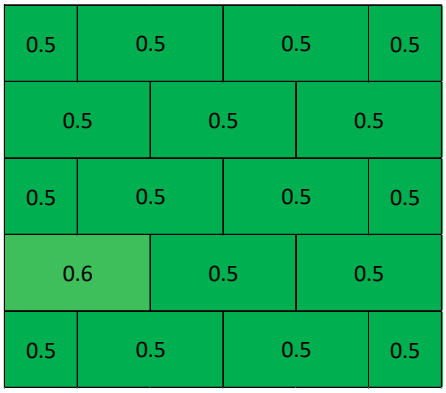

(c) volume of water = 0.03 liter

(f) volume of water = 0.53 liter

Figure 54. Volume of water reaching the wall surface and the moisture content (%) of drywall

4.5.1.4 South wall DS1 at 0˚ wind direction

The moisture content of the South Wall is presented in Figure 55. The general trend of moisture increase in this wall is very similar to the North Wall, which is expected based on the symmetric exposure condition of these two walls. This wall also experiences very limited exposure to the rain, even at the end of the tests (Figure 55-f), with only 0.53 liters of water reaching the wall surface, and the highest recorded moisture content at 1.4%. Similarly, no moisture increase is observed for the first three exposure periods (Figure 55-a, b, and c), and the moisture increase due to direct impinging occurs only at the lower part of the wall. The rest of the wall experiences moisture increase due to the increased level of the interior air humidity.

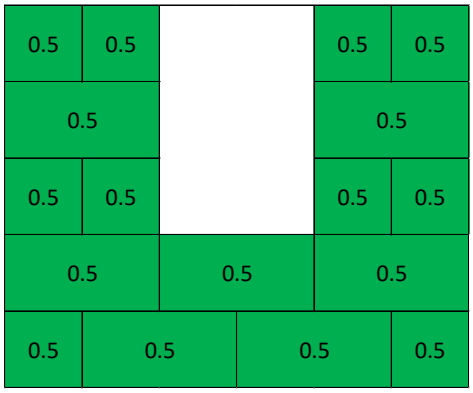

(a) volume of water = 0.00 liter

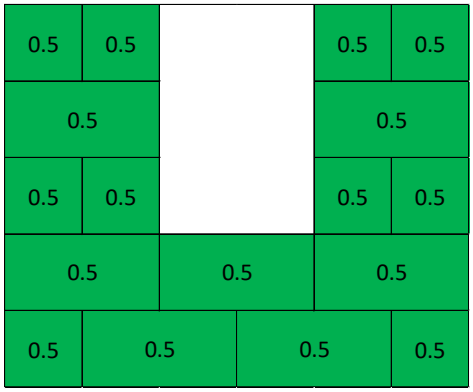

(b) volume of water = 0.01 liter

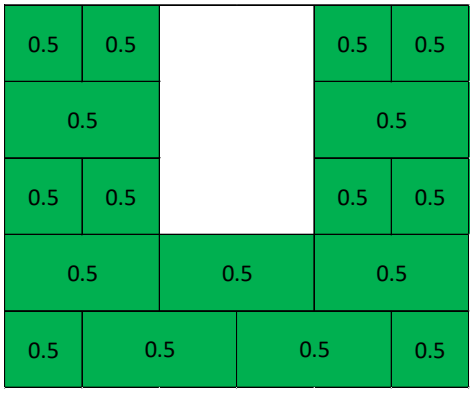

(c) volume of water = 0.03 liter

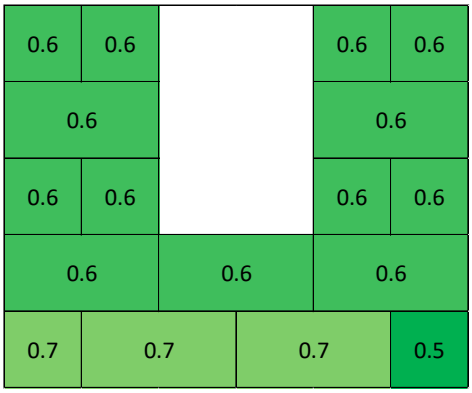

(d) volume of water = 0.12 liter

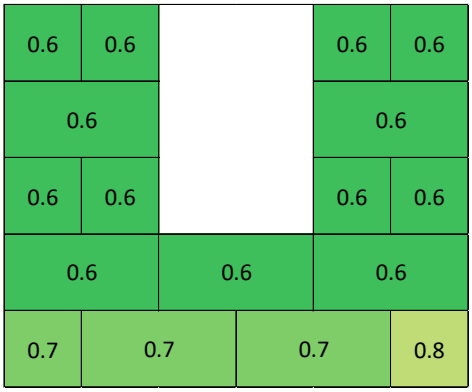

(e) volume of water = 0.18 liter

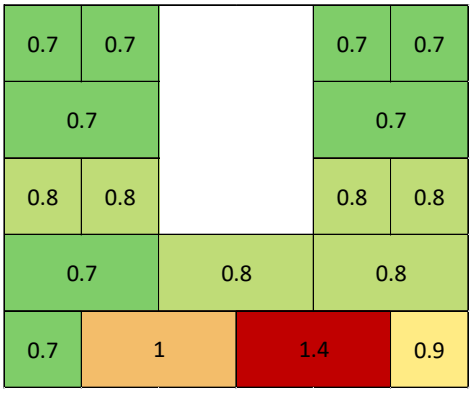

(f) volume of water = 0.53 liter

Figure 55. Volume of water reaching the wall surface and the moisture content (%) of drywall

4.5.2. Moisture content of the drywall for the DS1 model at the 45˚ wind direction

This section presents the results of full-scale experimental tests performed on the model with one open window at the East Wall and subjected to the 45˚ wind direction. In this case, the model was tested for two consecutive days. The first day tests started with the dry model. During the first day of tests, the model was subjected to rain exposure for three successive periods, including two 5-minute tests, followed by a 10-minute test. At the end of each test, the volume of runoff water on each wall surface was obtained from the accumulated water in the measuring bucket. Also, the amount of water that was absorbed by the drywall was calculated by multiplying the difference in moisture content after the test and dry condition to the tributary weight of drywall associated with the moisture measurement location on the wall. Summing up the values for all locations resulted in the amount of absorbed water by the wall. Finally, for each set of tests, the total amount of water reaching the wall and resulting in moisture increase at the end of that test was calculated as the summation of the accumulated water on the bucket since the start of the first set of tests plus the amount of absorbed water by the drywall at the end of the test.

The second-day tests started with the wet interior, with drywall holding some of the moisture load from the previous day. During the second day, the model was subjected to three periods of rain exposure, including 10-minute, 20-minute and 30-minute runtimes. Since it was required to calculate the amount of water reaching the interior walls at the start of the second-day tests based on the moisture level of the walls at the beginning of the second day, linear regression was applied to the data obtained from the

first-day tests. This resulted in a linear relationship between the volume of water reaching a wall surface and the amount of water absorbed by the wall (Figure 56). Then, the amount of water that reached the surface of a wall at the beginning of the second-day test was estimated using this relation and given the volume of absorbed water by the wall just before the start of the second-day tests.

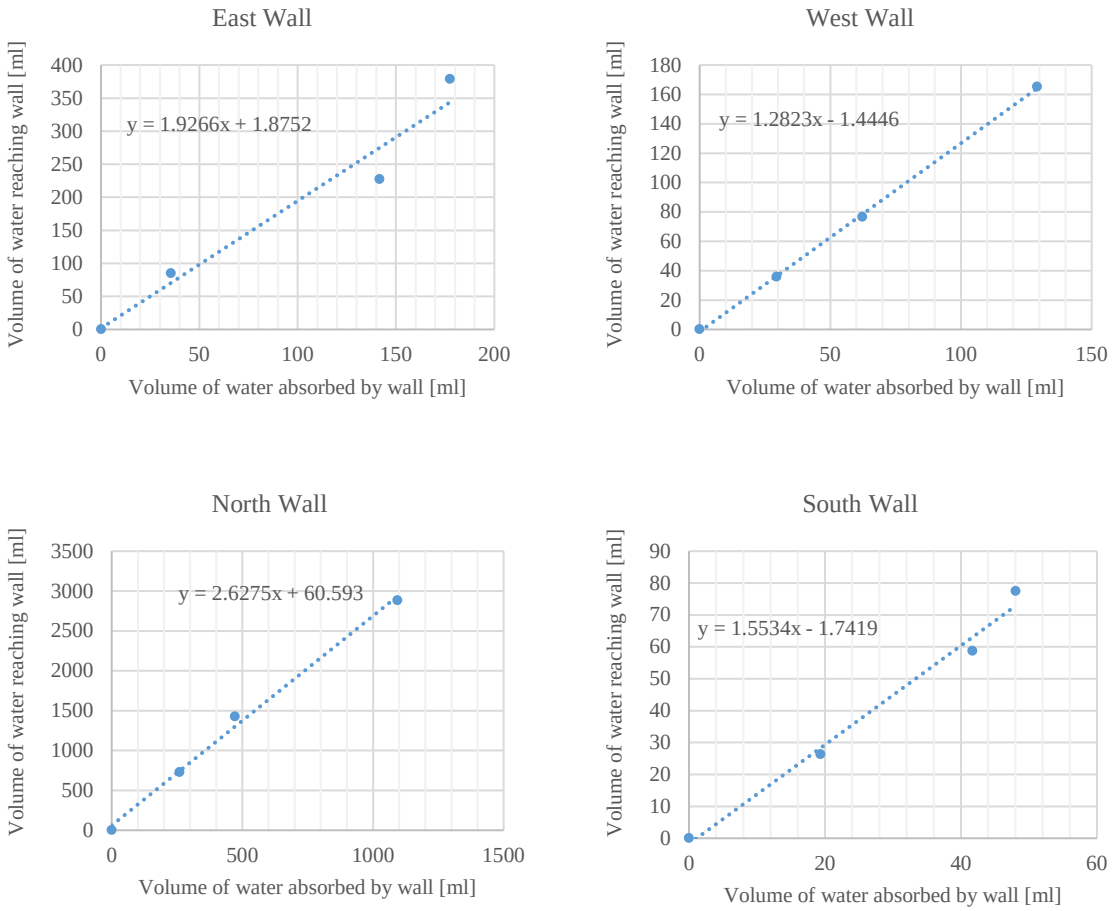

Figure 56. The experimental relation between the volume of water reaching the wall and absorbed water by the drywall for the first day of testing DS0 at the 45° wind direction

Once the amount of water that has reached a wall at the start of the second-day tests was estimated, the amount of water that has reached that wall at the end of each test

could be calculated by adding that initial value to the accumulative amount of water on the bucket since the start of second day plus the absorbed water by the drywall at the end of that test. The results for all the tests performed on the DS1 model subjected to the 45° wind angle are shown in Figure 57.

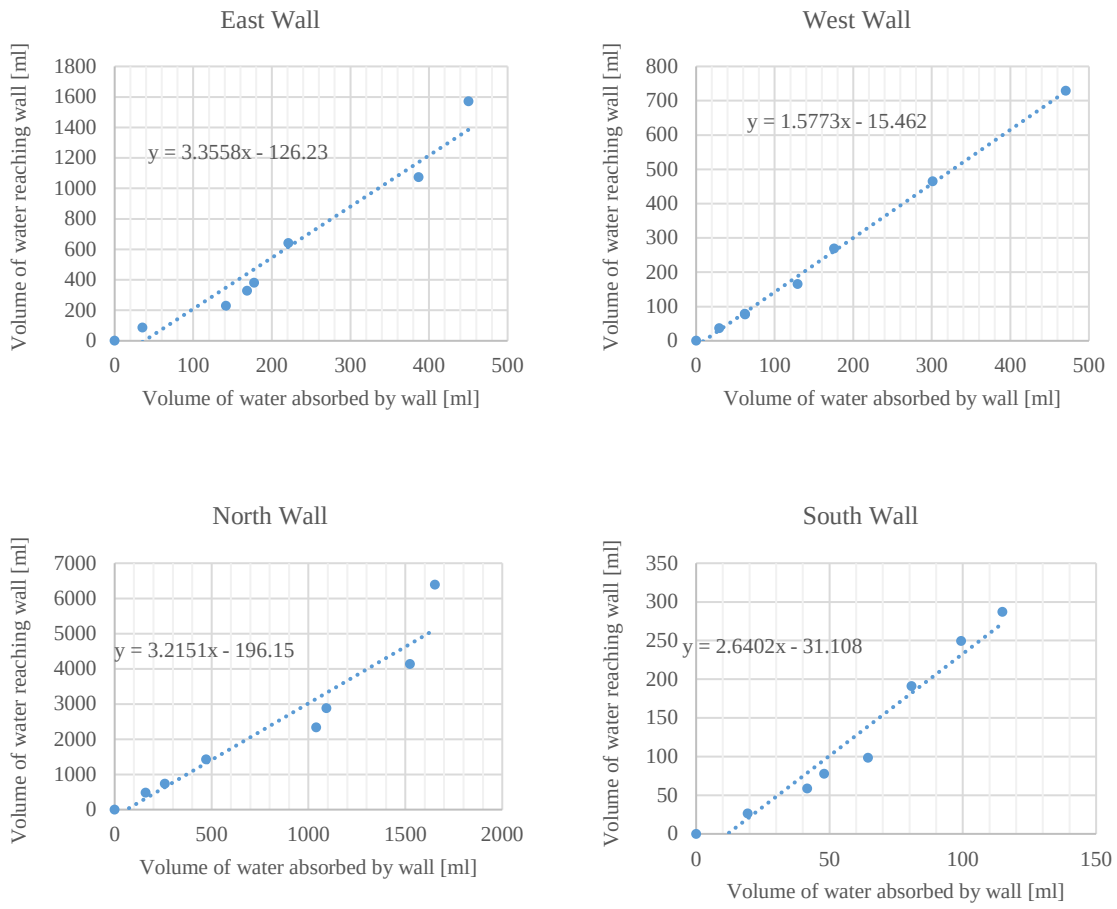

Figure 57. The experimental relation between the volume of water reaching the wall and absorbed water by the drywall for DS0 at the 45° wind direction

4.5.2.1 East wall DS1 at the 45˚ wind direction

The moisture content of the East Wall affected by different volumes of water reaching its surface is displayed in Figure 58. Figure 58-a shows the moisture content of

the dry condition of the wall before starting the tests. This wall is the one with the open windward window. At the 45°, wind direction, the wind blows at an inclined angle through this window. Immediately after the start of the first test, the humidity of the indoor environment increases and, as a result, there is a minor increase (from 0.5% to 0.6%) in the moisture content all across the wall surface (Figure 58-b). It can be observed that the bottom left corner of the window is the first location where a notable moisture increase is recorded, and this this can be justified by the oblique wind angle of attack (Figure 58-c). Also, as the tests continued (Figure 58-d, e and f), the left side of the wall experienced a relatively higher amount of moisture compared to the right side, which can be justified from the oblique angle of the wind toward the left side of the window. In fact, the right side of the window is not really affected by the rain droplets, because of the oblique angle of the wind, and it can be claimed that the increased moisture content (0.7%) at the right side is caused by the humid indoor environment.

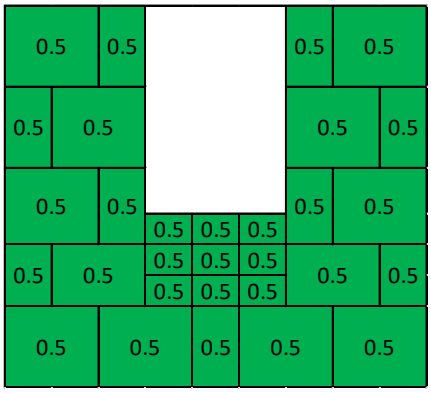

(a) volume of water = 0.00 liter

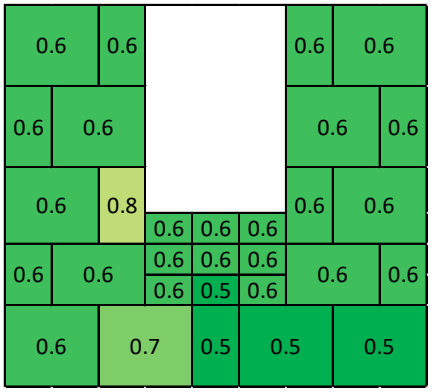

(b) volume of water = 0.08 liter

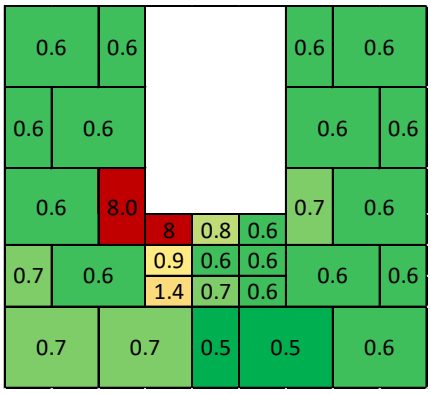

(c) volume of water = 0.23 liter

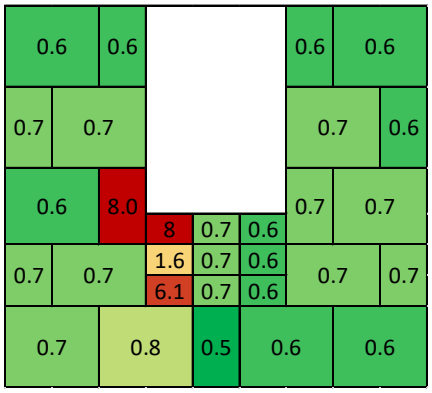

(d) volume of water = 0.38 liter

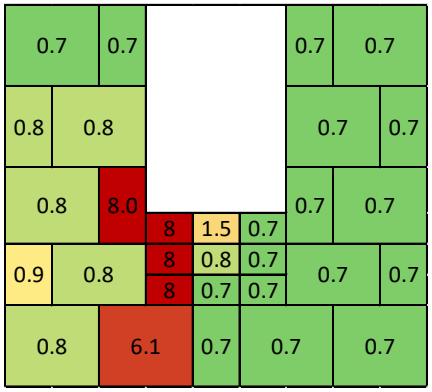

(e) volume of water = 1.07 liter

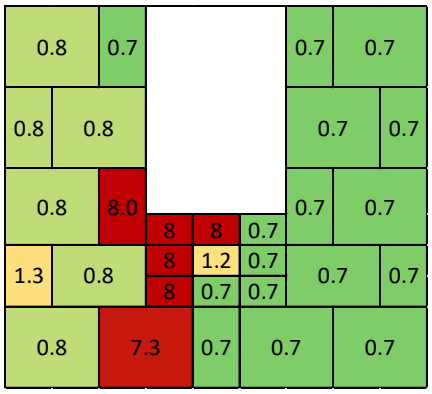

(f) volume of water = 1.57 liter

Figure 58. Volume of water reaching the wall surface and the moisture content (%) of drywall

4.5.2.2 West Wall DS1 at the 45˚ wind direction

Figure 59 shows the moisture content of the West Wall subjected to different volumes of water reaching its surface. This is the wall directly opposite of the open window. The tests start with the dry condition and with the moisture content of 0.5% across the whole wall surface (Figure 59-a). It can be noted that the moisture increase starts at the right half of the wall (Figure 59-b). All along the experiment, the right half of the wall keeps absorbing more moisture compared to the left half, and the bottom right corner of the wall tends to be the most affected part (Figure 59-c, d, e, and f). In fact, the left side of the door is barely affected by the rain droplets, and the moisture increase that it experiences is only because of the increase in the indoor humidity. This observation can be justified by the oblique angle of internal wind at the 45° wind direction. Unlike the 0° wind direction, at 45° wind angle, the internal wind flow is directed toward the North Wall rather than directly aiming at the West Wall and, as a result, only the right side of the West Wall (the side close to the North Wall) gets direct impinging rain on its surface.

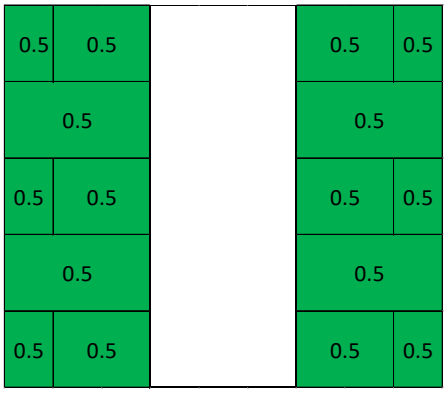

(a) volume of water = 0.00 liter

(d) volume of water = 0.16 liter

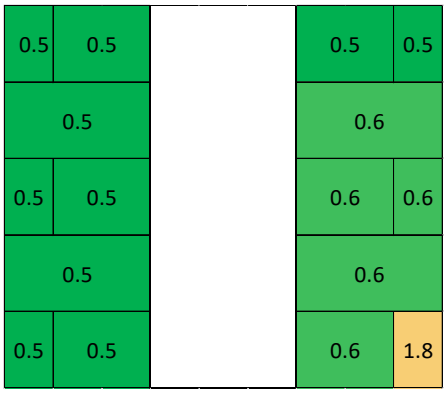

(b) volume of water = 0.04 liter

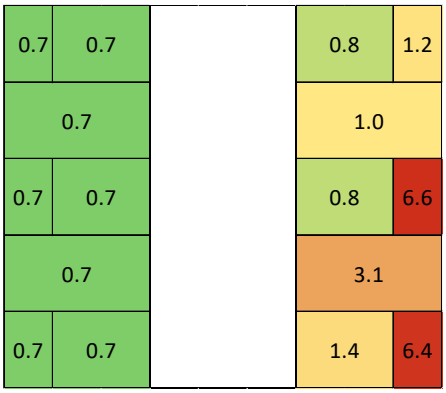

(e) volume of water = 0.46 liter

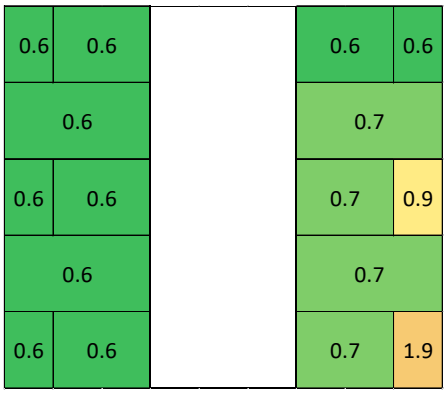

(c) volume of water = 0.08 liter

(f) volume of water = 0.73 liter

Figure 59. Volume of water reaching the wall surface and the moisture content (%) of drywall

4.5.2.3 North Wall DS1 at the 45˚ wind direction

The moisture content measurement of the North Wall and the corresponding volume of water reaching its surface are presented in Figure 60. The tests started with the dry condition and with the moisture content of 0.5% at the drywall (Figure 60-a). Immediately after the start of the first test, the moisture content at the drywalls experiences a considerable increase (Figure 60-b). This wall is the direct target of the wind flow at the 45° wind direction, so this notable increase after the first period of water exposure was expected. The rapid increase in the moisture continues toward the end of the tests (Figure 60-c, d, e, and f). All along the tests, the bottom portion of the wall, which is exposed to both direct impinging and the runoff water from above, absorbs the highest amount of moisture, while the top of the wall, which is barely subjected to rain impinging on its surface, absorbs the least amount of moisture.

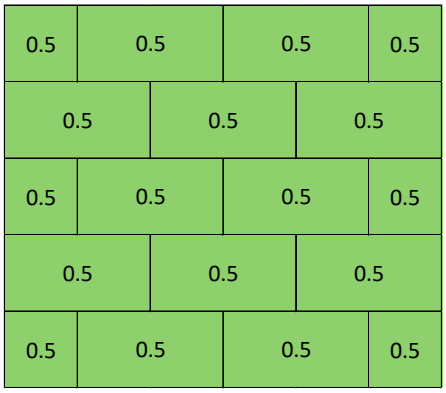

(a) volume of water = 0.00 liter

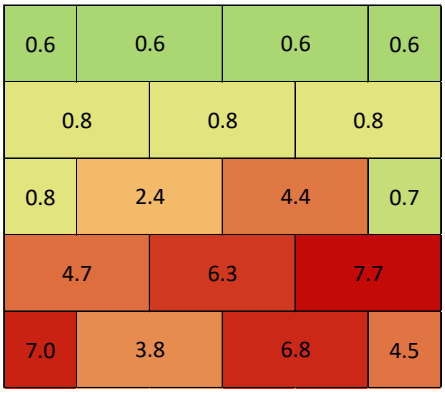

(d) volume of water = 2.89 liter

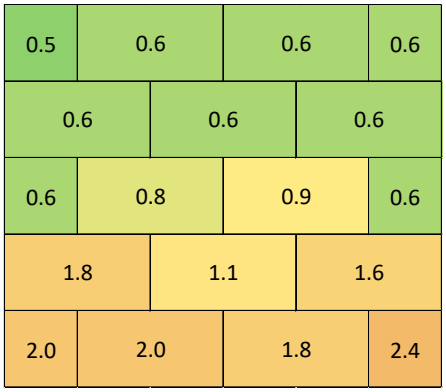

(b) volume of water = 0.73 liter

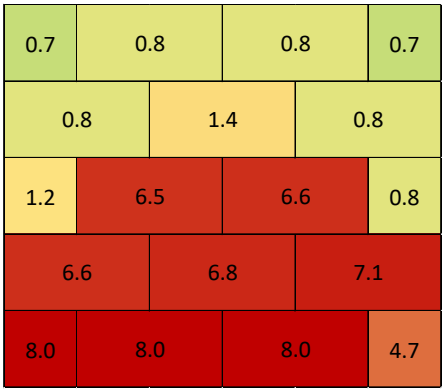

(e) volume of water = 4.13 liter

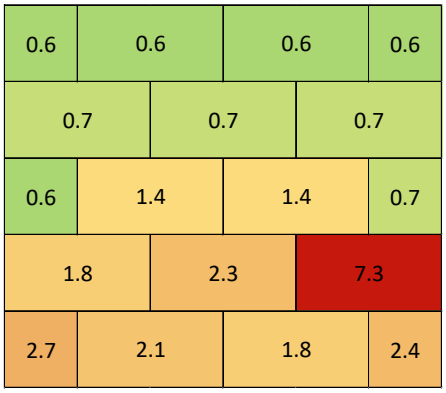

(c) volume of water = 1.42 liter

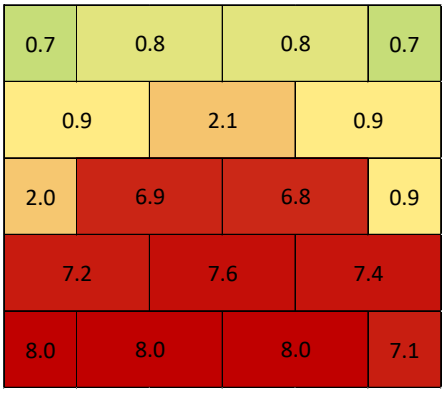

(f) volume of water = 6.39 liter

Figure 60. Volume of water reaching the wall surface and the moisture content (%) of drywall

4.5.2.4 South wall DS1 at the 45˚ wind direction

Figure 61 shows the moisture content of the South Wall affected by different volumes of water reaching its surface. The dry condition of the wall before the start of the tests is presented in Figure 61-a. For the DS1 model subjected to the 45˚ wind direction, this wall is hardly exposed to the raindrops carried by the internal wind flow. As can be observed, the notable moisture increase starts below and close to the bottom corners of the window (Figure 61-e) once 0.25 liters of water reaches the wall. Based on these observations, it can be safely assumed that the moisture increase of the wall is caused by the water penetration through the defects of the closed window. The closed window on the South Wall is directly subjected to the 45˚ wind flow and, as a result, the water can intrude through the existing defects and cracks in the window seal and make the drywall wet as it moves toward the bottom of the wall.

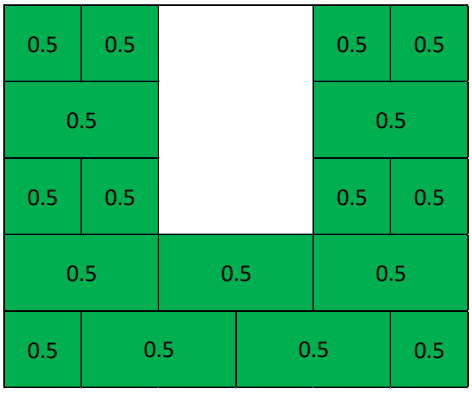

(a) volume of water = 0.00 liter

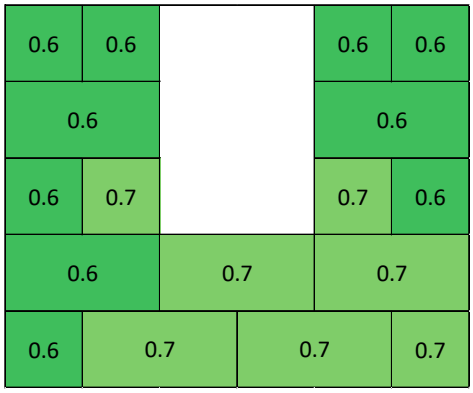

(d) volume of water = 0.08 liter

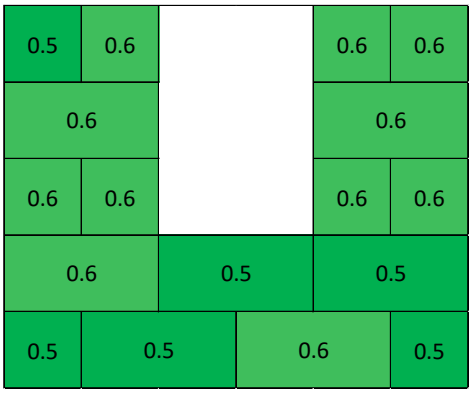

(b) volume of water = 0.03 liter

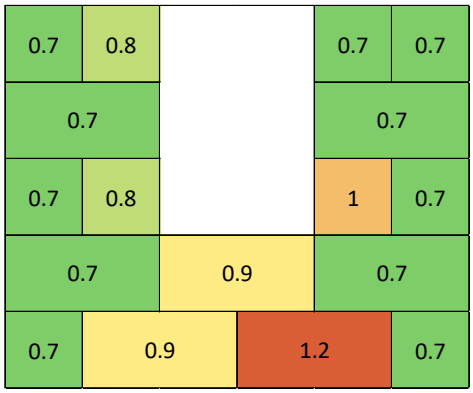

(e) volume of water = 0.25 liter

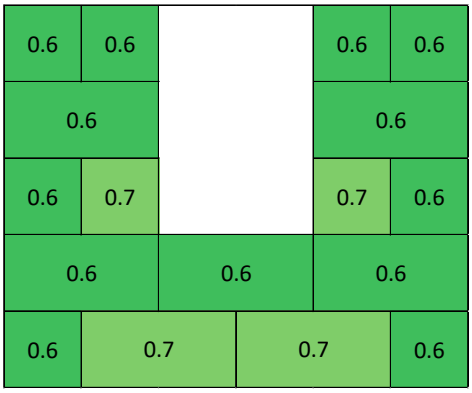

(c) volume of water = 0.06 liter

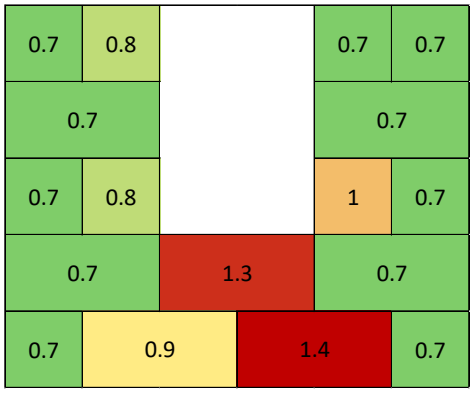

(f) volume of water = 0.29 liter

Figure 61. Volume of water reaching the wall surface and the moisture content (%) of drywall

4.5.3. Moisture content of the drywall for the DS2 model at the 0˚ wind direction

The results of full-scale experimental tests performed on the model with two open windows and at the 0˚ wind direction are presented in this section. For this case, the experimental tests were performed on two successive days. On the first day, the experiment included two 5-minute rain exposures followed by a 10-minute test. During the second day, the model was subjected to consecutive 10-minute, 15-minute and 30-minute rain intrusion tests. Only the first test period started with a dry model condition. As explained in the previous sections, before the start of the second day of testing, the model had partially lost the moisture absorbed during the previous day. Thus, it was required to estimate the expected amount of water that could result in the remaining moisture on the walls at the beginning of the second day of testing. Linear regression was applied to the data obtained from the consecutive tests performed during the first day of testing. Figure 62 shows the obtained relation between the volume of water reaching each interior wall surface and the amount of absorbed water by that wall for the tests performed during the first day of the experiment. The amount of expected water reaching the wall before the start of the second day was estimated using these relations and given the amount of residual absorbed water on the wall. Figure 63 shows the results of all tests, and the relation between the amount of water reaching different interior walls and the amount of water absorbed by the walls.

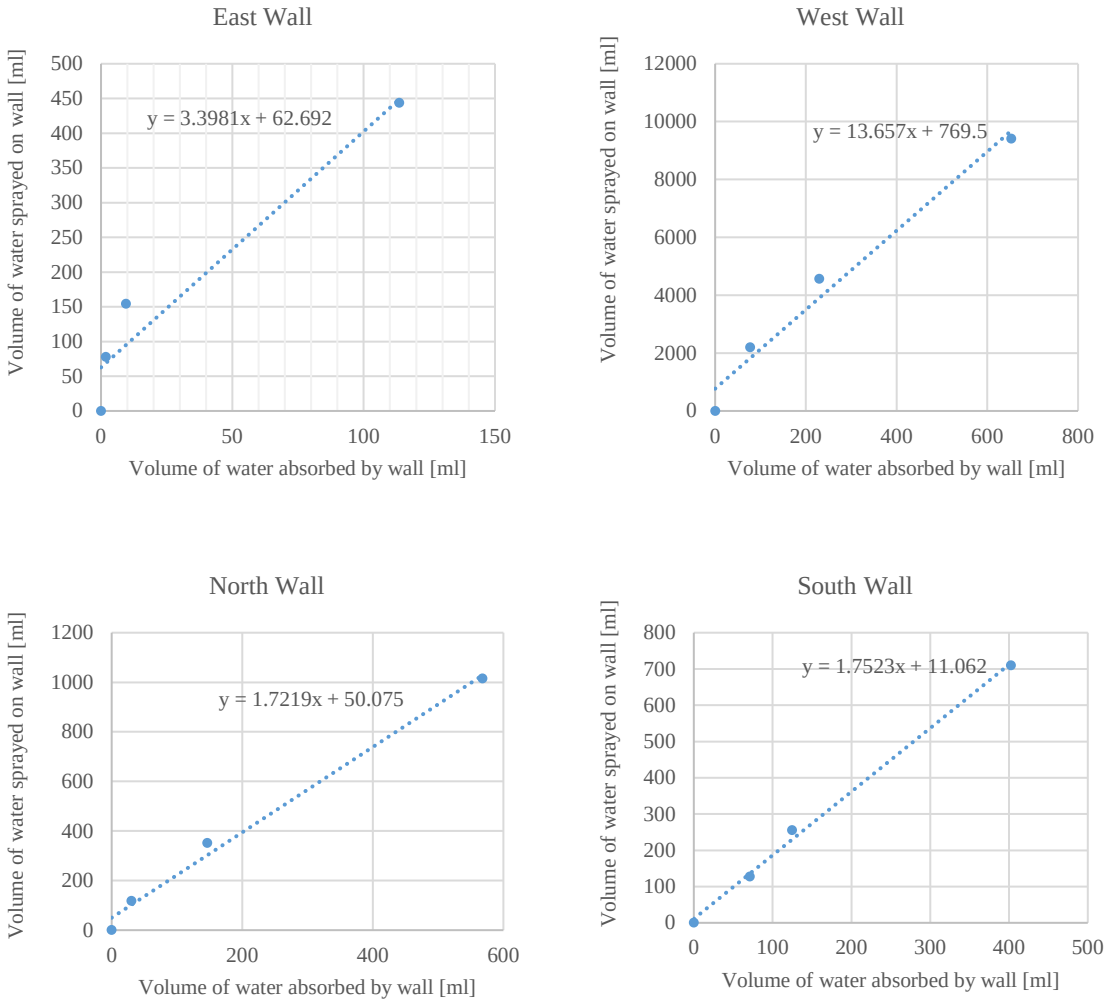

Figure 62. The experimental relation between the volume of water reaching the wall and absorbed water by the drywall for the first day of testing DS2 at the 0° wind direction

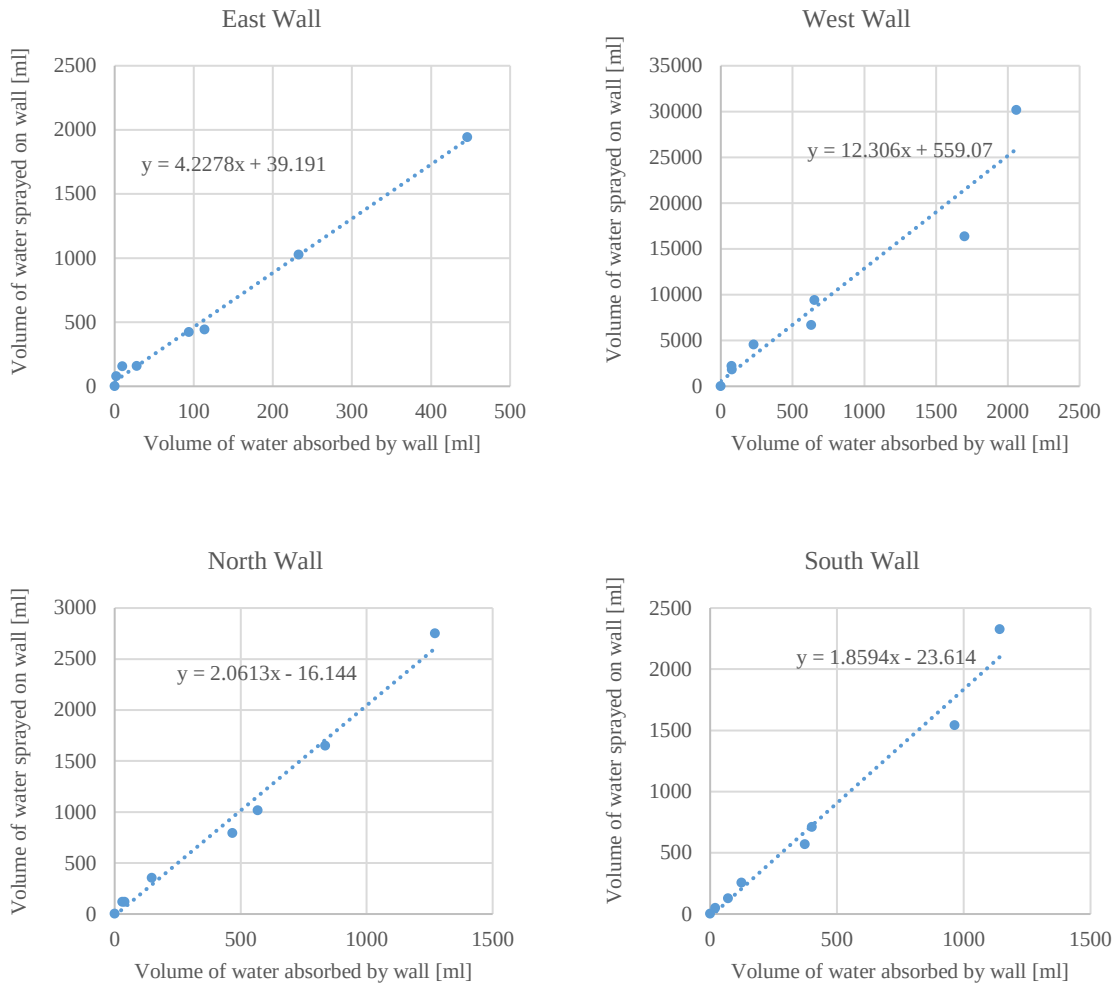

Figure 63. The experimental relation between the volume of water reaching the wall and absorbed water by the drywall for DS2 at the 0° wind direction

4.5.3.1 East Wall DS2 at the 0˚ wind direction

The moisture content of the East Wall corresponding to different volumes of water reaching its surface is presented in Figure 64. The experiment begins with the dry building interior, as shown in Figure 64-a. As can be observed, there is not any significant increase of moisture content up until 0.44 liters of water reaches the wall surface (Figure 64-d) and affects the drywall adjutant to the bottom right corner of the window. Another notable observation is the different patterns of moisture increase for

DS1 and DS2 models at the 0˚ wind direction. At this wind angle, the water can intrude only through the windward window, which is identical between these models. The only difference is the second open window at the South Wall of the DS2 model. While for the DS1 model at the 0˚ wind angle, at the end of the experiment, minimal moisture increase was observed at the top portion of the wall (Figure 52-f); at the end of DS2 model tests, a notable moisture increase could be observed all across the wall (Figure 64-f). This observation can be caused by the open window at the South Wall that works like an outlet for the internal wind flow and facilitates the entrance of wind flow through the windward open window on the East Wall. This results in a more powerful internal wind flow in the DS2 model compared to the DS1 model and, as a result, the rain droplets can better spread in the building interior and affect the whole interior wall surfaces.

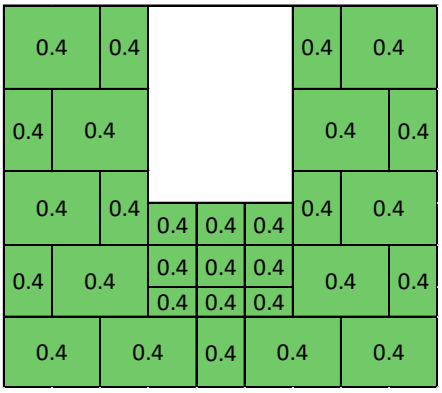

(a) volume of water = 0.00 liter

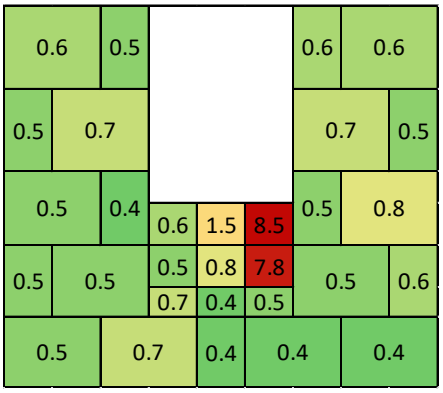

(d) volume of water = 0.44 liter

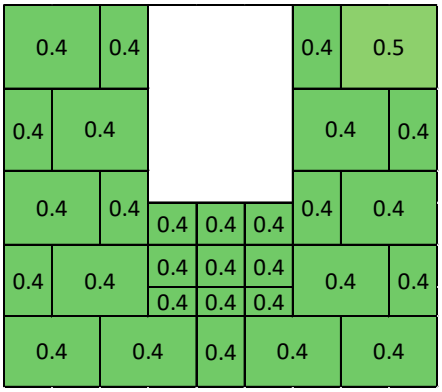

(b) volume of water = 0.08 liter

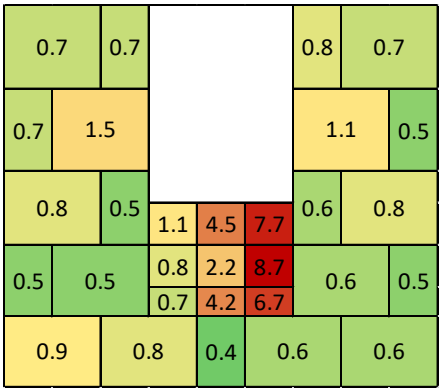

(e) volume of water = 1.03 liter

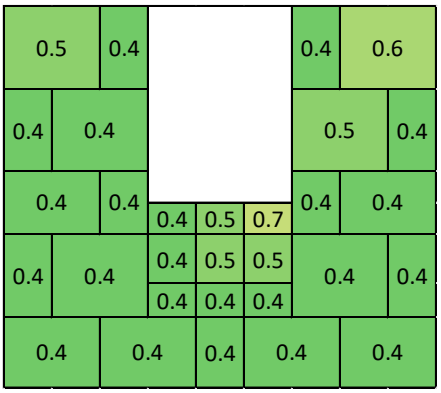

(c) volume of water = 0.15 liter

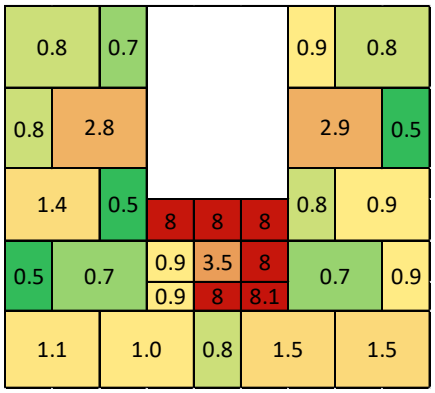

(f) volume of water = 1.91 liter

Figure 64. Volume of water reaching the wall surface and the moisture content (%) of drywall

4.5.3.2 West Wall DS2 at the 0˚ wind direction

Figure 65 shows the moisture content of the West Wall affected by different volumes of water reaching its surface. The initial dry condition is displayed in Figure 65-a. It can be observed that a considerable amount of water (2.2 liters) reaches this wall immediately after the first run of the tests and results in a notable increase of moisture content at the bottom of the wall (Figure 65-b). This wall is directly opposite the open window at the 0˚ wind angle of attack similar to the case of DS1 at the 0 ˚ wind direction. However, the amount of water that reaches this wall is considerably higher compared to the DS1 model. At the end of the DS2 experiment (Figure 65-f), 30.18 liters of water reach this wall, while at the end of DS1 experiment, the wall gets only 0.84 liters of water (Figure 52-f). This considerable difference is caused by the internal wind flow generated by the open window on the South Wall of the DS2 model. This powerful internal wind flow spreads the rain droplets all across the surface of the wall, so unlike the DS1 model, where only the bottom of the wall is affected, the whole surface of the wall becomes wet at the end of the DS2 model test.

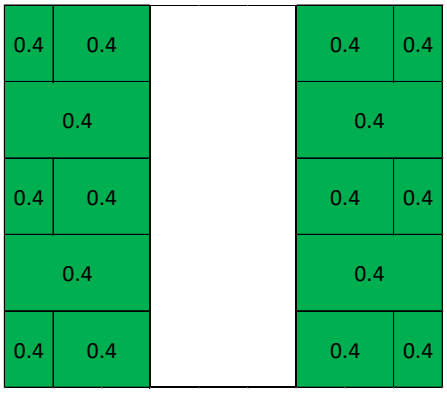

(a) volume of water = 0.00 liter

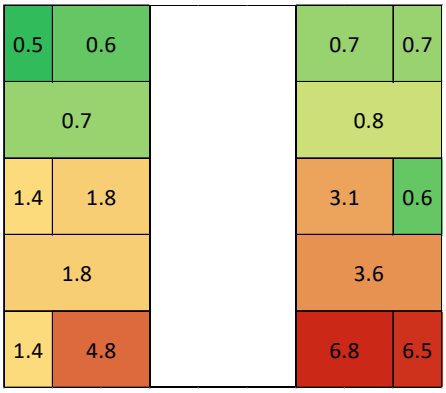

(d) volume of water = 9.41 liter

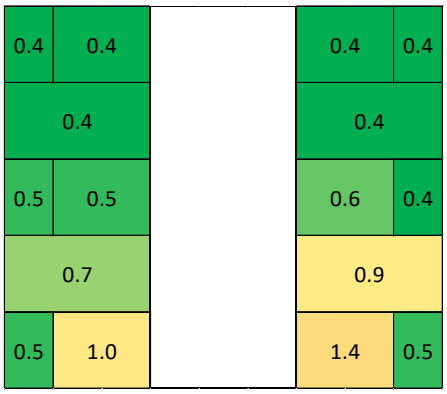

(b) volume of water = 2.20 liter

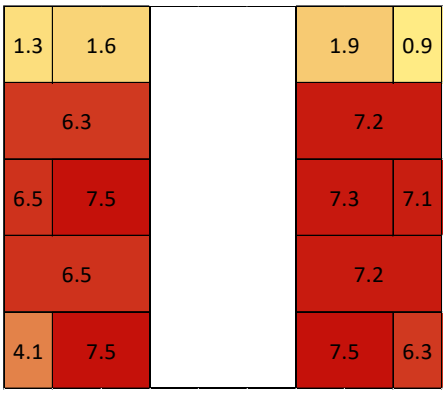

(e) volume of water = 16.35 liter

(c) volume of water = 4.57 liter

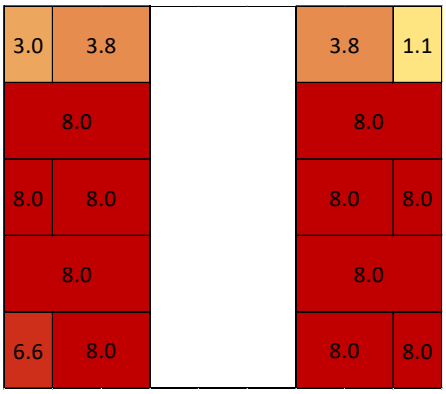

(f) volume of water = 30.18 liter

Figure 65. Volume of water reaching the wall surface and the moisture content (%) of drywall

4.5.3.3 North Wall DS2 at the 0˚ wind direction

The trend of increase in moisture content by increasing the volume of water is displayed in Figure 66 for the North Wall. At the start of the tests, the drywall is dry and the moisture content is equal to 0.4% across the wall (Figure 66-a). The bottom left corner of the wall is the first location where the moisture content begins to increase as the volume of water that reaches the wall increases (Figure 66-b). This corner is adjacent to the West Wall (the wall opposite the open windward window). As the tests continue, the wetness expands from this location toward the diameter of the wall (Figure 66-c, d and e). At the end of the test, a total of 2.75 liters of water reach the wall and only the left edge of the wall remains unaffected (Figure 66-f). Compared to the case of DS1 at the 0˚ wind direction (Figure 60-f), the effect of moisture is considerably higher for the North Wall at DS2. In this case, also, the effect of the open window on the South Wall and the more powerful internal wind flow causes the better spread of the raindrops on the North wall and results in the higher moisture absorption at DS2 compared to DS1.

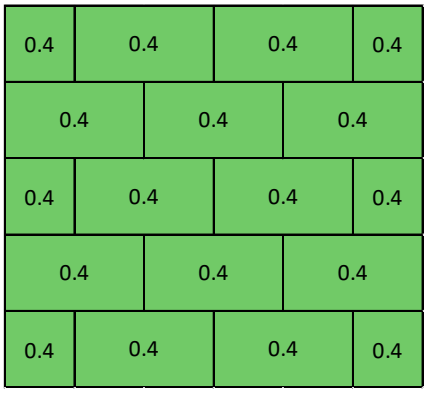

(a) volume of water = 0.00 liter

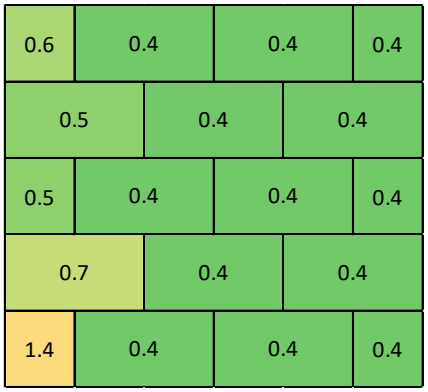

(b) volume of water = 0.12 liter

(c) volume of water = 0.35 liter

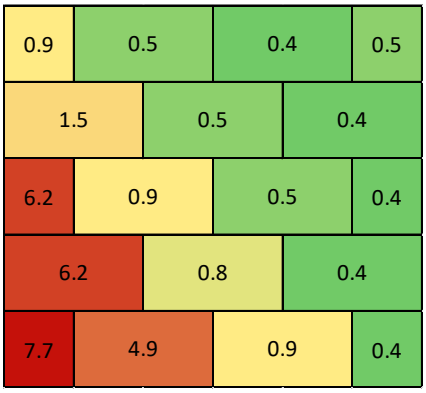

(d) volume of water = 1.01 liter

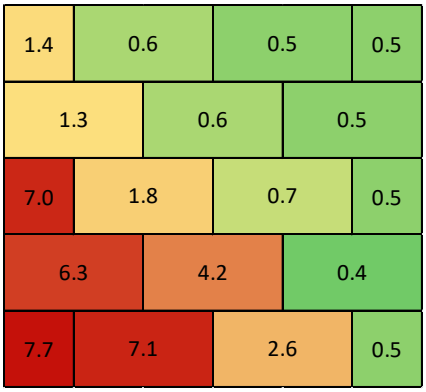

(e) volume of water = 1.65 liter

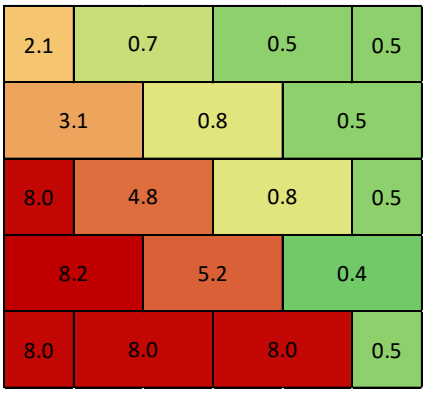

(f) volume of water = 2.75 liter

Figure 66. Volume of water reaching the wall surface and the moisture content (%) of drywall

4.5.3.4 South Wall DS2 at the 0˚ wind direction

Figure 67 shows the moisture content of the South Wall affected by different volumes of water reaching its surface. As can be observed, this wall has a very similar wetness pattern to the North Wall (Figure 52). In this case, the bottom right corner of the wall is the first location where the moisture increase is obvious. This corner is on the side adjacent to the West Wall (the wall opposite the open windward window). By increasing the volume of water, the moisture expands toward the diameter of the wall. At the end of the test, a total of 2.32 liters of water reach this wall, which is relatively higher compared to the case where the model was subjected to the 0˚ wind angle. In that case, there was only one open window on the East Wall (DS1 tests at the 0˚ wind direction, in Figure 55). As previously explained, the second window on South Wall takes out the wind coming through the windward window on East Wall, and results in a more powerful internal wind flow. As a result, the impact of moisture propagation becomes more extended in the model with two open windows (the DS2 model) subjected to the same wind direction of 0˚.

(a) volume of water = 0.00 liter

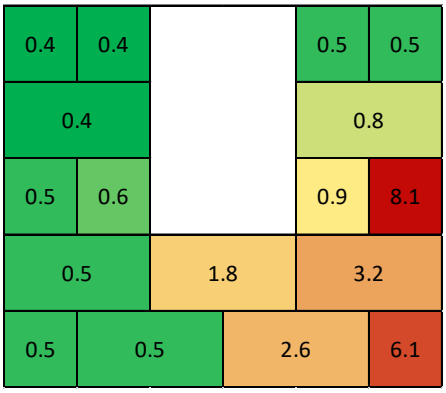

(d) volume of water = 0.71 liter

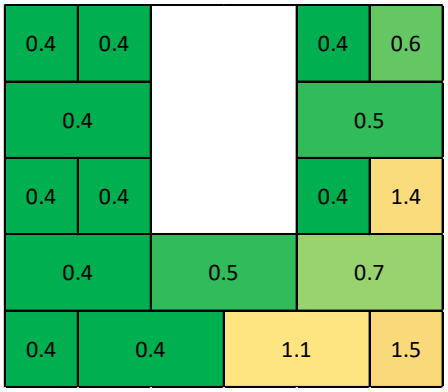

(b) volume of water = 0.13 liter

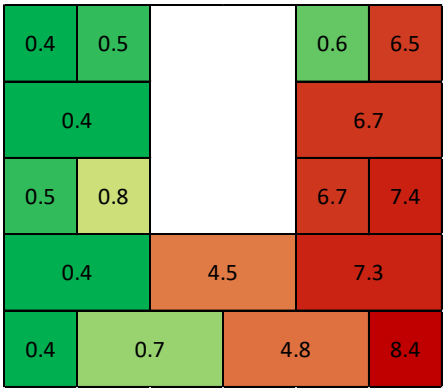

(e) volume of water = 1.54 liter

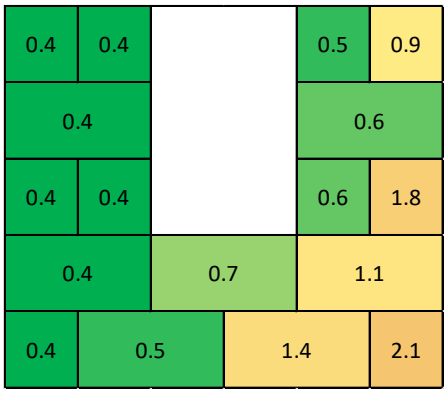

(c) volume of water = 0.26 liter

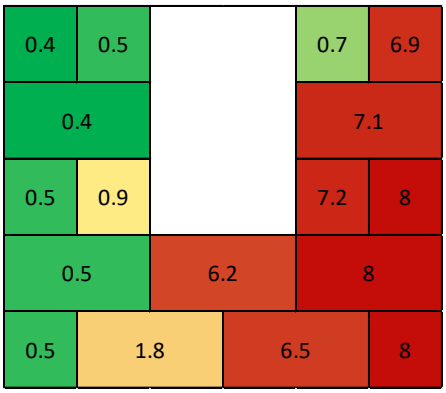

(f) volume of water = 2.32 liter

Figure 67. Volume of water reaching the wall surface and the moisture content (%) of drywall

4.6. Water Volume-Damage Relations

In this section, an effort to evaluate the sustained damage by the internal walls based on the absorbed moisture content by the gypsum board covering the wall surface is taken. Although there are several standard procedures for evaluating the physical and mechanical properties of gypsum boards (ASTM C472, 2012 and ASTM C1396, 2014), there is very little information in the literature regarding the moisture content threshold of Gypsum Wallboard that results in its failure. According to the technical document by Gypsum Association, 2010, the gypsum sheathing board has a maximum water absorption of 10%, while the water-resistant gypsum board has the maximum water absorption capacity of 5%. However, neither of these two types is used for the interior drywall. Gypsum sheathing board is mainly used for the building exterior, and water-resistant gypsum board is typically used in the bathrooms, where there is a high potential for moisture exposure and the fungal growth. According to an article by Harriman, 2006, for most of the gypsum boards, 2% of the weight is the highest moisture content that they can hold before crumbling apart. The lack of information on the moisture failure of gypsum wallboard is mainly because of the fact that this product is not supposed to be exposed to water and gotten wet in the first place.

On the other hand, the functionality of drywall is not only restricted by its physical properties. Gypsum is a permeable material highly prone to fungal growth (Nielsen, Holm, P., & Nielsen, 2004, Pasanen, Juutinen, Jantunen, & Kalliokoski, 1992 and Johansson, Ekstrand-Tobin, Svensson, & Bok, 2012). Based on the technical report by the Gypsum Association, 2015, the mold growth can start in the gypsum board if it is

not completely dried in 24 to 48 hours. According to ANSI/IICRC S500, 2015 standard for water damage restoration, although the falling rainwater is defined as category 1 water ("water that originates from a sanitary water source and does not pose substantial risk from dermal, ingestion or inhalation exposure"), but it can deteriorate to category 3 water ("water that is grossly contaminated and can contain pathogenic, toxigenic or other harmful agents to humans") once the microorganisms become wet, depending upon the length of time and temperature. The experience from the previous hurricanes has shown that in many cases the water damage restoration is not possible until weeks after the event. Therefore, it is not unrealistic to assume that the absorbed water by the drywall changes to category 3 water and the fungal growth occurs on any drywall that gets wet by intruded water during the hurricane.

Based on ANSI/IICRC S500, 2015 standard, the drywalls affected by category 3 water are "Unrestorable," and should be removed and replaced. Based on the information obtained from the literature, it was decided that any drywall that gets wet by direct impinging of water on its surface during the experimental tests needs to be removed and replaced. Additionally, it was decided that the sustained damage by the interior wall will be presented as the percentage of the drywall that needs to be replaced.

It was decided that drywall needs to be replaced at any location where the direct impinging water results in a moisture content of 0.7% or higher. However, as explained earlier in this chapter, the decision on whether the moisture increase is caused by the increased indoor humidity or direct impinging of rain on the surface requires engineering judgment. Therefore, for each of the interior walls (e.g. East, West, North and South

walls), at the end of each experimental water exposure period, the percentage of the drywall area that experienced a moisture content of 0.7% or higher due to impinging water on its surface was reported as the percentage of the damage sustained by that interior wall. Since the volume of water that reached the interior wall surface at the end of each water exposure period was also determined (as explained in section 4.5), it was possible to define a relationship between the percentage of sustained damage by the interior wall and the volume of water that reaches that wall surface. In this study, the percentage of damage was defined as the percentage of the wall area that needs to be removed and replaced to the total area of the wall. This criterion can be easily used in the loss estimation models to calculate the loss as the repair/replacement cost to the initial cost of the component.

Table 15 to Table 18 present the relationship between the volume of water that reaches each of the interior walls and the sustained damage by the wall. It is noteworthy that a higher volume of water does not always lead to a higher percentage of the damage. This is caused by the different wetness patterns associated with different test configurations. For example, the 1.36 liters of water that reach the East Wall of the DS1 model at the 0˚ wind direction (Figure 52-c) can only affect the drywall below the height of the window and result in 40% damage, while the 1.03 liters of water that reach the same wall of the DS2 model at the 0˚ wind direction (Figure 58-e) can lead to a more uniform wetness trace all across the wall, and result in 70% damage.

Table 15. Relation between the volume of water reaching the East Wall and the sustained damage

Test Case	Water Volume (liter)	Percentage of damage
DS1-0wind	0.00	0%
DS2-0wind	0.08	0%
DS1-45wind	0.08	10%
DS2-0wind	0.15	15%
DS1-45wind	0.23	25%
DS1-45wind	0.38	50%
DS2-0wind	0.44	50%
DS1-0wind	0.75	40%
DS2-0wind	1.03	70%
DS1-45wind	1.07	70%
DS1-0wind	1.36	40%
DS1-45wind	1.57	100%
DS2-0wind	1.94	100%
DS1-0wind	2.38	80%
DS1-0wind	3.43	80%
DS1-0wind	7.09	100%

Table 16. Relation between the volume of water reaching the West Wall and the sustained damage

Test Case	Water Volume (liter)	Percentage of damage
DS1-0wind	0.00	0%
DS1-45wind	0.04	5%
DS1-0wind	0.04	15%
DS1-45wind	0.08	40%
DS1-0wind	0.08	15%
DS1-45wind	0.17	45%
DS1-0wind	0.24	35%
DS1-0wind	0.42	50%
DS1-45wind	0.46	50%
DS1-45wind	0.73	60%
DS1-0wind	0.84	80%
DS2-0wind	2.20	60%
DS2-0wind	4.57	70%
DS2-0wind	9.41	80%
DS2-0wind	16.35	100%
DS2-0wind	30.18	100%

Table 17. Relation between the volume of water reaching the North Wall and the sustained damage

Test Case	Water Volume (liter)	Percentage of damage
DS1-0wind	0.00	0%
DS1-0wind	0.01	0%
DS1-0wind	0.03	5%
DS2-0wind	0.12	15%
DS1-0wind	0.12	40%
DS1-0wind	0.18	50%
DS2-0wind	0.35	35%
DS1-0wind	0.53	60%
DS1-45wind	0.73	70%
DS2-0wind	1.01	50%
DS1-45wind	1.43	80%
DS2-0wind	1.65	70%
DS2-0wind	2.75	80%
DS1-45wind	2.88	90%
DS1-45wind	4.13	100%
DS1-45wind	6.39	100%

Table 18. Relation between the volume of water reaching the South Wall and the sustained damage

Test Case	Water Volume (liter)	Percentage of damage
DS1-0wind	0.00	0%
DS1-0wind	0.01	0%
DS1-45wind	0.03	5%
DS1-0wind	0.03	0%
DS1-45wind	0.06	10%
DS1-45wind	0.08	15%
DS1-0wind	0.12	15%
DS2-0wind	0.13	20%
DS1-0wind	0.18	20%
DS1-45wind	0.25	30%
DS2-0wind	0.26	40%
DS1-45wind	0.29	45%
DS1-0wind	0.61	50%
DS2-0wind	0.71	50%
DS2-0wind	1.54	60%
DS2-0wind	2.33	70%

Finally, for each interior wall, the above results were grouped into discrete levels of water volume that can result in different ranges of physical damage, as displayed in Figure 68 to Figure 71. The horizontal axis of these graphs shows the volume of water, and the vertical axis shows the probable damage by the partition. For example, if the East Wall (Figure 68) is subjected to less than 0.5 liters of water during the hurricane-induced water intrusion, the median of the sustained damage by the wall would be 20%.

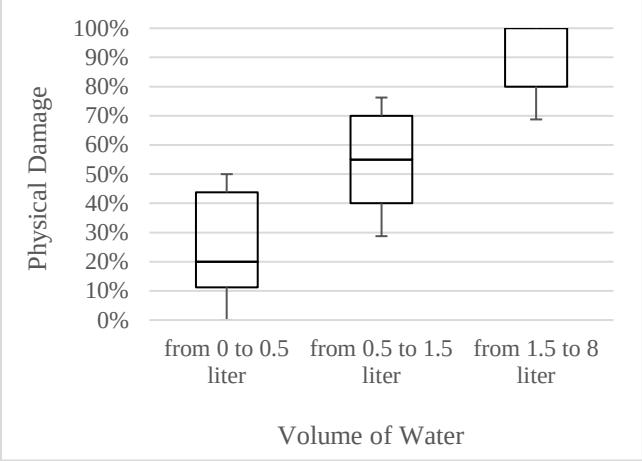

Figure 68. Physical Damage-Volume of water relation for East Wall

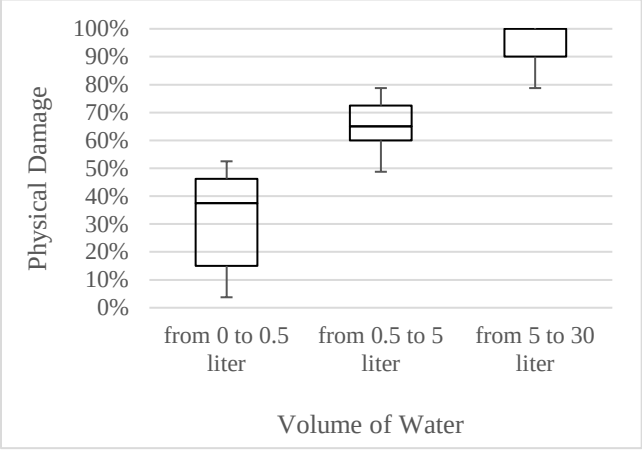

Figure 69. Physical Damage-Volume of water relation for the West Wall

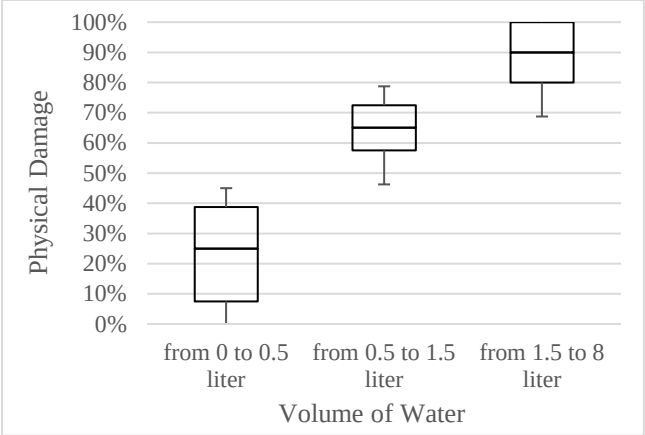

Figure 70. Physical Damage-Volume of water relation for the North Wall

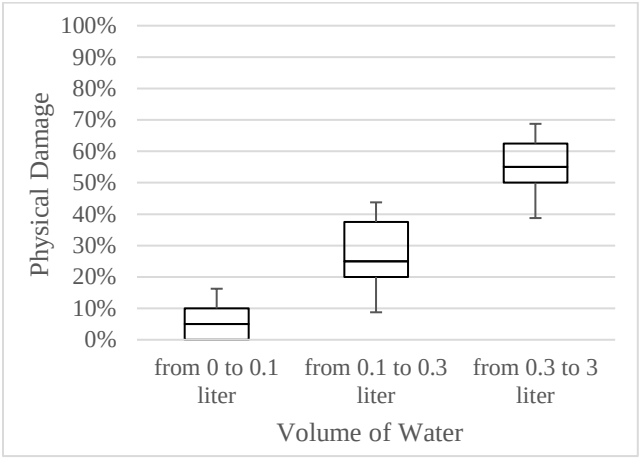

Figure 71. Physical Damage-Volume of water relation for the South Wall

These experimental relations, named as water-damage relations, can be used to estimate the sustained damage by partitions given the volume of water that impacts them. As a result of the water propagation tests (Chapter 3), the FPHLM interior loss module can be modified to calculate the volume of water that reaches different interior components, including the partition. Therefore, in the final step, the water-damage relations can be implemented into FPHLM to predict the sustained physical damage by partitions given the volume of water that reaches them.

The application of these experimental data in probabilistic loss estimation models like FPHLM can significantly improve their loss prediction accuracy. The current loss estimation models predict the interior losses using approximate relations obtained from post-hurricane surveys. Those approximate relations are based on individual opinion rather than experimental test results.

The accurate loss estimation is very important for hurricane rehabilitation decision making, as well as hurricane risk management, especially for hurricane-prone states like Florida. The results of this study can improve the hurricane loss estimation and help the decision makers and stakeholders to improve their policies and ensure the economic sustainability and safety of citizens.

CHAPTER 5

SUMMARY AND CONCLUSIONS

CHAPTER 5. SUMMARY AND CONCLUSIONS

5.1. Summary

This study aimed to experimentally investigate the effect of rain intrusion during hurricane events on the building interior. The research was performed in three main phases, including simulation of Wind-Driven Rain at the WOW EF, interior water propagation tests on large-scale wood building models, and damage evaluation of interior walls of a full-scale model.

During the first phase, the proper nozzle type and arrangement were selected to generate the rain field with matching characteristics to the wind-driven rain field associated with hurricane events. Two drop-size measurement devices (i.e. Parsivel^2 and the PIP) were used to record the rain size distribution of the simulated rain field. It was concluded that for the small droplets (generated with the scale of 1:4) of this study, Parsivel^2 was not accurate enough and the PIP provided more precise measurements. Different nozzle types were tested at stagnant air to compare the rain size distribution generated by different nozzle types. Additionally, one of the nozzle types was tested at different water pressures, and it was shown that the size distribution is not significantly affected by the pressure fluctuations. Finally, the nozzles were installed on the spires in front of the fans, and the generated rain size distribution was compared to the target rain size distribution. It was shown that the simulated rain field could adequately represent the rain characteristics of a hurricane. The tests were repeated, and measurements were performed at different locations of the WOW EF test section. It was shown that the generated rain field was uniform across the test section. Similarly, the rain rate was

measured using a tipping bucket rain gauge at different locations on the test section, and uniformity of the rain rate was also confirmed.

The second phase of the study concentrated on the experimental evaluation of the water propagation pattern in the building interior once it was subjected to simultaneous wind and rain effects. The 1:4 large-scale building model was built out of wood. The interior of the model was divided into six identical room compartments and six attic compartments. Each of these compartments was connected to a separate water bucket to collect the accumulated water. The interior walls and partitions were covered with super-absorbent pads to measure the amount of water that reached their surface. Since the water intrusion into the building is directly affected by the exterior openings, it was decided to test the building model at different exterior conditions, including light, minor and moderate damage states to observe water propagation associated with each of these cases. Also, to consider the effect of various roof types, the model was tested with a gable and a hip roof attached to it. Each model configuration was tested at 0˚, 45˚ and 90˚ wind directions. At the end of each test, the amount of water that reached different interior components (i.e. partitions, flooring, and ceiling) was obtained and reported as the weight of water in grams. The results showed that:

- In general, the internal water propagation followed a similar pattern for room compartments of the gable and hip roof models.
- For the light damage state configuration, only the attic compartment directly below the defect was affected by water intrusion. The small area of the opening and lack of internal wind flow can justify this observation.

- In the light damage state, only the wall defected by the opening and the adjacent flooring component was affected by the water intrusion. In this case, also the internal wind flow was negligible and could not propagate the water inside the building.
- For the minor and moderate damage state model configurations, it was shown that the large exterior envelope openings can result in a powerful internal wind flow, which significantly affects the water propagation path in the building interior.
- By predicting the direction of the internal wind flow through the probable large envelope opening, such as windows, we can estimate the least affected interior locations and minimize the expected damage by placing the expensive water-sensitive instruments, such as appliances, there.

The last phase of the research was dedicated to the experimental evaluation of the moisture-induced damage at the interior walls subjected to water intrusion. For these experimental tests, the full-scale model of a single-story building with a gable roof was subjected to water intrusion at the WOW EF test section. The interior walls of the model were built by installing commercial gypsum board panels on stud walls. Then, the surface of the drywall was painted by one layer of primer and paint, which is the typical practice in residential building construction. Once the model was prepared, the moisture measurement spots were marked on each wall. Additionally, a gutter was installed below each interior wall to collect the surface runoff water on the surface of that wall. Each gutter was connected to a separate bucket, where the collocated surface runoff water accumulated. The model was tested at three configurations, including one open windward

window subjected to the 0˚ and 45˚ wind directions, and two open windows, with one subjected to the 0˚ wind angle of attack. Each model configuration was tested at consecutive periods of water exposure. After each exposure period, the moisture content of the drywall was measured at the marked locations on the interior walls. Additionally, the buckets were weighted to obtain the amount of the surface runoff water on the surface of the walls during the exposure period. The moisture expansion pattern across the wall surface associated with different levels of water exposure was observed, and the results were presented graphically. It was shown that the second open window can significantly increase the internal wind flow and result in a much more extended water propagation inside the building. The sustained damage of the interior walls was estimated based on the increase in moisture content across the wall surface. Finally, for each of the interior walls, the percentage of damage was related to the amount of water that reaches the wall surface.

5.2. Conclusions and future work

To conclude, this research provided experimental data to evaluate the interior damage of the residential buildings caused by rain intrusion during the hurricane events. The results of the second phase of the study can be used to estimate the water distribution among different interior components, including flooring, partitions and ceiling, while the water-damage relations obtained from the last phase of the study can be used to evaluate the sustained damage by the interior components given the volume of water that reaches the component. These results can be implemented in loss estimation models, such as FPHLM, to calculate the monetary damage sustained by the building interior at any given

wind speed and rain intensity. The application of the resulted experimental data can significantly improve the interior loss estimation module of the probabilistic loss estimation models and lead to a more realistic prediction of the hurricane-induced loss of residential buildings.

While this study was a great step forward to experimentally evaluate the rain-induced damages of the building interior, there is still more research to be done. In this study, one model configuration was tested for the wall openings at any damage state and roof type. For future research, the water propagation tests can be performed to investigate the water distribution at other possible configurations of wall openings for any given damage state. Also, in the last phase of the study, the water-damage relations were obtained only for partitions. In the future, an experimental study can be performed to develop similar water-damage relations for the other groups of interior components, including ceiling, flooring, and cabinet.

REFERENCES

ANSI/IICRC S500. (2015). *Standard and Reference Guide for Professional Water Damage Restoration.*

ASTM C472. (2012). *C472-Standard, Test Methods for Physical Testing of Gypsum Panel Products*. West Conshohocken, PA: American Society for Testing and Materials.

ASTM C1396. (2014). *C1396-Standard Specification for Gypsum Board*. West Conshohocken, PA: American Society for Testing and Materials.

ASTM E331. (2009). *ASTM E331-00 Standard test method for water penetration of exterior windows, curtain walls, and doors by uniform static air pressure difference*. West Conshohocken, PA: American Society for Testing and Materials.

ASTM E547. (2009b). *ASTM E547-00 Standard test method for water penetration of exterior windows, curtain walls, and doors by cyclic static air pressure difference*. West Conshohocken, PA: American Society for Testing and Materials.

Baheru, T. (2014). *Development of Test-Based Wind-Driven Rain Intrusion Model for Hurricane-Induced Building Interior and Contents Damage*. Miami, Florida: Florida International University.

Best, A. C. (1950). The size distribution of raindrops. *Quarterly Journal of the Royal Meteorological Society, 76(327),* 16-36.

Bhinderwala, S. (1995). *Insurance loss analysis of single family dwellings damaged in hurricane Andrew*. Clemson, South Carolina: Clemson University.

Blocken, B., & Carmeliet, J. (2002). Spatial and temporal distribution of driving rain on a low-rise building. *Wind and Structures, 5*(5), 441-462.

Choi, E. C. (1999). Wind-driven rain on building faces and the driving-rain index. *Journal of Wind Engineering and Industrial Aerodynamics, 79*(1), 105-122.

Chowdhury, A. G., Zisis, I., Bitsuamlak, G., Pinelli, J. P., Hajra, B., & Moravej, M. (2017). Large-scale experimentation using the 12-fan wall of wind to assess and mitigate hurricane wind and rain impacts on buildings and infrastructure systems. *Journal of Structural Engineering, 143(7).*

Cope, A. D. (2004). *Predicting the vulnerability of typical residential buildings to hurricane damage.* Gainesville, Florida: University of Florida.

Desta, T. Z., Langmans, J., & Roels, S. (2011). Experimental data set for validation of heat, air and moisture transport models of building envelopes. *Building and Environment, 46*(5), 1038-1046.

Dingle, N., & Lee, Y. (1972). Terminal fallspeeds of raindrops. *Journal of Applied Meteorology, 11*(5), 877-879.

FEMA 488. (2005). *Mitigation Assessment Team Report: Hurricane Charley in Florida, observations, recommendations, and technical guidance*.

FEMA. (2005). *Mitigation assessment team report: Hurricane Ivan in Alabama and Florida, observations, recommendations, and technical guidance*.

FEMA P-942. (2013). *Hurricane Sandy in New Jersey and New York Building Performance Observations, Recommendations*.

FPHLM. (2015). *Florida Public Hurricane Projection Loss Model 6.1*. Miami, Florida: Florida Commission on Hurricane Loss Projection Methodology.

Friedrich, K., Higgins, S., Masters, F. J., & Lopez, C. R. . (2013). Articulating and stationary PARSIVEL disdrometer measurements in conditions with strong winds and heavy rainfall. *Journal of Atmospheric and Oceanic Technology, 30*(9), 2063-2080.

Gypsum Association. (2010). *Gypsum board typical mechanical and physical properties*. Hyattsville, MD: Gypsum Association.

Gypsum Association. (2015). *Assessing water damge of gypsum board*. Hyattsville, MD: Gypsum Association

Harriman, L. (2006). Practical Aspects of Locating and Measuring Moisture in Buildings. *Indoor Environment*.

HAZUS. (2009). *Hazus MH 2.1, Multi-hazard Loss Estimation Methodology-Hurricane Model*. Washington, D.C.: Federal Emergency Management Agency, Mitigation Division.

Hens, H., & Fatin, A. M. (1995). *Heat-air-moisture design of masonry cavity walls: Theoretical and experimental results and practice*. Atlanta, GA: American Society of Heating, Refrigerating and Air-Conditioning Engineers, Inc.

ISO. (2009). *Hygrothermal performance of buildings - Calculation and presentation of climatic data. Part 3: calculation of a driving rain index for vertical surfaces from hourly wind and rain data*: Finnish Standards Association SFS Helsinki.

Johansson, P., Ekstrand-Tobin, A., Svensson, T., & Bok, G. (2012). Laboratory study to determine the critical moisture level for mould growth on building material. *International Biodeterioration & Biodegradation, 73*, 23-32.

Johnson, T. (2015). *Interior Damage Prediction in Residential Buildings Due to Hurricane Induced Rain Penetration*. Melbourne, Florida: Florida Institute of Technology.

Johnson, T., Pinelli, J.-P., Baheru, T., Chowdhury, A. G., Weekes, J., & Gurley, K. (2018). Simulation of Rain Penetration and Associated Damage in Buildings within a Hurricane Vulnerability Model. *Natural Hazards Review, 19*(2).

Korsgaard, V., & Rode, C. (1992). *Laboratory and practical experience with a novel water-permeable vapor retarder*. Paper presented at the Thermal Perform ance o f the E xterior Envelopes of Buildings, Conference Proceeding, Clearwater Beach, Florida.

Lacy, R. E. (1977). *Climate and building in Britain*: HM Stationery Office

Lopez, C. R. (2011). *Measurement, analysis, and simulation of wind driven rain.* Gainesville, Florida: University of Florida.

Mendes, N., & Philippi, P. C. (2005). A method for predicting heat and moisture transfer through multilayered walls based on temperature and moisture content gradients. *International Journal of Heat and Mass Transfer, 48*(1), 37-51.

Mileti, D. (1999). *Disasters by Design: A Reassessment of Natural Hazards in the United States*: Joseph Henry Press.

Mualem, Y., & Assouline, S. (1986). Mathematical model for rain drop distribution and rainfall kinetic energy. *Transactions of the ASAE-American Society of Agricultural Engineers (USA)*.

National Science Board. (2007). *Hurricane warning: the critical need for a national hurricane research initiative*. National Science Foundation.

Nielsen, K. F., Holm, G., Uttrup, P., L., & Nielsen, P. A. (2004). Mould growth on building materials under low water activities. Influence of humidity and temperature on fungal growth and secondary metabolism. *International Biodeterioration & Biodegradation, 54*(4), 325-336.

Pasanen, A. L., Juutinen, T., Jantunen, M. J., & Kalliokoski, P. (1992). Occurrence and moisture requirements of microbial growth in building materials. *International Biodeterioration & Biodegradation, 30*(4), 273-283.

Pita, G., P., P. j., Cocke, S., Gurley, K., Mitrani-Reiser, J., Weekes, J., & Hamid, S. (2012). Assessment of hurricane-induced internal damage to low-rise buildings in the Florida Public Hurricane Loss Model. *Journal of Wind Engineering and Industrial Aerodynamics, 104*, 76-87.

Pita, G. L. (2012). *Pita, Gonzalo Luis. Hurricane vulnerability of commercial-residential buildings*. Melbourne, Florida: Florida Institute of Technology.

Straube, J., & Burnett, E. (2000). *Simplified prediction of driving rain on buildings.* Paper presented at the Proceedings of the international building physics conference, Eindhoven, Netherlands.

TeeJet Technologies. (2015). Catalog 51A.

Tokay, A., Bashor, P. G., Habib, E., & Kasparis, T. (2008). Raindrop size distribution measurements in tropical cyclones. *Monthly Weather Review, 136(5)*, 1669-1685.

Tokay, A., Petersen, W. A., Gatlin, P., & Wingo, M. (2013). Comparison of raindrop size distribution measurements by collocated disdrometers. *Journal of Atmospheric and Oceanic Technology, 30*(8), 1672-1690.

Tokay, A., Wolff, D. B., & Petersen, W. A. (2014). Evaluation of the new version of the laser-optical disdrometer, OTT Parsivel2. *Journal of Atmospheric and Oceanic Technology, 31*(6), 1276-1288.

Tsongas, G. A., Govan, D. P., & McGillis, J. A. (1998). Field observations and laboratory tests of water migration in walls with shiplap hardboard siding. *Thermal envelopes VII/Moisture-practices*, 469-483.

Van de Lindt, J. W., Graettinger, A., Gupta, R., Skaggs, T., Pryor, S., & Fridley, K. J. (2007). Performance of wood-frame structures during Hurricane Katrina. *Journal of Performance of Constructed Facilities*(American Society of Civil Engineers).

Waldvogel, A. (1974). The N 0 jump of raindrop spectra. *Journal of the Atmospheric Sciences, 31*(4), 1067--1078.

VITA

FARZANEH RAJI

Born, Tehran, Iran

2003 - 2008	B.Sc., Civil Engineering, Iran University of Science and Technology, Tehran, Iran.
2008 - 2010	M.Sc., Structural Engineering, Sharif University of Technology, Tehran, Iran
2013 - 2018	Ph.D., Structural/Wind Engineering, Florida International University, Miami, FL

PUBLICATIONS AND PRESENTATIONS

Raji, F., Zisis, I., (2018) “Rain propagation into the building interior caused by internal wind flow. 3rd Thermal and Fluids Engineering Conference (TFEC), Fort Lauderdale, FL, USA

Raji, F., Zisis, I., Pinelli, J. P., Chowdhury, A. G., (2017). “Interior damage of residential buildings due to wind-driven rain intrusion”. 13th Americas Conference on Wind Engineering, Gainesville, Florida, USA.

Naeiji, A., Raji, F., and Zisis, I. (2017). Wind loads on residential scale rooftop photovoltaic panels. Journal of Wind Engineering and Industrial Aerodynamics, 168, 228-246.

Zisis, I., Raji, F., & Jose D. Candelario (2016). “Large-scale wind tunnel tests of canopies attached to low-rise buildings.” Journal of Architectural Engineering.

Naeiji, A., Raji, F., & Zisis, I. (2015). “Large-scale wind testing of photovoltaic panels mounted on residential roofs”. In Structures Congress 2015 (pp. 1868-1878), Portland, Oregon.

Candelario, J., Raji, F., Naeiji, A., Zisis, I., Chowdhury, A. (2015). “Large-scale wind testing on canopies attached to residential buildings”. In 14th International Conference in Wind Engineering Proceeding, Porto Alegre, Brazil.

Naeiji, A., Raji, F., Zisis, I., Chowdhury, A., Irwin, P. (2015). “Wind-induced pressures and forces on solar panels mounted on flat, gable or hip roof residential buildings”. In 14th International Conference in Wind Engineering Proceeding, Porto Alegre, Brazil.

Zisis, I., Naeiji, A. and Raji, F. (2014). “Codification of wind-induced loads on rooftop solar panels”. Final report submitted to The State of Florida Division of Emergency Management.

A. Abdelnaby, F Raji, A. Yohannes, A. Naimi, S Mishra, M Golias (2014). “Impact of the 1811-1812 earthquakes on existing transportation networks in Memphis area”. 10th US National Conf. on Earthquake Engineering Frontiers of Earthquake Engineering".

Rofooei F., Raji F., (2011). “Probabilistic loss estimation of concrete MRF models subjected to near field earthquakes”. Proceedings of the 8th International Conference on Structural Dynamics, EURODYN 2011.